Computer assisted analysis of contrast enhanced ultrasound images for quantification in vascular diseases

Wing Keung Cheung

March 2016

PhD thesis
Department of Bioengineering
Imperial College London

Submitted for the degree of Doctor of Philosophy of Imperial College London

Declaration of Originality

The work presented in this thesis is my own work unless otherwise attributed.

Wing Keung Cheung

March 2016

Copyright Declaration

Abstract

Contrast enhanced ultrasound (CEUS) with microbubble contrast agents has shown great potential in imaging microvasculature, quantifying perfusion and hence detecting vascular diseases. However, most existing perfusion quantification methods based on image intensity, and are susceptible to confounding factors such as attenuation artefacts. Improving reproducibility is also a key challenge to clinical translation. Therefore, this thesis aims at developing attenuation correction and quantification techniques in CEUS with applications for detection and quantification of microvascular flow / perfusion.

Firstly, a technique for automatic correction of attenuation effects in vascular imaging was developed and validated on a tissue mimicking phantom. The application of this technique to studying contrast enhancement of carotid adventitial vasa vasorum as a biomarker of radiation-induced atherosclerosis was demonstrated. The results showed great potential in reducing attenuation artefact and improve quantification in CEUS of carotid arteries. Furthermore, contrast intensity was shown to significantly increase in irradiated carotid arteries and could be a useful imaging biomarker for radiation-induced atherosclerosis.

Secondly, a robust and automated tool for quantification of microbubble identification in CEUS image sequences using a temporal and spatial analysis was developed and validated on a flow phantom. The application of this technique to evaluate human musculoskeletal microcirculation with contrast enhanced ultrasound was demonstrated. The results showed an

excellent accuracy and repeatability in quantifying active vascular density. It has great potential for clinical translation in the assessment of lower limb perfusion.

Finally, a new bubble activity identification and quantification technique based on differential intensity projection in CEUS was developed and demonstrated with an in-vivo study, and applied to the quantification of intraplaque neovascularisation in an irradiated carotid artery of patients who were previously treated for head and neck cancer. The results showed a significantly more specific identification of bubble signals and had good agreement between the differential intensity-based technique and clinical visual assessment. This technique has potential to assist clinicians to diagnose and monitor intraplque neovascularisation.

Acknowledgements

I would like to express my gratitude to my thesis supervisor, Dr Meng-Xing Tang, for his patient guidance in supervising me through the research. His help, support and understanding encourage me to overcome challenges and take ownership of my research projects, which is very important for me to become an independent researcher. He also provides me with opportunities in presenting the research work in international conferences, which allows me to gain new insight for my research.

I would also like to thank Dr Robert Eckersley, Prof David Cosgrove, Prof Alun Davies and Prof Roxy Senior for their valuable advice and suggestions in conducting research and writing papers.

In addition, I would like to thank my clinical collaborators, Dr Dorothy Gujral, Dr Benoy Shah, Dr Navtej Chahal, Dr Katherine Williams and Dr Brahman Dharmarajah, who helped me throughout my research. Without their inputs, the research projects would never be possible.

Special thanks to all members of Ultrasound Laboratory for Imaging and Sensing for their support and helpful input during the weekly group meetings.

Finally, I must thank my wife, Grace Fan, who supports me unconditionally. I could not have done my doctoral study without you.

Table of Contents

List of Publications

[1] **Cheung WK**, Gujral DM, Shah B, Chahal N, Bhattacharyya S, Cosgrove D, Eckersley RJ, Harrington KJ, Senior R, Nutting CM, Tang M-X. *Attenuation Correction and Normalisation for Quantification of Contrast Enhancement in Ultrasound Images of Carotid Arteries*, Ultrasound in Medicine and Biology, Vol. 41, No. 7, 01.07.2015, p. 1876-1883.

[2] Stanziola A, **Cheung WK**, Eckersley RJ, Tang M-X. *Motion Correction in Contrast-Enhanced Ultrasound Scans of Carotid Atherosclerotic Plaques*, Proceedings of The IEEE International Symposium on Biomedical Imaging: From Nano to Macro (ISBI), New York, USA, 16-19 April 2015.

[3] **Cheung WK**, Williams KJ, Christensen-Jeffries K, Dharmarajah B, Eckersley RJ, Davies AH, Tang M-X. *Reproducible and automated quantification of active vascular density in human lower limbs using contrast enhanced ultrasound and an automated temporal and spatial analysis algorithm.* European Journal of Ultrasound (under review).

[4] **Cheung WK**, Shah B, Stanziola A, Gujral DM, Chahal N, Cosgrove D, Senior R, Tang M-X. *Differential intensity projection (DIP) for detection and quantification of plaque neovascularisation in CEUS images of carotid arteries.* Ultrasound in Medicine and Biology (under review).

[5] Gujral DM, **Cheung WK**, Shah B, Chahal N, Bhattacharyya S, Hooper J, Senior R, Tang M-X, Harrington KJ, Nutting CM. *Contrast enhancement of carotid adventitial vasa vasorum as a biomarker of radiation-induced atherosclerosis.* Radiotherapy and Oncology (under review).

List of Figures

List of Tables

List of Abbreviations

ABI	ankle-brachial index
ASL	arterial spin labeling
CAS	carotid artery stenting
CBF	cerebral blood flow
CBV	cerebral blood volume
CCA	common carotid artery
CEA	carotid endarterectomy
CEUS	contrast enhanced ultrasound
CIMT	carotid intima-media thickness
COV	coefficient of variation
CVD	cardiovascular disease
DCE	dynamic contrast-enhanced
DIP	differential intensity projection
DM	diabetes mellitus
DR	destruction and replenishment
ECG	electrocardiography
fMRI	functional magnetic resonance imaging
FWHM	full width half maximum
GTT	glucose tolerance test
HbA1c	haemoglobin A1c
HFR	harmonic-to-fundamental ratio
HLFR	high-to-low frequency ratio
HNC	head and neck cancer
ICC	intra-class correlation
IPH	intraplaque haemorrhage
IPN	intraplaque neovascularisation
LDL	low density lipoproteins
LHS	left hand side
MI	mechanical index

MIP	maximum intensity projection
MIRT	medical image registration toolbox
MR	magnetic resonance
MRI	magnetic resonance imaging
MTD	microbubble track density
MTT	mean transit time
MVA	microvascular area
MVD	microvascular density
NIF	normalised intensity fluctuation
PAD	peripheral arterial disease
PTA	percutaneous transluminal angioplasty
RHS	right hand side
ROI	region of interest
RT	radiotherapy
SD	standard deviation
TGC	time gain compensation
TIC	time intensity analysis
TMM	tissue-mimicking phantom
US	ultrasound
VV	vasa vasorum
WHO	World Health Organization

Chapter 1

Introduction

1.1 Background and motivation

According to the World Health Organization (WHO), cardiovascular disease is the leading cause of death globally (1) and there is an increase in the number of people who die from such disease. In particular, atherosclerosis (2) and peripheral arterial disease (3) are very common types of vascular diseases and can be fatal if there is a lack of early intervention. These diseases are caused by the build-up of fatty deposits in the blood vessels, result in the changes of microvasculature and blood flow. There is an urgent and unmet clinical need for early diagnosis and monitoring of these diseases. Current imaging modalities can be used to image large- and medium-sized blood vessels in the human body under different conditions, but lack the necessary sensitivity, resolution, contrast or penetration depth to see small vessels or capillary networks. Recently, the echo-enhancing microbubbles have made it possible to image and quantify microcirculation using ultrasound (4). These bubbles are small enough to move through the microvasculature, and remain completely within the vascular space throughout the circulation. Hence, they are ideal for studying vessel architecture and image microcirculation. An accurate quantification of the microbubble signals can provide valuable clinical information about tissue microcirculation for both diagnosis and assisting therapy. However there are still a number of technical problems that need to be addressed before a reliable quantification technique based on CEUS can be developed and used in clinical practice in e.g. atherosclerosis and peripheral arterial disease.

The first issue is the attenuation effect. During a US diagnosis, ultrasound echo from a target is affected by attenuation between US wave and the target segmented tissues. The reduced signal amplitude can not only significantly affect the quality of the image produced but also the quantification results, as most quantification methods are based on image intensity. Many studies have been done to address the problem of inaccurate compensation of attenuation in standard B-mode US and contrast enhanced ultrasound (CEUS) in general (5-8). However, an accurate attenuation compensation technique for automatically quantifying tissue perfusion with microbubbles has yet been well exploited.

The second issue is the lack of reliable perfusion quantification algorithms. Traditional techniques such as manual visual assessment (9), time intensity curve analysis (10-12) and destruction and replenishment analysis (13) are being used to quantify microbubble signal in contrast-enhanced ultrasound imaging nowadays. However, they all have various shortcomings. Most existing approaches for perfusion quantification using CEUS are calculated based on image intensity, and are susceptible to confounding factors such as attenuation and nonlinear propagation imaging artefacts (14-17). Improving reproducibility is also a key challenge to clinical translation. Poor reproducibility means there is a high degree of variability in quantitative results which leads to diagnostic uncertainty.

Therefore, for atherosclerosis and peripheral arterial disease diagnosis, it is particularly important to develop new methods for improved quantification.

The objectives of the thesis are:

1. To develop an automatic attenuation correction technique in contrast-enhanced ultrasound images and apply the technique to in vivo contrast enhanced ultrasound images of human carotid arteries.
2. To develop an automatic and robust microbubble identification technique in contrast-enhanced ultrasound images and apply the technique to quantification of in vivo musculoskeletal microcirculation in the lower limb.
3. To develop a differential intensity-based image visualisation and quantification technique in contrast-enhanced ultrasound images and apply the technique to quantify intraplaque neovascularisation.

1.2 Thesis structure

Chapter 2 is a literature review. Firstly, the clinical background on vascular diseases particularly atherosclerosis and peripheral artery disease (including diabetes mellitus-related) is introduced. Secondly, a technical review on medical imaging of vascular disease is presented. It includes magnetic resonance imaging, ultrasound imaging and contrast enhanced ultrasound imaging. Finally, a review of current state-of-the-art quantification methods in CEUS such as motion correction, intensity-based quantification, attenuation and its correction and temporal-based quantification is discussed.

Chapter 3 describes the development of an automated attenuation correction and normalisation algorithm to improve the quantification of contrast enhancement in ultrasound images of carotid arteries. It is based on the assumption that microbubble contrast agents are well mixed in the lumen and hence, the image intensity across the vessel lumen should be homogeneous (except intensity variations due to speckles) if attenuation is properly corrected

for. The algorithm is first validated on phantoms consisting of contrast agent-filled vessels embedded in tissue mimicking materials of known attenuation. It is subsequently applied to in vivo contrast enhanced ultrasound images of human carotid arteries. Both in vitro and in vivo results showed significant reduction in the shadowing artefact and improved homogeneity within the carotid lumen after the correction. This study has been included in (18).

Chapter 4 introduces a robust and automated quantification tool for microbubble identification in CEUS image sequences using a pixel level temporal and spatial analysis based algorithm. This technique is demonstrated on a phantom and then, as an initial clinical demonstration, applied to the quantification of in vivo musculoskeletal microcirculation in lower limb perfusion of healthy human subjects. A microbubble track density (MTD) measure, the ratio of the segmented microbubble area over the whole tissue area, is calculated as a surrogate for active capillary density. In vitro results showed a good correlation between the calculated MTD measure and the known bubble concentration. For in vivo results, a significant increase in the MTD measure was found in lower limbs of healthy volunteers after exercise, with excellent repeatability over a series of days. The proposed new approach demonstrates great potential as an accurate and highly reproducible clinical tool for quantification of active vascular density.

Chapter 5 performs a study to develop a microbubble detection and quantification technique for CEUS by using differential intensity projection (DIP). This technique was demonstrated with an in-vivo study, and applied to the quantification of intraplaque neovascularisation in an irradiated carotid artery of patients who were previously treated for head and neck cancer.

The results using DIP were compared with those obtained by maximum intensity projection (MIP) and visual assessment. The results showed that DIP can significantly reduce nonlinear propagation tissue artefacts and is much more specific in detecting bubble signals than MIP, being able to reveal IPN signals which are buried in tissue artefacts in the corresponding MIP image. A good correlation was found between MVA / MVD obtained using DIP and the corresponding expert visual grades. In conclusion, the proposed method shows great potential in quantification of IPN in the contrast enhanced ultrasound of carotid arteries.

Chapter 6 summarises the content of the thesis and includes a discussion about the techniques and future work.

References

1. Mendis S, Puska P, Norrving B, et al. Global atlas on cardiovascular disease prevention and control. Geneva: World Health Organization in collaboration with the World Heart Federation and the World Stroke Organization; 2011.
2. Faxon DP, Creager MA, Smith SC, Jr., et al. Atherosclerotic Vascular Disease Conference: Executive summary: Atherosclerotic Vascular Disease Conference proceeding for healthcare professionals from a special writing group of the American Heart Association. Circulation. 2004;109(21):2595-604.
3. Amarteifio E, Weber MA, Wormsbecher S, et al. Dynamic contrast-enhanced ultrasound for assessment of skeletal muscle microcirculation in peripheral arterial disease. Invest Radiol. 2011;46(8):504-8.

4. Feinstein SB**.** The powerful microbubble: from bench to bedside, from intravascular indicator to therapeutic delivery system, and beyond. American Journal of Physiology-Heart and Circulatory Physiology. 2004;287(2):H450-H7.

5. Wells PNT**.** Ultrasound imaging. Physics in Medicine and Biology. 2006;51(13):R83-R98.

6. Mule S, De Cesare A, Lucidarme O, et al. Regularized estimation of contrast agent attenuation to improve the imaging of microbubbles in small animal studies. Ultrasound in Medicine and Biology. 2008;34(6):938-48.

7. Mari JM, Hibbs K, Stride E, et al. An Approximate Nonlinear Model for Time Gain Compensation of Amplitude Modulated Images of Ultrasound Contrast Agent Perfusion. Ieee Transactions on Ultrasonics Ferroelectrics and Frequency Control. 2010;57(4):818-29.

8. Tang MX, Mari JM, Wells PNT, Eckersley RJ**.** Attenuation Correction in Ultrasound Contrast Agent Imaging: Elementary Theory and Preliminary Experimental Evaluation. Ultrasound in Medicine and Biology. 2008;34(12):1998-2008.

9. Feinstein SB**.** Contrast ultrasound imaging of the carotid artery vasa vasorum and atherosclerotic plaque neovascularization. J Am Coll Cardiol. 2006;48(2):236-43.

10. Piscaglia F, Nolsoe C, Dietrich CF, et al. The EFSUMB Guidelines and Recommendations on the Clinical Practice of Contrast Enhanced Ultrasound (CEUS): update 2011 on non-hepatic applications. Ultraschall Med. 2012;33(1):33-59.

11. Dietrich CF, Averkiou MA, Correas JM, et al. An EFSUMB Introduction into Dynamic Contrast-Enhanced Ultrasound (DCE-US) for Quantification of Tumour Perfusion. Ultraschall in Der Medizin. 2012;33(4):344-51.

12. Claudon M, Dietrich CF, Choi BI, et al. Guidelines and good clinical practice recommendations for contrast enhanced ultrasound (CEUS) in the liver--update 2012:

a WFUMB-EFSUMB initiative in cooperation with representatives of AFSUMB, AIUM, ASUM, FLAUS and ICUS. Ultraschall Med. 2013;34(1):11-29.

13. Wei K, Jayaweera AR, Firoozan S, et al. Quantification of myocardial blood flow with ultrasound-induced destruction of microbubbles administered as a constant venous infusion. Circulation. 1998;97(5):473-83.

14. Tang MX, Mulvana H, Gauthier T, et al. Quantitative contrast-enhanced ultrasound imaging: a review of sources of variability. Interface Focus. 2011;1(4):520-39.

15. Stride E, Tang MX, Eckersley RJ**.** Physical phenomena affecting quantitative imaging of ultrasound contrast agents. Applied Acoustics. 2009;70(10):1352-62.

16. Lindner JR, Womack L, Barrett EJ, et al. Limb Stress-Rest Perfusion Imaging With Contrast Ultrasound for the Assessment of Peripheral Arterial Disease Severity. Jacc-Cardiovascular Imaging. 2008;1(3):343-50.

17. Akkus Z, Hoogi A, Renaud G, et al. New Quantification Methods for Carotid Intra-Plaque Neovascularization Using Contrast-Enhanced Ultrasound. Ultrasound in Medicine and Biology. 2014;40(1):25-36.

18. Cheung WK, Gujral DM, Shah BN, et al. Attenuation Correction and Normalisation for Quantification of Contrast Enhancement in Ultrasound Images of Carotid Arteries. Ultrasound in Medicine and Biology. 2015;41(7):1876-83.

Chapter 2

Literature Review

Atherosclerosis, Peripheral Artery Disease (PAD) and Diabetes Mellitus (DM) are common vascular diseases found in humans. As these diseases might not be cured permanently, regular monitoring is essential for the patients with these diseases. Current imaging modalities including Magnetic Resonance Imaging (MRI) and ultrasound (US) have limitations in imaging vasculature in the human body. Recently, Contrast Enhanced Ultrasound (CEUS) has shown potential to become a front-line diagnostic tool to produce high resolution and real-time images of the microvascular perfusion. Nevertheless, CEUS still has technical challenges regarding quantification of micro-circulation. In this chapter the medical background of three stated vascular diseases, the current imaging modalities available to perform diagnosis and the limitations of current quantification technique in CEUS are reviewed and discussed.

2.1 Medical Background of Atherosclerosis, PAD and DM

The medical background including the cause, diagnosis and medical treatment of the three diseases are introduced in this section.

2.1.1 Atherosclerosis

Atherosclerosis is a disease when the arterial wall is narrowed and hardened. It is a result of atherosclerotic plaque formation. Libby et al (1) reported that the infiltration of low density

lipoproteins (LDL) into intima of the vessel wall causes wall thickening. This stimulates monocytes to pass into the vessel wall and differentiate to macrophages. The macrophages then consume the modified LDL and produce macrophage foam cells. As a result, a complex inflammatory response takes place in the affected vessel wall. When this response is progressing, more complex atherosclerotic plaques are formed. Figure 2-1 shows a normal artery and an atherosclerotic artery.

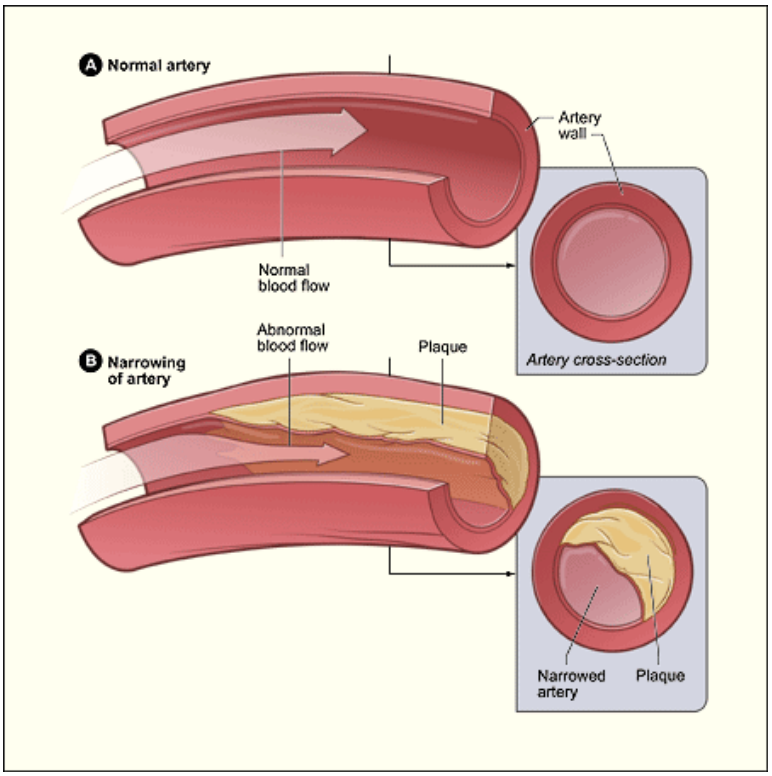

Figure 2-1: (A) a normal artery (B) an atherosclerotic artery[1]

As the plaque is growing, it fills up the whole lumen of the artery. This could lead to blocking of blood flow inside the artery. Consequently, it causes blood clots which could block downstream vessels. Depending on the composition of plaque, plaque may rupture and this could also cause blockage. Stroke may occur because of this blockage.

[1] Joseph Nordqvist . (2013). What Is Atherosclerosis? What Causes Atherosclerosis?. Available: http://www.medicalnewstoday.com/articles/247837.php. Last accessed 27th Sept 2013.

2.1.1.1 Plaque vulnerability

According to plaque composition, plaque can be classified into two types: (A) stable and low risk plaque (B) vulnerable, unstable and high risk plaque. Stable and low risk plaque is composed of a thick fibrous cap over a small fatty core. It is strengthened and stabilised by a collagen protein, which is part of connective tissue and makes the plaque unlikely to rupture (2). Vulnerable, unstable and high risk plaque has a thin fibrous cap over a large fatty core. It progresses when large amounts of LDL and cholesterol accumulate in the plaque. The fatty core expands and the thin fibrous cap begins to erode. At the same time, inflammatory cells within the plaque release enzymes that break down collagen in the cap. A weak fibrous cap is the result, which is highly susceptible to rupture (2). Figure 2-2 shows the composition of stable and vulnerable plaque. It is known that plaque rupture is associated with plaque vulnerability. Plaque vulnerability is responsible for inducing stroke which is the loss of brain function due to the decrease or blockage of blood flow to an area of the brain (3), and brain cells start to die in the absence of oxygen (4). Therefore, plaque vulnerability is the most reliable factor when carrying out risk assessment of stroke in patients.

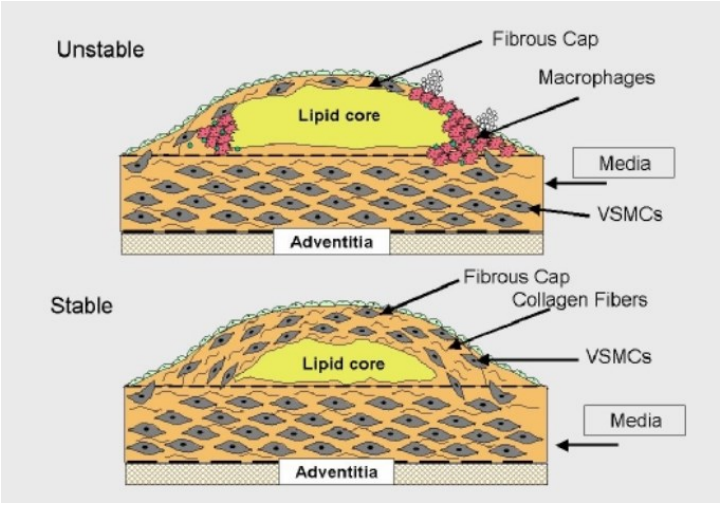

Figure 2-2: (A) vulnerable, unstable and high risk plaque (B) stable and low risk plaque[2]

[2] Weissberg. 2001

2.1.1.2 Biomarkers (CIMT and stenosis)

In order to identify individuals who have an unstable or vulnerable plaque, biomarkers are developed as indicators to show the risk level of atherosclerosis. Currently, carotid intima-media thickness (CIMT) and carotid artery stenosis are the most common biomarkers in carotid artery diagnosis. CIMT is defined as the distance between the lumen-intima interface and the media-adventitia interface (5). The arterial wall is accessed in the longitudinal view. Clinicians perform semi-automated CIMT measurement along a minimum of 10mm length of a selected segment using an edge detection algorithm. Several studies have shown that CIMT is associated with cardiovascular disease (CVD) risk factors and therefore confirm the role of CIMT for predicting cardiovascular events (6). Carotid artery stenosis is the degree of narrowing of the carotid vessel. A stenosis greater than 70% (7) will lead to a surgical intervention. However, both of these biomarkers have limitations. For example, they do not provide information about the composition of plaque. Vulnerable plaques are not necessarily those which intrude the most into the lumen (8). Furthermore, the reliability, efficiency and precision of these measurements are influenced by image artefacts (i.e. attenuation and non-linear propagation artefacts) of ultrasound images. Image artefacts of ultrasound images will potentially introduce variability of these biomarkers. Therefore, a more reliable biomarker should be developed to identify plaque vulnerability at an early stage.

2.1.1.3 Surrogate markers (Neovascularisation of plaque and vasa vasorum)

Recently, neovascularisation of plaque and vasa vasorum have been recognised as two new surrogate markers to reflect plaque vulnerability (9, 10). Vessel wall hypoxia and inflammation are the main causes of neovascularisation (11). Huang et al (12) showed that neovascularisation is a reliable marker of vulnerable plaque. Plaque neovascularisation is the formation of neovessels within the plaque which reflects plaque instability (13). Furthermore,

it was also considered as a predictor of plaque rupture, which is closely linked to atherosclerosis-related stroke. Adventitial vasa vasorum is a network of neovessels with an outside-in orientation, originating from the adventitia and extending to the intima layer of the carotid wall (14). These small vessels provide blood supply for adventitia and outer parts of large vessels. The existence of these small blood vessels is the key feature of early atherosclerosis because they usually precede the actual atherosclerotic plaque development (15, 16). Adventitial vasa vasorum neovascularisation establishes a physiological mechanism to supply nutrients to tissues within the wall (17). There is a clear indication that hyperplasia of adventitial vasa vasorum occurs at the early stage of atherosclerosis, whereas new neovessels extend to the intima-media forming an ectopic neovascularisation in the later stage (18).

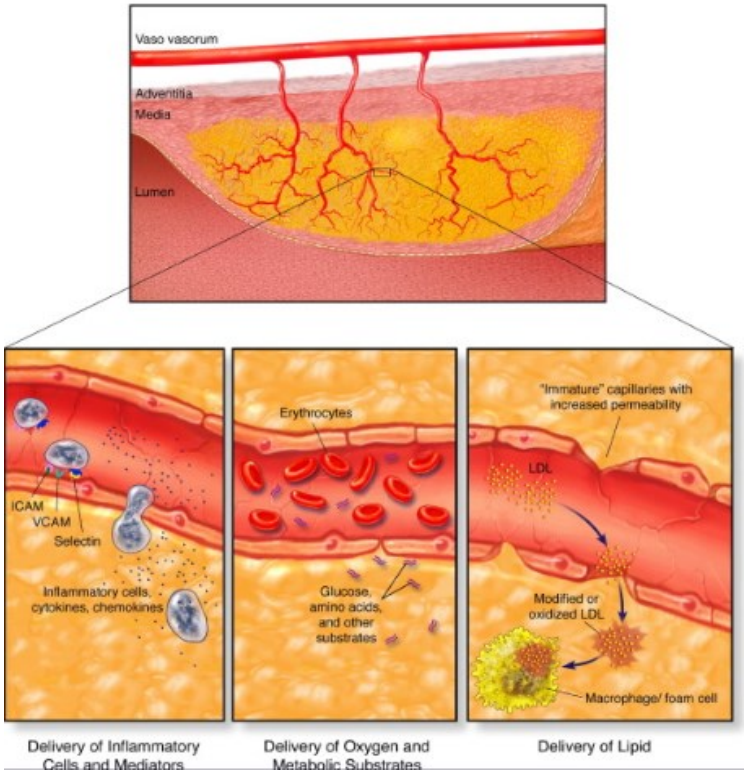

Figure 2-3: Neovascularisation of plaque and vasa vasorum[3]

[3] Doyle B., Caplice N. Plaque neovascularization and antiangiogenic therapy for atherosclerosis. J. Am. Coll. Cardiol. 2007; 49(21): 2073-2080.

These two markers (neovascularisation of plaque and adventitia vasa vasorum, Figure 2-3) play a critical role in indication of early plaque progression and are directly related to the biological properties of plaque. Recent studies also confirmed that there is a pronounced association between plaque neovascularistion, plaque vulnerability and cardiovascular events (13, 15, 19, 20). Furthermore, it is noted that the immature neovascularisation developed in atherosclerosis is very similar to the angiogenesis growing in cancerous tumours (21, 22).

2.1.1.4 Medical treatment - Carotid Endarterectomy and Carotid Artery Stenting

The medical procedures for treatment of carotid artery disease are Carotid Endarterectomy (CEA) and Carotid Artery Stenting (CAS). CEA is a surgical procedure performed by a surgeon who makes an incision in the neck and removes plaque from a carotid artery during CEA. This helps restore normal blood flow through the artery. CAS is a procedure in which the vascular surgeon inserts a slender and metal-mesh tube which is known as a stent. The stent is expanded inside the carotid artery to increase blood flow in areas blocked by plaque. CEA and CAS are the most effective treatments to treat a blocked carotid artery and reduce the risk of stroke (23). However, these surgical interventions are invasive and risky (24). Therefore, it is important to identify patients who are at high risk of stroke in advance to avoid unnecessary, potentially dangerous and expensive surgeries.

2.1.2 Peripheral Artery Disease

Peripheral Artery Disease (PAD) is a disease in which plaque is formed in the arteries. These arteries carry blood to head, organs and limbs. When plaque builds up in the artery, known as

atherosclerosis, the artery narrows down and hence the blood flow decreases. PAD increases the risk of coronary heart disease, heart attack and stroke. Also, it is common to see PAD in legs. Figure 2-4 illustrates how PAD affects the artery in the legs.

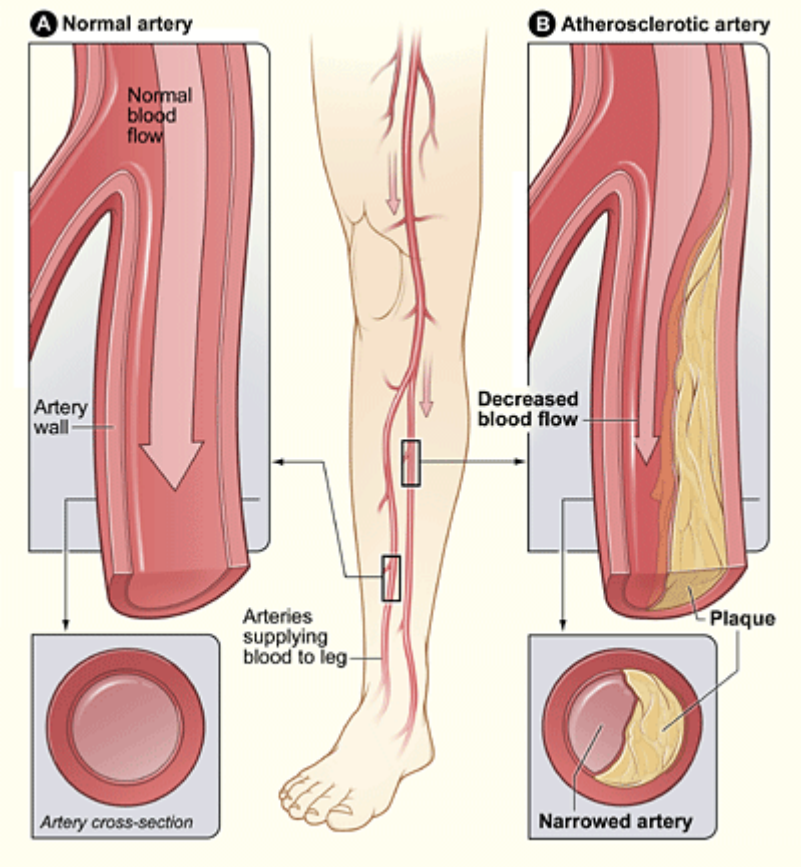

Figure 2-4: The illustration shows how PAD can affect arteries in the legs. (A) A normal artery with normal blood flow. The inset image shows a cross-section of the normal artery. (B) An artery with plaque build-up which is partially blocking blood flow. The inset image shows a cross-section of a narrowed artery[4].

2.1.2.1 Ankle-Brachial Index (ABI)

ABI compares the blood pressure in the ankle to that in the arm. ABI is the ratio of the arterial blood pressure at the ankle divided by the arm blood pressure. An ABI, which is less

[4] https://www.nhlbi.nih.gov/health/health-topics/topics/pad

than 0.9, is good evidence for the diagnosis of PAD. The setup of the test is displayed in Figure 2-5. This test can be applied to limb and show how well the blood flow in one's limb is. Though this Index is useful to show whether PAD is affecting the limb, it cannot identify which vessel is narrowed or blocked.

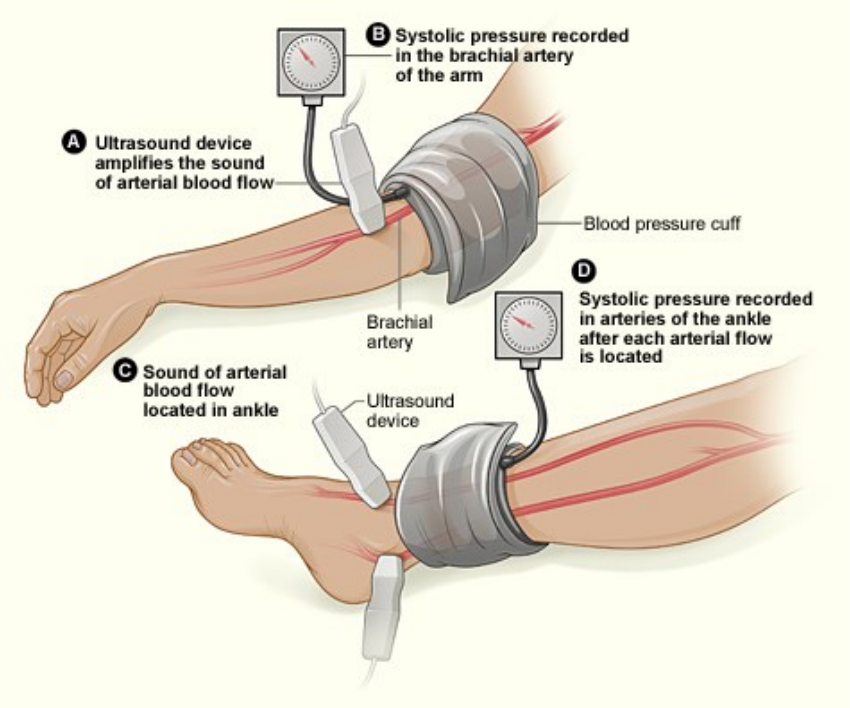

Figure 2-5: The illustration shows the ankle-brachial index test. The test compares blood pressure in the ankle to blood pressure in the arm. As the blood pressure cuff deflates, the blood pressure in the arteries is recorded.[5]

2.1.2.2 Treadmill Test

A treadmill test can show how severe the PAD is. In this test, the patient walks on a treadmill. This shows whether the patient has any PAD symptoms during normal walking. Different levels of exercise would indicate how severe the PAD is. The patient may have an ABI test done before and after the treadmill test. It compares the blood flow in the arms and legs

[5] https://www.nhlbi.nih.gov/health/health-topics/topics/pad/diagnosis

before and after exercise. By combining the treadmill test and ABI test, the clinician can have a better assessment on the severity of PAD.

2.1.2.3 Perfusion quantification of PAD

Although PAD can be diagnosed by the ABI test and treadmill test, they cannot assess muscular perfusion at a microcirculatory level, which would be the critical information for end organ damage (25). In addition, it is known that total blood flow and capillary dilatation responses to muscle contraction are reduced in patients with PAD, therefore, perfusion quantification could help to quantify and visualise the disease. This quantitative information could be useful for monitoring PAD over time as well as evaluating treatment performance. Existing imaging techniques such as Dynamic Contrast-Enhanced (DCE) Magnetic Resonance Imaging and functional Magnetic Resonance Imaging (fMRI) could be used to quantify the microcirculation (26). However, these techniques are very sensitive to motion artefacts, even a small movement could lead to a poor image, which affects the quantitative results. In addition, these techniques could not provide reproducible results, hence they are currently not suitable to be used in clinical practice for PAD diagnosis. Alternatively, a recent advance in Contrast Enhanced Ultrasound (CEUS) which allows imaging for vasculature, despite the technical problems of perfusion quantification which need to be addressed, CEUS provides a unique opportunity to be a front-line imaging tool to assess PAD. Therefore, it is important to develop an accurate and reliable quantification technique in CEUS.

2.1.2.4 Medical treatment - blood thinning medications

The effective treatment of peripheral artery disease is blood thinning medications. Also, diet control and regular exercise could improve patient's symptoms. Clinician may also prescribe

medications to control some of the risk factors for PAD, including high blood pressure and high cholesterol.

However, the above treatments may only improve the patient's condition temporarily. If the symptoms of PAD get worse rapidly, a surgical procedure may be necessary. It is a procedure called a Percutaneous Transluminal Angioplasty (PTA) or a balloon angioplasty procedure. The basic principle of a balloon angioplasty procedure is that a small balloon is inflated inside an artery to open up the artery, and hence improve blood flow in the artery. The procedure is safe, much less invasive than traditional surgery, and now standard treatment for most forms of PAD. Figure 2-6 shows the balloon angioplasty procedure. However, all the treatments mentioned above may not be able to cure PAD. Therefore, regular monitoring is vital.

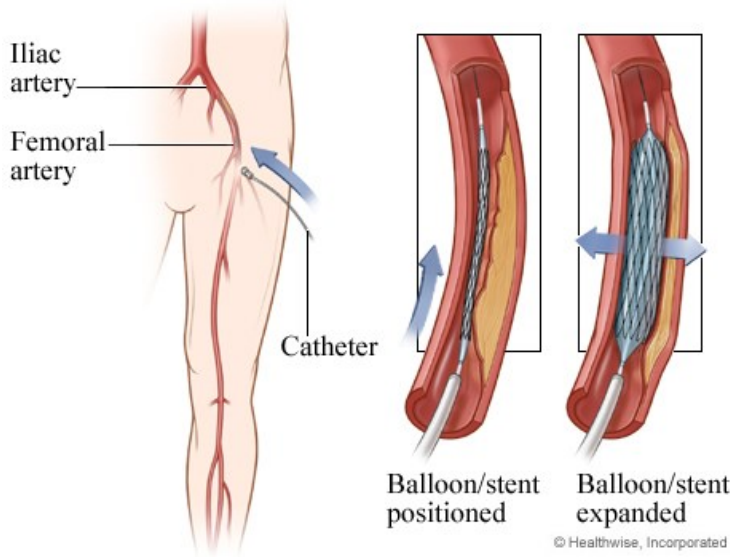

Figure 2-6: The illustration shows the balloon angioplasty procedure.[6]

[6] https://myhealth.alberta.ca/Health/Pages/conditions.aspx?hwid=aa118416

2.1.3 Diabetes Mellitus

Diabetes mellitus (DM) is a disease in which there are high blood glucose levels over a prolonged period. It is also commonly known as diabetes. Patients with DM have symptoms of high blood glucose including frequent urination, increased thirst and increased hunger. Diabetes can cause many long-term complications, i.e. cardiovascular disease, stroke, chronic kidney failure, foot ulcers and damage to the eyes.

Diabetic patients are at high risk for peripheral arterial disease (PAD) characterised by symptoms of intermittent claudication or critical limb ischaemia (27). PAD in diabetic patients is caused by the angiopathy affecting the medium-sized arteries predominantly and is due to the abnormal metabolic state that prevails in DM. Diabetic patients with PAD commonly show involvement in the arteries below the knee, especially at the tibial and peroneal arteries, and involvement in profunda femoris (28). PAD in DM affects both the microcirculation and large vessels.

2.1.3.1 Glucose concentration test

Diabetes can be classified as type 1 or type 2 diabetes. Type 1 diabetes is defined as the pancreas does not produce any insulin and Type 2 diabetes is defined as the pancreas does not produce enough insulin or the body's cells do not react to insulin. Two glucose tests may be used for screening and diagnosis of these 2 types of diabetes. (A) Fasting glucose (fasting blood glucose, FBG) test measures the level of glucose in blood after fasting for at least 8 hours. (B) 2-hour glucose tolerance test (GTT). GTT is performed in the following

procedures. Firstly, the subject has to do a fasting glucose test, and then drinks a 75-gram glucose drink. Another blood sample is drawn 2 hours after the glucose drink is taken. This test examines how the subject's body processes glucose. Under normal condition, the blood glucose level rises after the drink and stimulates the pancreas to release insulin into the bloodstream. Insulin allows glucose to be taken up by cells. As time passes, the blood glucose level is expected to decrease again. However, when a subject is unable to produce enough insulin, or if the body's cells are resistant to its effects, which is known as insulin resistance, then less glucose is transported from the blood into cells and the blood glucose level remains high. This subject will then be diagnosed with diabetes.

2.1.3.2 Haemoglobin A1c (HbA1c) test

Hemoglobin A1c, also called A1c or glycated hemoglobin, is a type of hemoglobin with glucose attached. The A1c test evaluates the average amount of glucose in blood over the last two to three months by measuring the percentage of glycated (glycosylated) hemoglobin. The higher the level of glucose in the blood, the more glycated hemoglobin is formed. Once the glucose binds to the hemoglobin, it remains there for the life of the red blood cell and the duration is normally about 120 days. The predominant form of glycated hemoglobin is known as A1c. A1c is produced on a daily basis and slowly cleared from the blood as older red blood cells die and younger red blood cells (with non-glycated hemoglobin) take their place.

2.1.3.3 Perfusion quantification of DM

Perfusion quantification of DM (29) is an important tool for diagnosis and therapy. This disease would affect the capillary perfusion such as the microcirculation in muscle due to insulin resistance. The perfusion quantification is similar to PAD where the perfusion at a

microcirculatory level is assessed. Although DM can be diagnosed by GTT and HbA1c test, they cannot assess perfusion at a microcirculatory level and locate the damaged vessels, which would be the critical information for vascular damage. Perfusion quantification could help to quantify and visualise the vessels which are affected by DM. This quantitative information could be useful for monitoring the affected vessels over time as well as evaluating treatment performance. Current available technology such as Arterial Spin-Labeling (ASL) MRI could provide muscle blood flow (30). However, it is still not clear whether this technology can estimate microvascular function. On the other hand, CEUS could provide additional and valuable perfusion information in DM, which is similar to perfusion quantification in PAD. An accurate and reliable quantification in CEUS is therefore in great urgency.

2.1.3.4 Medical treatment – Medications, diabetic diet and exercise

The major goal in treating type 1 and type 2 diabetes is to regulate the blood sugar (glucose) level within the normal range. This can be done by either insulin uptake, exercise or diet control. Insulin causes cells in the liver, muscle, and fat tissue to take up glucose from blood and convert it to glycogen that can be stored in liver and muscles. Then, the blood sugar level will decrease. Weight reduction and exercise can treat type 2 diabetes effectively. They increase the body's sensitivity to insulin, thus help to control blood sugar elevations.

2.2 Current Medical Imaging Modalities of Atherosclerosis, PAD and DM

In this section, current medical imaging modalities of Atherosclerosis, PAD and DM are introduced. This includes Magnetic Resonance Imaging (MRI), Ultrasound (US) and Contrast Enhanced Ultrasound (CEUS).

2.2.1 Magnetic Resonance Imaging

Magnetic Resonance Imaging (MRI) is an imaging modality that used in vascular imaging based on the concept that protons precess in a magnetic field. For example, in order to image tissue, a changing magnetic field is applied within that region so that the protons are rotated at a resonant frequency. To construct the final image, the signals from the protons are detected and analysed by Fourier analysis.

MRI can be used to assess morphologic and functional peripheral vascular status and vascular adaptations over a period of time in patients with peripheral arterial disease (26). Quantification of morphological vascular status can be done by contrast-enhanced MR angiography as well as phase contrast angiography MRI. They can be used to evaluate most of the major arteries in the body. One drawback of MR angiography is that it does not evaluate small vessels or extremely slow blood flow. Dynamic contrast-enhanced (DCE) MRI and functional magnetic resonance imaging (fMRI) can be used to assess the functional vascular status. However, they are very sensitive to motion artefacts and could produce poor images. Furthermore, MRI is also a common imaging modality for plaque imaging. It can be used to characterise carotid plaque (31) which allows categorisation of carotid stenosis into different lesion types. Therefore, patients with asymptomatic carotid artery stenosis who have an increased risk for future cerebral events can be identified. However, this technique has limited spatial resolution.

MR perfusion imaging (32, 33) offers an alternative technique for measuring brain perfusion in acute stroke patients. It represents a form of functional imaging that assesses alterations in blood flow with additional information on metabolism and regional measures of a specific tracer. It can be used to identify affected brain tissue for therapy. Measurement of perfusion is based on analysis of a hemodynamic time-to-signal intensity curve generated when a tracer passes through the cerebral circulation. This curve can be further processed to extract parameters that reflect either the cerebral blood flow (CBF), cerebral blood volume (CBV) or mean transit time (MTT). The advantage of MRI perfusion imaging is that it is sensitive and relatively specific in detecting changes that occur after such strokes. However, one limitation of this technique is that the presence of hemorrhage in acute strokes which may create signal distortion resulting in artifactual perfusion measurements in that region.

Another MRI technique, Arterial Spin Labeling (ASL) Magnetic Resonance Imaging, can be used to measure muscle blood flow in patients with PAD. Pollak et al. (30) demonstrated that this technique could quantify peak exercise blood flow in calf muscle. This non-contrast technique may be useful for clinical trials of therapies for improving muscle perfusion, especially in patients who are unable to receive gadolinium. The drawback of this technique is that it cannot measure resting calf muscle perfusion due to low resting calf blood flow.

MRI has several disadvantages in general. MRI examination is expensive and not accessible. e.g. to the patients' bedside.

2.2.2 Ultrasound

Ultrasound (US) has been used in vascular imaging. Conventional B-mode and Doppler ultrasound are used to detect changes in the carotid artery wall and provide information for clinicians to decide if any treatment is needed (34). B-mode imaging is a technique that uses pulsed high frequency sound waves and their echoes. The principle is that ultrasound pulses are sent from transducer and propagate through targeted tissues. Sound waves are then reflected to the transducer. This is known as echo. B-mode imaging allows visualisation and quantification of anatomical structures. When studying blood flow and muscle motion, Doppler ultrasound is commonly used. It is a non-invasive test that can be used to measure blood flow by bouncing high-frequency sound waves off circulating red blood cells.

To achieve pulse-echo in ultrasound imaging, a transducer containing piezoelectric crystals converts electrical energy to sound for pulse generation, and converts acoustic energy in the echo to electrical energy to form an image. Broad bandwidth technology produces medical transducers that can generate pulses containing more than one operating frequency. These frequency ranges used in medical ultrasound imaging are from 2MHz to 15MHz (35).

Ultrasound interacts with tissues through different physical processes. They are reflection, scattering, refraction and absorption. Reflection is the most important interaction process for the purpose of generating an ultrasound image. When a beam of ultrasound strikes an acoustic boundary, part of the beam energy is transmitted across the boundary, while some is redirected backwards or reflected. Two types of reflection can occur, depending on the size of the boundary relative to that of the ultrasound beam. Specular reflections occur when the boundary is smooth and larger than the beam dimensions, while non-specular reflections

occur when the interface is smaller than the beam. It is also known as scattering. Scattering occurs when the reflecting interface is irregular in shape, and its dimensions are smaller than the ultrasound wavelength, the incident beam is reflected in many different directions. Refraction is a change of beam direction at a boundary between two media in which ultrasound travels at different velocities. It is caused by a change of wavelength as the ultrasound passes from one medium to the other while the beam frequency remains unchanged. It does not contribute to the process of image formation, but may contribute to imaging artefacts. Absorption is a process that energy in the ultrasound beam is transferred to the propagating medium, where it is transformed into different forms of energy such as heat. This process is affected by (A) the viscosity of the medium, (B) the relaxation time of the medium and (C) the beam frequency (36).

US is very useful in morphological characterisation of plaques depending on their size and composition (37). However, B-mode carotid ultrasound has several limitations. It cannot detect the various features of a vulnerable plaque such as the composition of the plaque. Specifically it does not provide information about adventitial vasa vasorum, intraplaque neovascularisation and inflammation, which are already identified as crucial diagnostic factors of early carotid plaque rupture (38, 39). Moreover, the complex three dimensional structure of the plaque makes the accurate morphological quantification difficult (40). Also, Doppler ultrasound is limited by low temporal and spatial resolution, angle dependence and susceptibility to artefacts (41). This may lead to either an over- or under-estimation of a carotid lesion resulting in misinterpretation of the need for a surgery.

2.2.3 Contrast Enhanced Ultrasound

Contrast enhanced ultrasound (CEUS) is a new technique that provides additional clinical information on top of the conventional ultrasound. It uses microbubbles to enhance the ultrasound backscatter from within the blood. It produces a unique image with increased contrast due to the high echogenicity of the contrast agents and provides a means of visualising and quantifying tissue perfusion. This technique opens up a new opportunity to image the microcirculation.

There are a number of different agents. First-generation microbubbles were air filled microspheres. Because of the high solubility of air in blood and a thin (10–15 nm) protein shell coat that is not a good barrier against gas diffusion, they disappear from the bloodstream within seconds after administration. To improve the stability of microbubbles, the second generation of microbubbles were developed. They are filled with a heavy-molecular-weight gas e.g. sulphur hexafluoride, with decreased solubility, therefore, improving stability under higher pressure (42).

Typically, a "microbubble", one of the ultrasonic contrast agents, contains air or high-molecular weight low-solubility gas encapsulated in a lipid or albumin shell. When the bubbles are injected into blood, they vibrate in an ultrasound field. The wall of the bubble is displaced asymmetrically during the increase and decrease of acoustic pressure. This generates a non-linear response which in turn generates harmonic frequencies that can be electronically separated from the frequency signatures from tissue echoes. As a result, the echoes from the blood in which bubbles are suspended are greatly enhanced and hence the contrast is significantly improved. This enables the imaging of the micro-vascularisation. The

accurate measurement of the concentration of bubbles and how it changes over time can provide valuable information in clinical investigations.

The enhancement of the ultrasound echo given by microbubbles is widely used in B-mode and Doppler imaging. Also, it provides a way to perform functional studies by tracking the flow of a microbubble bolus through a region of interest. Recently, new agents are being developed for target therapy and drug delivery. Pharmaceutical drugs are attached to a microbubble and then released locally by disrupting the bubbles by using a high power ultrasound beam. They can be burst ultrasonically at the target site to release the drug in a high concentration while the remainder of the body receives only small amount of dilute drug. As a result, the therapeutic treatment is improved (42).

In the context of carotid artery disease, spatial and temporal distribution of microbubbles can effectively reflect plaque vulnerability (43). Firstly, CEUS enhances the carotid lumen allowing a much clearer visualisation of CIMT and plaque morphology (44, 45), as shown in Figure 2-7. Secondly, contrast agents circulate as ideal intravascular tracers enabling the microvascular assessment of the adventitial and intraplaque neovascularisation (46, 47). CEUS imaging can also be performed non-invasively in real time and as a low cost alternative to more expensive modalities such as MRI angiography (48, 49). Therefore, CEUS could be a promising imaging technique in the reliable screening of the risk of stroke.

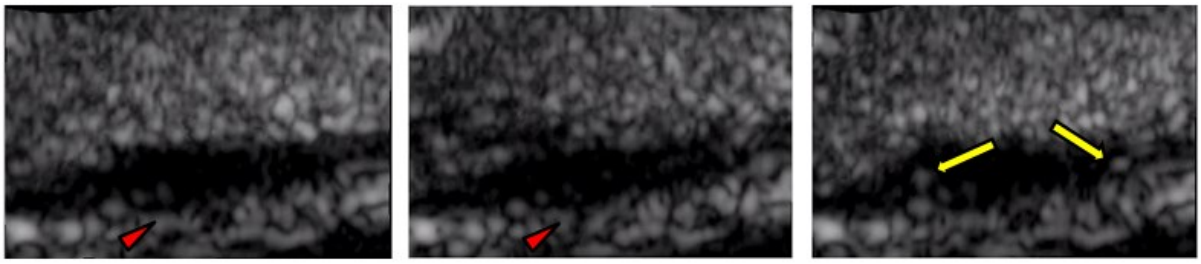

Figure 2-7: Zoom of consecutive frames of this lesion with visible microbubbles in the adventitial tissue (red arrow) and within the plaque (long yellow arrow)

Microbubble agents provide additional benefits to obtain quantitative information relating to tissue vascularisation and perfusion. This imaging technique has great potential and promise for diagnosis, monitoring, and therapy of vascular diseases and cancer.

2.3 Limitations of Current Quantification in CEUS

In this section, the limitations of current quantification in CEUS are discussed. These include motion, intensity-based quantification, attenuation and nonlinear artefacts and temporal-based quantification.

2.3.1 Motion

Motion correction is a critical step for accurate quantification. Existing quantification methods are based on spatial and temporal information in the image data to produce quantitative results. However, motion could affect the spatial and temporal information of the targeted region, which may produce unreliable quantitative results. Therefore, a motion compensation method is essential before any quantification method employed.

Several studies (50, 51) used affine motion correction to reduce motion artefacts. The source image needs to be rotated, shifted and sheared with respect to a reference image to achieve maximum alignment. This technique is particularly useful to compensate global motion. However, the local movement of an object is ignored in this method, and hence, it may not be suitable to compensate the movement in some applications such as carotid imaging.

In order to take local motion into account, several studies (52-54) employed non-rigid motion correction to reduce local motion artefacts. The principle is to adopt a deformation model such as free form deformation and allow local deformation of an object by manipulating an underlying mesh of control points. A similarity parameter is defined to measure the alignment of two images. The advantage of this approach is that it does not require any landmark selection, but it may require high computational resources and long execution times to search for the best alignment.

2.3.2 Intensity-based quantification

Recently several groups have developed various methods for IPN quantification. Huang et al. (12) proposed a dynamic evaluation of the plaque enhancement. The enhancement was analysed by a time intensity analysis (TIC). TIC is commonly used in analysing large and well perfused organs, for example, liver, prostate and heart (55-57). However, plaques in carotid artery are often small and weakly perfused, therefore, TIC analysis may not be appropriate to quantify microvessels in plaques. Hoogi et al. (58) used only one CEUS image per cardiac cycle. Hence, the connection of microvessel paths after time integration may be lost. Akkus et al. (59) developed a statistical segmentation of carotid plaque neovascularisation. An iterative expectation-maximisation algorithm was employed to solve a mixture estimation problem and classify the pixel as either background, blooming of contrast,

contrast spots or artefact. Optimisation is required in the iteration, which has a long data processing time. Therefore, there is still an unmet need to develop a fast and accurate quantification method to quantify contrast spots based on image intensity.

Another intensity based image visualisation and quantification method is maximum intensity projection (MIP). It is commonly used in vascular imaging. Several studies (60-62) have employed MIP to extract the arterial path. MIP computes the maximum intensity over time for each pixel. It can be used to identify the structure of the targeted object such as carotid plaques in B-mode images. In CEUS image, this technique provides useful information such as the vessel trajectories. The advantage of this approach is simple and fast, while the disadvantage is that this method is very sensitive to tissue artefact and noise. In particular, it is very difficult to distinguish between tissue artefact and blood vessels in the absence of temporal information, and therefore, it could generate over-estimated vessel paths and affect quantification results. Furthermore, motion significantly affects MIP. Hence, it is necessary to apply a good motion compensation algorithm before using MIP to reconstruct vessel paths.

2.3.3 Attenuation effect and correction

When sound travels through a medium, the intensity will be decreased with the travelled distance. This is known as attenuation. It is a combined result of scattering and absorption. Ultrasonic attenuation follows a decay law of the wave amplitude as it propagates through material. This phenomenon is modelled by this equation,

$$A(z) = A_o e^{-\mu z} \tag{2-1}$$

where μ is the attenuation coefficient of the wave traveling in the z-direction, A is the amplitude of propagating wave. Also, the attenuation coefficient is linearly dependent on frequency. For different types of tissue, the attenuation coefficients are shown in Table 2-1.

Table 2-1: Attenuation coefficient of different tissues at a frequency of 1MHz

Body tissue	**Attenuation Coefficient (dB/cm at 1MHz)**
Water	0.002
Blood	0.18
Fat	0.65
Muscle	1.5-3.5
Bone	5.0

From the Table 2-1, sound wave is more attenuated in the bone, while the attenuation effect is the least in water. This means that sound waves can penetrate easily in water, while not in bone. The quantification of micro-circulation based on CEUS image intensity is significantly influenced by attenuation which, therefore, must be corrected.

Time gain compensation (TGC) is a method to compensate the attenuation effect in ultrasound imaging. This technique is available in commercial scanners. However, the operator has to manually enter pre-set values according to the distance between transducer and tissue. This introduces variability of the image formed. Moreover, this technique mainly improves the visualisation of images, while the improvement of quantification is not addressed. For this reason, several compensation algorithms have been reported in literature. Several studies addressed the method to compensate the attenuation. For example, O'

Donnell (63) and Melton and Skorton (64) proposed a method based on the statistics of image intensities to separate attenuation into two or three levels. However, these methods are not able to perform compensation dynamically for a varying attenuation coefficient.

A number of studies reported automatic attenuation correction in B-mode imaging. For example, McDicken et al (65) proposed a method that integrates the signal from the receiver, then it is inverted and fed back to control the gain. An algorithm was developed by Pye et al (66), it calculated a variable gain function by a smoothing factor such that the mean echo amplitude at a particular depth was equal to a mid-range grey level. Hughes and Duck (67) described echoes as attenuation and backscatter coefficients. They are based on this model to correct the attenuation. Asanuma et al (68) reported the use of harmonic-to-fundamental ratio (HFR) to quantify the tissue perfusion. This method showed potential to achieve the goal of attenuation correction. Yet, the theoretical background was not well understood.

Some studies have been done to correct attenuation in CEUS images in general (69-71), for example, Tang et al (69) developed a mathematical model to manipulate multiple echo measurements so that those unknown parameters related to the attenuation can be largely removed and quantities that are truer representation of bubble concentration can be extracted. This technique did not require additional measurements and could be implemented in real time. Although this method is simple and fast, the in vivo application of it for flow quantification is limited due to its assumptions. Furthermore, there is no study on CEUS images of carotid arteries where accurate quantification of plaque neovascularisation and abnormal proliferation of VV is valuable.

In conclusion, the proposed attenuation correction method can be applied to either high or low quality of CEUS images, which is better than current techniques that require high quality of CEUS images. This is particularly important in the clinical imaging of carotid atherosclerosis due to the need for a quantitative analysis of intraplaque neovascularisation and adventitial vasa vasorum.

2.3.4 Temporal-based quantification

Recently several groups have developed various methods for single bubble detection and tracking by taking advantage of some temporal information. Viessmanns et al. and Christensen-Jeffries et al. used rolling background subtraction to remove unwanted background signals from static structures such as the echo from the tube wall (72, 73). The technique can produce super-resolution images, where vessel structures detected are over five times smaller than the optimal diffraction limited resolution, while the resolution of conventional ultrasound is fundamentally limited by the achievable point spread function (PSF) localization precision. Ackermann et al. adopted a temporal median filtering and foreground/background subtraction to detect and track of multiple microbubbles in ultrasound B-mode image (74). This technique can produce a better image in terms of vessel morphology, and flow velocity is also provided. But, it requires a suitable range of microbubble concentration, which is hard to control in vivo. Errico et al. developed ultrafast ultrasound localization technique for deep super-resolution vascular imaging by exploiting the coherence of backscattered signals, the spatiotemporal filtering approach discriminates slowly moving bubbles of sub-wavelength size (low spatial coherence) from slow motion tissue signals whose temporal variations affect many neighbouring pixels the same way (high

spatial coherence) (75). The method combines deep penetration and super-resolution imaging at unprecedented spatiotemporal resolution, by using clinically approved microbubbles, but the process takes 2 millisecond to form a single image and is more affected by motion than existing real-time imaging techniques. One drawback of this approach is that an appropriate motion compensation technique is required in order to image deep structures. This technique could also be affected by skull-induced signal attenuation, which increases the limit of the smallest detectable blood vessel for brain imaging. Furthermore, there is no quantification method that examines the frequency features of the temporal signal in CEUS image sequences, which could provide a new way of distinguishing and quantifying microbubbles.

Finally, good reproducibility is a key requirement for the clinical translation of any CEUS quantification techniques and this is yet to be fully demonstrated.

2.4 Summary

In this chapter, the medical background on Atherosclerosis, Peripheral Artery Disease and Diabetes Mellitus has been reviewed. These vascular diseases are significant challenges to humans. The clinical need for an imaging tool for imaging and quantifying microvascular flow in these diseases is described. MRI and CEUS are common modalities used in vascular imaging. The technical background on these modalities of mentioned vascular diseases has been reviewed. CEUS has certain advantages over MRI, though various technical issues in CEUS need to be addressed. The current state-of-the-art quantification methods in CEUS have also been reviewed. The current quantification methods have several limitations (i.e. affected by attenuation and poor reproducibility), which limit the usefulness of CEUS in clinical practice.

In the following chapters, computer assisted quantification methods including attenuation correction and sensitivity detection of bubble signals were proposed to overcome the existing limitations in CEUS. Chapter 3 presents the development of an automated attenuation correction and normalisation algorithm to improve the quantification of contrast enhancement in ultrasound images of carotid arteries. Chapter 4 introduces a robust and automated tool for reproducible quantification of microbubble identification in CEUS image sequences using a pixel level temporal and spatial analysis based algorithm. Chapter 5 introduces a new microbubble visualisation and quantification technique for CEUS carotid artery imaging by using a differential intensity mapping. Chapter 6 summarizes the thesis and suggests possible future work.

References

1. Libby P, Ridker PM, Hansson GK**.** Progress and challenges in translating the biology of atherosclerosis. Nature. 2011;473(7347):317-25.
2. van der Wal AC, Becker AE**.** Atherosclerotic plaque rupture - pathologic basis of plaque stability and instability. Cardiovascular Research. 1999;41(2):334-44.
3. Wolf PA, Kannel WB, Sorlie P, McNamara P**.** Asymptomatic carotid bruit and risk of stroke. The Framingham study. JAMA. 1981;245(14):1442-5.
4. Rudd JHF, Davies JR, Weissberg PL**.** Imaging of atherosclerosis - Can we predict plaque rupture? Trends in Cardiovascular Medicine. 2005;15(1):17-24.
5. Touboul PJ, Hennerici MG, Meairs S, et al. Mannheim intima-media thickness consensus. Cerebrovasc Dis. 2004;18(4):346-9.

6. O'Leary DH, Polak JF, Kronmal RA, et al. Carotid-artery intima and media thickness as a risk factor for myocardial infarction and stroke in older adults. New England Journal of Medicine. 1999;340(1):14-22.

7. Geroulakos G, Ramaswami G, Nicolaides A, et al. Characterization of Symptomatic and Asymptomatic Carotid Plaques Using High-Resolution Real-Time Ultrasonography. British Journal of Surgery. 1993;80(10):1274-7.

8. Topol EJ, Nissen SE**.** Our Preoccupation with Coronary Luminology - the Dissociation between Clinical and Angiographic Findings in Ischemic-Heart-Disease. Circulation. 1995;92(8):2333-42.

9. Virmani R, Burke AP, Farb A, Kolodgie FD**.** Pathology of the vulnerable plaque. Journal of the American College of Cardiology. 2006;47(8):C13-C8.

10. Hellings WE, Peeters W, Moll FL, et al. Composition of Carotid Atherosclerotic Plaque Is Associated With Cardiovascular Outcome A Prognostic Study. Circulation. 2010;121(17):1941-U111.

11. Sluimer JC, Daemen MJ**.** Novel concepts in atherogenesis: angiogenesis and hypoxia in atherosclerosis. Journal of Pathology. 2009;218(1):7-29.

12. Huang PT, Huang FG, Zou CP, et al. Contrast-enhanced sonographic characteristics of neovascularization in carotid atherosclerotic plaques. J Clin Ultrasound. 2008;36(6):346-51.

13. McCarthy MJ, Loftus IM, Thompson MM, et al. Angiogenesis and the atherosclerotic carotid plaque: An association between symptomatology and plaque morphology. Journal of Vascular Surgery. 1999;30(2):261-8.

14. Williams JK, Heistad DD**.** Structure and function of vasa vasorum. Trends in Cardiovascular Medicine. 1996;6(2):53-7.

15. Fleiner M, Kummer M, Mirlacher M, et al. Arterial neovascularization and inflammation in vulnerable patients - Early and late signs of symptomatic atherosclerosis. Circulation. 2004;110(18):2843-50.

16. Herrmann J, Lerman LO, Rodriguez-Porcel M, et al. Coronary vasa vasorum neovascularization precedes epicardial endothelial dysfunction in experimental hypercholesterolemia. Cardiovascular Research. 2001;51(4):762-6.

17. Staub D, Schinkel AF, Coll B, et al. Contrast-enhanced ultrasound imaging of the vasa vasorum: from early atherosclerosis to the identification of unstable plaques. JACC Cardiovasc Imaging. 2010;3(7):761-71.

18. Moulton KS**.** Angiogenesis in atherosclerosis: gathering evidence beyond speculation. Current Opinion in Lipidology. 2006;17(5):548-55.

19. Mofidi R, Crotty TB, McCarthy P, et al. Association between plaque instability, angiogenesis and symptomatic carotid occlusive disease. British Journal of Surgery. 2001;88(7):945-50.

20. Dunmore BJ, McCarthy MJ, Naylor AR, Brindle NPJ**.** Carotid plaque instability and ischemic symptoms are linked to immaturity of microvessels within plaques. Journal of Vascular Surgery. 2007;45(1):155-9.

21. Folkman J**.** Tumor angiogenesis: therapeutic implications. N Engl J Med. 1971;285(21):1182-6.

22. Ross JS, Stagliano NE, Donovan MJ, et al. Atherosclerosis: a cancer of the blood vessels? Am J Clin Pathol. 2001;116 Suppl:S97-107.

23. Mas J, Chatellier G, Beyssen B, et al. Endarterectomy versus stenting in patients with symptomatic severe carotid stenosis. New England Journal of Medicine. 2006;355(16):1660-71.

24. Biasi GM, Froio A, Diethrich EB, et al. Carotid plaque echolucency increases the risk of stroke in carotid stenting: the Imaging in Carotid Angioplasty and Risk of Stroke (ICAROS) study. Circulation. 2004;110(6):756-62.

25. Wang JC, Criqui MH, Denenberg JO, et al. Exertional leg pain in patients with and without peripheral arterial disease. Circulation. 2005;112(22):3501-8.

26. Versluis B, Backes WH, van Eupen MG, et al. Magnetic resonance imaging in peripheral arterial disease: reproducibility of the assessment of morphological and functional vascular status. Invest Radiol. 2011;46(1):11-24.

27. Jude EB, Eleftheriadou I, Tentolouris N**.** Peripheral arterial disease in diabetes--a review. Diabet Med. 2010;27(1):4-14.

28. Jude EB, Oyibo SO, Chalmers N, Boulton AJ**.** Peripheral arterial disease in diabetic and nondiabetic patients: a comparison of severity and outcome. Diabetes Care. 2001;24(8):1433-7.

29. Barrett EJ, Rattigan S**.** Muscle Perfusion Its Measurement and Role in Metabolic Regulation. Diabetes. 2012;61(11):2661-8.

30. Pollak AW, Meyer CH, Epstein FH, et al. Arterial spin labeling MR imaging reproducibly measures peak-exercise calf muscle perfusion: a study in patients with peripheral arterial disease and healthy volunteers. JACC Cardiovasc Imaging. 2012;5(12):1224-30.

31. Esposito-Bauer L, Saam T, Ghodrati I, et al. MRI plaque imaging detects carotid plaques with a high risk for future cerebrovascular events in asymptomatic patients. PLoS One. 2013;8(7):e67927.

32. Calamante F, Gadian DG, Connelly A**.** Quantification of perfusion using bolus tracking magnetic resonance imaging in stroke - Assumptions, limitations, and potential implications for clinical use. Stroke. 2002;33(4):1146-51.

33. Fisher M, Prichard JW, Warach S**.** New magnetic resonance techniques for acute ischemic stroke. JAMA. 1995;274(11):908-11.

34. Handa N, Matsumoto M, Maeda H, et al. Ultrasonic evaluation of early carotid atherosclerosis. Stroke. 1990;21(11):1567-72.

35. Gill R**.** The Physics and Technology of Diagnostic Ultrasound: a Practitioner's Guide; 2012.

36. Hill CR, Bamber JC, ter Haar GR**.** Physical Principles of Medical Ultrasonics; 2004.

37. Reilly LM, Lusby RJ, Hughes L, et al. Carotid Plaque Histology Using Real-Time Ultrasonography - Clinical and Therapeutic Implications. American Journal of Surgery. 1983;146(2):188-93.

38. Koenig W, Khuseyinova N**.** Biomarkers of atherosclerotic plaque instability and rupture. Arterioscler Thromb Vasc Biol. 2007;27(1):15-26.

39. Shalhoub J, Owen DRJ, Gauthier T, et al. The use of Contrast Enhanced Ultrasound in Carotid Arterial Disease. European Journal of Vascular and Endovascular Surgery. 2010;39(4):381-7.

40. Arroyo LH, Lee RT**.** Mechanisms of plaque rupture: mechanical and biologic interactions. Cardiovascular Research. 1999;41(2):369-75.

41. Clevert DA, Sommer WH, Zengel P, et al. Imaging of carotid arterial diseases with contrast-enhanced ultrasound (CEUS). European Journal of Radiology. 2011;80(1):68-76.

42. Duck FA, Baker AC, Starritt HC**.** Ultrasound in Medicine. 1998.

43. Sestier FJ, Mildenberger RR, Klassen GA**.** Role of Autoregulation in Spatial and Temporal Perfusion Heterogeneity of Canine Myocardium. American Journal of Physiology. 1978;235(1):H64-H71.

44. Macioch JE, Katsamakis CD, Robin J, et al. Effect of contrast enhancement on measurement of carotid artery intimal medial thickness. Vascular Medicine. 2004;9(1):7-12.

45. Kono Y, Pinnell SP, Sirlin CB, et al. Carotid arteries: Contrast-enhanced US angiography preliminary clinical experience. Radiology. 2004;230(2):561-8.

46. Feinstein SB**.** The powerful microbubble: from bench to bedside, from intravascular indicator to therapeutic delivery system, and beyond. American Journal of Physiology-Heart and Circulatory Physiology. 2004;287(2):H450-H7.

47. Staub D, Patel MB, Tibrewala A, et al. Vasa Vasorum and Plaque Neovascularization on Contrast-Enhanced Carotid Ultrasound Imaging Correlates With Cardiovascular Disease and Past Cardiovascular Events. Stroke. 2010;41(1):41-7.

48. Caplice NM, Martin K**.** Contrast-Enhanced Ultrasound and the Enigma of Plaque Neovascularization. Jacc-Cardiovascular Imaging. 2010;3(12):1273-5.

49. Coll B, Nambi V, Feinstein SB**.** New advances in noninvasive imaging of the carotid artery: CIMT, contrast-enhanced ultrasound, and vasa vasorum. Curr Cardiol Rep. 2010;12(6):497-502.

50. Briechle K, Hanebeck UD**.** Template matching using fast normalized cross correlation. Optical Pattern Recognition Xii. 2001;4387:95-102.

51. Golemati S, Sassano A, Lever MJ, et al. Carotid artery wall motion estimated from B-mode ultrasound using region tracking and block matching. Ultrasound in Medicine and Biology. 2003;29(3):387-99.

52. Lee S, Wolberg G, Shin SY**.** Scattered data interpolation with multilevel B-splines. Ieee Transactions on Visualization and Computer Graphics. 1997;3(3):228-44.

53. Rueckert D, Sonoda LI, Hayes C, et al. Nonrigid registration using free-form deformations: Application to breast MR images. Ieee Transactions on Medical Imaging. 1999;18(8):712-21.

54. Myronenko A, Song XB, Sahn DJ**.** Maximum Likelihood Motion Estimation in 3D Echocardiography through Non-rigid Registration in Spherical Coordinates. Functional Imaging and Modeling of the Heart, Proceedings. 2009;5528:427-36.

55. Goossen TEB, de la Rosette JJMCH, de Kaa CAHV, et al. The value of dynamic contrast enhanced power Doppler ultrasound Imaging in the localization of prostate cancer. European Urology. 2003;43(2):124-31.

56. Claudon M, Dietrich CF, Choi BI, et al. Guidelines and good clinical practice recommendations for Contrast Enhanced Ultrasound (CEUS) in the liver - update 2012: A WFUMB-EFSUMB initiative in cooperation with representatives of AFSUMB, AIUM, ASUM, FLAUS and ICUS. Ultrasound Med Biol. 2013;39(2):187-210.

57. Wei K, Jayaweera AR, Firoozan S, et al. Quantification of myocardial blood flow with ultrasound-induced destruction of microbubbles administered as a constant venous infusion. Circulation. 1998;97(5):473-83.

58. Hoogi A, Akkus Z, van den Oord SC, et al. Quantitative analysis of ultrasound contrast flow behavior in carotid plaque neovasculature. Ultrasound Med Biol. 2012;38(12):2072-83.

59. Akkus Z, Bosch JG, Sánchez-Ferrero GV, et al. Statistical segmentation of carotid plaque neovascularization. SPIE Medical Imaging, 2013. International Society for Optics and Photonics: 867506--12.

60. Hoogi A, Adam D, Hoffman A, et al. Carotid plaque vulnerability: quantification of neovascularization on contrast-enhanced ultrasound with histopathologic correlation. AJR Am J Roentgenol. 2011;196(2):431-6.

61. van Ooijen PM, Ho KY, Dorgelo J, Oudkerk M**.** Coronary artery imaging with multidetector CT: visualization issues. Radiographics. 2003;23(6):e16.

62. Suri JS, Liu KC, Reden L, Laxminarayan S**.** A review on MR vascular image processing: Skeleton versus nonskeleton approaches: part II. Ieee Transactions on Information Technology in Biomedicine. 2002;6(4):338-50.

63. Odonnell M**.** Quantitative Volume Backscatter Imaging. Ieee Transactions on Sonics and Ultrasonics. 1983;30(1):26-36.

64. Melton HE, Skorton DJ**.** Rational Gain Compensation for Attenuation in Cardiac Ultrasonography. Ultrasonic Imaging. 1983;5(3):214-28.

65. Mcdicken WN, Evans DH, Robertso.Da**.** Automatic Sensitivity Control in Diagnostic Ultrasonics. Ultrasonics. 1974;12(4):173-6.

66. Pye SD, Wild SR, Mcdicken WN**.** Adaptive Time Gain Compensation for Ultrasonic-Imaging. Ultrasound in Medicine and Biology. 1992;18(2):205-12.

67. Hughes DI, Duck FA**.** Automatic attenuation compensation for ultrasonic imaging. Ultrasound in Medicine and Biology. 1997;23(5):651-64.

68. Asanuma T, Viggen K, Seward JB, Belohlavek M**.** Dual-spectra ultrasonography - An attenuation-compensating technique for myocardial perfusion analysis. Journal of Ultrasound in Medicine. 2002;21(3):249-59.

69. Tang MX, Mari JM, Wells PNT, Eckersley RJ**.** Attenuation Correction in Ultrasound Contrast Agent Imaging: Elementary Theory and Preliminary Experimental Evaluation. Ultrasound in Medicine and Biology. 2008;34(12):1998-2008.

70. Mule S, De Cesare A, Lucidarme O, et al. Regularized estimation of contrast agent attenuation to improve the imaging of microbubbles in small animal studies. Ultrasound in Medicine and Biology. 2008;34(6):938-48.

71. Mari JM, Hibbs K, Stride E, et al. An Approximate Nonlinear Model for Time Gain Compensation of Amplitude Modulated Images of Ultrasound Contrast Agent Perfusion. Ieee Transactions on Ultrasonics Ferroelectrics and Frequency Control. 2010;57(4):818-29.

72. Christensen-Jeffries K, Browning RJ, Tang MX, et al. In Vivo Acoustic Super-Resolution and Super-Resolved Velocity Mapping Using Microbubbles. Ieee Transactions on Medical Imaging. 2015;34(2):433-40.

73. Viessmann OM, Eckersley RJ, Christensen-Jeffries K, et al. Acoustic super-resolution with ultrasound and microbubbles. Physics in Medicine and Biology. 2013;58(18):6447-58.

74. Ackermann D, Schmitz G**.** Detection and Tracking of Multiple Microbubbles in Ultrasound B-Mode Images. IEEE Trans Ultrason Ferroelectr Freq Control. 2016;63(1):72-82.

75. Rrico CE, Pierre J, Pezet S, et al. Ultrafast ultrasound localization microscopy for deep super-resolution vascular imaging. Nature. 2015;527(7579):499-+.

Chapter 3

Attenuation correction and normalisation for quantification of contrast enhancement in ultrasound images of carotid arteries

An automated attenuation correction and normalisation algorithm was developed to improve the quantification of contrast enhancement in ultrasound images of carotid arteries. The algorithms firstly corrects attenuation artefact and normalises intensity within the contrast agent-filled lumen and then extends the correction and normalisation to regions beyond the lumen. The algorithm was firstly validated on phantoms consisting of contrast agent-filled vessels embedded in tissue mimicking materials of known attenuation. It was subsequently applied to in vivo contrast enhanced ultrasound (CEUS) images of human carotid arteries. Both in vitro and in vivo results show significant reduction in the shadowing artefact and improved homogeneity within the carotid lumens after the correction. The error in quantification of contrast enhancement due to attenuation on phantoms was reduced from 49% to 12% on average. In conclusion the proposed method show great potential in reducing attenuation artefact and improving quantification in contrast enhanced ultrasound of carotid arteries. This work was done in collaboration with Dr Dorothy M. Gujral from the Head and Neck Unit, the Royal Marsden Hospital, where she focused on the application of the attenuation and normalisation technique to study contrast enhancement of carotid adventitial vasa vasorum as a biomarker of radiation-induced atherosclerosis. Part of her results are included in this chapter.

3.1 Introduction

Stroke is a major cause of mortality, morbidity and long-term disability, resulting in a substantial economic burden on health and social services (1). Carotid atherosclerotic plaque is one of the major preventable causes of stroke (2). Plaques at risk of rupture (vulnerable plaques) are not necessarily those which impinge most substantially upon the lumen (3). Nevertheless, current clinical imaging investigations still focus on quantifying the degree of luminal stenosis, and hence are relatively poor at predicting which patients will suffer a stroke. Recent studies have identified plaque neovascularisation as being a key feature of vulnerable plaques (4, 5). Furthermore, abnormal proliferation of adventitial vasa vasorum (VV) occurs early at sites of atherosclerosis and is thought to be a precursor to atherosclerosis and an early biomarker of vascular damage (6, 7). An imaging tool capable of detecting and quantifying such vascular features would offer valuable information for the diagnosis and management of this important disease.

Ultrasonography (US) is regarded as one of the most promising tools in assisting diagnosis and management of carotid artery disease due to its non-ionizing nature and real-time imaging in good spatial resolution, with relatively low cost and high accessibility. Recently, contrast-enhanced ultrasound (CEUS) has made it possible to image and quantify neovascularisation in plaques as well as adventitial VV (7). However, current quantification of contrast enhancement is significantly limited by spatially heterogeneous and patient-specific attenuation (8, 9). During a US scan, the ultrasound echo from a target is affected by attenuation between the US transducer and the target. Time Gain Compensation (TGC) is commonly used for correcting attenuation where echo signals are amplified as a function of

time so the further the echoes come from the higher the signal gain. However, such TGC cannot account for spatially heterogeneous attenuation caused by either heterogeneous tissue distribution or non-uniform contact between the probe and skin. It is also difficult for TGC to account for variations of tissue attenuating properties across patient populations. Consequently, it is common to see 1) shadowing in vascular ultrasound images (e.g. see Figure 3-1), a manifestation of spatially heterogeneous attenuation; and 2) variations of image intensity between patients, a manifestation of population variation. It should be noted that attenuation may not be visually identifiable due to image compression at display but can still cause significant errors in quantification based on image intensity, which limits the usefulness of quantification of CEUS in clinical applications. While some studies have been done to correct attenuation in CEUS images in general (9-11), we are not aware of any study on CEUS images of carotid arteries where accurate quantification of plaque neovascularisation and abnormal proliferation of VV is valuable.

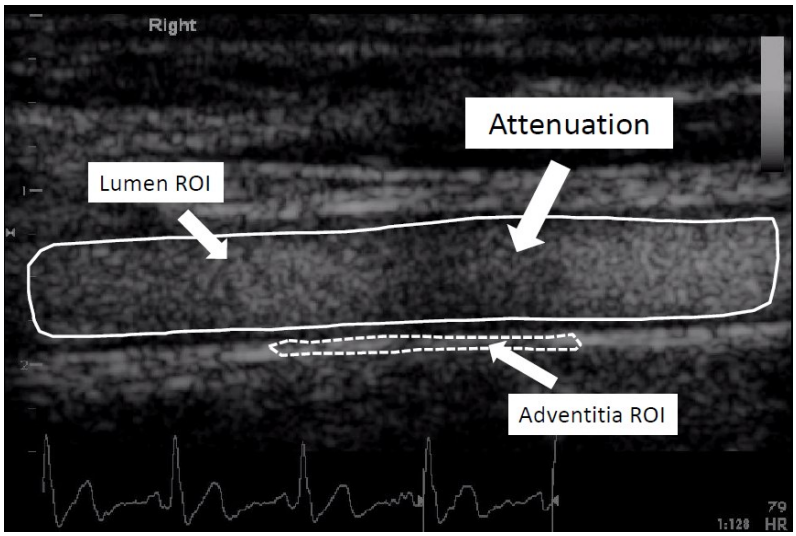

Figure 3-1: ROIs in the lumen (solid line) and vessel wall (dash line)

The objective of this study was to develop an attenuation correction and normalisation technique for CEUS carotid artery imaging in order to correct for spatially heterogeneous and

patient-specific attenuation and thus improve the quantification of contrast enhancement in plaques and VV. This technique was initially validated on a carotid artery-mimicking phantom and then, as an initial clinical demonstration, applied to ultrasound contrast enhancement in carotid artery vessel wall in a cohort of patients.

3.2 Materials and Methods

3.2.1 Attenuation correction and image normalisation algorithms

An attenuation correction algorithm for CEUS carotid artery images was developed based on the assumption that microbubble contrast agents are well mixed in the lumen and, hence, the image intensity across the vessel lumen should be homogeneous (except for intensity variations due to speckles) if attenuation is properly corrected for. Microbubbles, when injected intravenously, are expected to have been well mixed in the flow when they arrive at the carotid artery. Based on this assumption, the algorithm initially estimates and corrects for the attenuation within the carotid lumen, and then extends the correction at the lumen boundary to the vessel wall next to the lumen. Furthermore, the images are normalised so that quantification of contrast enhancement is less affected by variations in patient dose of contrast agents.

Analysis of CEUS video sequences was performed offline using software developed in-house using Matlab (The Mathworks Inc., Natick, MA, USA). Regions of interest (ROIs) were selected manually, one to segment the lumen and the others to include regions in the adventitia where quantification is required (Figure 3-1). The motion of the lumen and adventitia ROIs in the video sequence was tracked and corrected by employing a piece-wise

block matching algorithm (12, 13). As a result of motion correction, all images in the sequence were aligned to the first image.

The attenuation correction algorithm consists of the following specific steps. All computations were performed on linearised video data. The video data are log-compressed and linearized video data refers to the anti-log decompressed video data.

(1) Based on the segmented lumen, the relative smoothed intensity profile A, which is a function of accumulated attenuation within the lumen was estimated by adopting a low pass Gaussian filter (9) as shown in equation (3-1)

$$A_{lumen}(x,y) = I_{lumen}(x,y) * G(x,y) \tag{3-1}$$

where $G(x,y) = \frac{1}{2\pi\sigma^2} \cdot e^{-\frac{x^2+y^2}{2\sigma^2}}$, x and y are spatial coordinates, $*$ denotes convolution

The choice of σ, the standard deviation of the Gaussian kernel, depends on the imaging settings. Here the standard deviation is set to be at least twice the speckle size measured on the image for both phantom and in vivo studies. Such a filter diminishes the speckles and leaves the spatially smoothed intensity profile.

One issue with the filtering is that at the boundary of the lumen the filter covers pixels outside the lumen. To resolve this issue, a mirror image approach was adopted, i.e. the pixels outside the bounds of the lumen were computed by mirror-reflecting the lumen across the lumen border. This was done by using a MATLAB function *imfilter* with boundary condition *symmetric*.

(2) The attenuation correction was performed within the segmented lumen as shown in equation (3-2)

$$CI_{lumen}(x,y) = I_{lumen}(x,y) / (A_{lumen}(x,y) + \text{regulariser}) \quad (3\text{-}2)$$

where $CI_{lumen}(x,y)$ denotes corrected image within the lumen

The regulariser is a constant which avoids the over-amplification of noise when A_{lumen} in the denominator in equation (3-2) becomes close to zero. It plays a crucial role in this correction process as too large a regulariser would leave the image uncorrected while too small a regulariser would cause overcompensation due to noise. In this study, the value of the regulariser is set at 0.08 for the phantom study and 0.1 for the in vivo study. These values are obtained by minimising the normalised intensity fluctuation (NIF) within the corrected lumen defined as follows:

$$NIF = \frac{\sqrt{\sum(CI(x,y) - \langle CI(x,y)\rangle)^2}}{\langle CI(x,y)\rangle} \quad (3\text{-}3)$$

where CI is the intensity of pixel at position (x,y), $\langle CI(x,y)\rangle$ is the spatial average intensity within corrected lumen. The variation of this index as a function of the regulariser for the phantom study is shown in Figure 3-2.

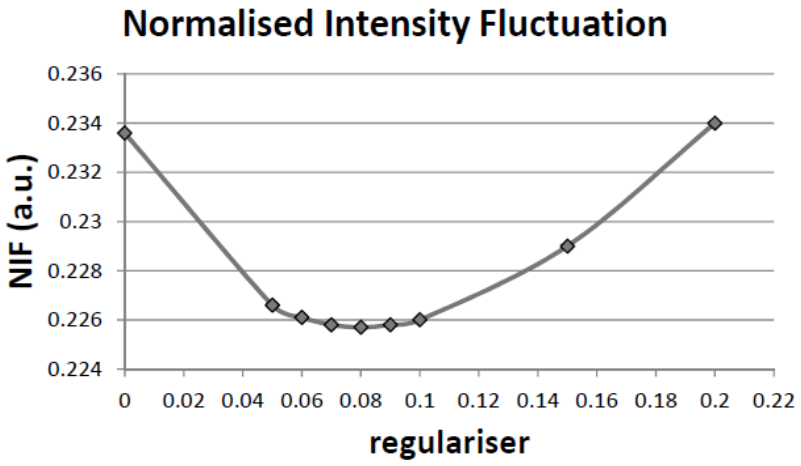

Figure 3-2: Normalised intensity fluctuation within corrected lumen

(3) Based on the estimated $CI_{lumen}(x,y)$ which covers the whole lumen, the correction factors at the lower (A_{lb}) and upper boundaries (A_{ub}) of the lumen were extended to regions below (I_{lr}) and above the lumen (I_{ur}) including the adventitia, using equation (3-4)

$$CI_{ur}(x,y) = I_{ur}(x,y) / (A_{ub}(x,y) + \text{regulariser})$$
$$CI_{lr}(x,y) = I_{lr}(x,y) / (A_{lb}(x,y) + \text{regulariser}) \quad (3\text{-}4)$$

3.2.2 Image normalisation

The image is then normalised by the mode intensity within the lumen. After normalisation, the peak in the lumen intensity histogram is located at intensity equal to one. This is to reduce the variations in CEUS quantification caused by variations in both tissue attenuation properties and contrast concentration in different subjects.

3.2.3 Evaluation of lumen intensity homogeneity

As a first step to evaluate the attenuation correction algorithm, image intensity histograms were generated to characterise the change of intensity homogeneity within the lumen before and after the correction. FWHM of the peak in the lumen intensity histogram is calculated as a measure of lumen intensity homogeneity.

3.2.4 Phantom set-up and validation

The attenuation correction algorithm was first validated on a carotid artery-mimicking phantom constructed in-house and shown in Figure 3-3. It consisted of two contrast agent-filled vessels embedded in a tissue-mimicking phantom (TMM2) (14). The first vessel is to

simulate the carotid artery, and the second is 1cm below the first, to represent target regions containing microbubble contrast agents whose concentration needs to be quantified. An additional attenuating material (TMM1) was placed under the probe and covering half of the TMM2, causing additional attenuation to only half of the phantom. While the upper vessel was to mimick the carotid artery, the lower vessel was to create a region with controlled bubble concentration. Given that the microbubbles were well mixed and the TMM under the tube are homogeneous, such a setup offers both measurements with attenuation (left hand side (LHS)) and control measurements (right hand side (RHS)) within the same image acquisition and any extra signal loss on the LHS of the phantom compared to the RHS is due to the attenuation caused by the additional attenuation material.

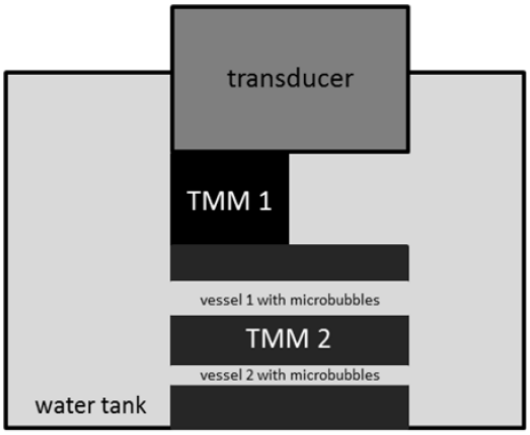

Figure 3-3: Carotid artery-mimicking set-up with additional attenuation material (TMM1) on the left hand side of the phantom

The TMM1 and TMM2 were made according to the protocol of (14). The estimated attenuation of the TMM1 or TMM2 was 0.5 $dBcm^{-1}MHz^{-1}$. Homemade lipid shell microbubbles were used in two concentrations: 7.50×10^{6}/ml and 3.75×10^{6}/ml. A Toshiba AplioXG scanner (PLT-704SBT, 4-11 MHz linear probe) was used to scan the phantom with the following settings: MI = 0.1, Gain = 70, Dynamic Range = 80, TGC = manually adjusted,

Frequency = 4/8 MHz. Two groups of ROIs (bubble regions within the lower vessel and tissue regions below that vessel) were selected on both the attenuated and control sides of the phantom (Figure 3-4) and the average intensity was compared before and after attenuation correction. The locations of ROIs were indicated in Figure 3-4, including regions for attenuated bubble signals, unattenuated bubble signals, attenuated tissue signals and unattenuated tissue signals respectively.

3.2.5 Clinical application (vessel wall)

48 patients previously treated for head and neck cancer (HNC) with at least one risk factor for atherosclerosis were recruited from a cancer centre. The study was approved by the institutional research and ethics committee and each patient provided informed consent. CEUS image sequences were acquired on both sides of the neck with a clinical scanner (GE Vivid7 with a 9 MHz broadband linear array transducer). A GE scanner was used to scan the phantom with the following settings: MI = 0.21, Gain = 0, Dynamic Range = 54, TGC = manually adjusted, Frequency = 3.2/6.4 MHz. Contrast-enhanced ultrasound video loops were taken using a commercially available ultrasound contrast agent, SonoVue^{TM} (Bracco, Milan) given as an intravenous infusion via a peripheral vein at a rate of 1.2 mL/min. The infusion was delivered over a total of 5-7 minutes. Imaging was performed in real-time prior to the arrival of and following the saturation of the carotid artery with SonoVue.

The FWHM of lumen intensity histogram for both uncorrected and corrected images was calculated. Our technique was then applied to investigate the hypothesis that radiation-induced injury results in an inflammatory response in the endothelium and consequent proliferation of adventitial vasa vasorum, which may be measured quantitatively using

CEUS. The mean contrast intensity (before and after attenuation correction) in the irradiated adventitia versus the mean contrast intensity in the unirradiated adventitia was compared. The effect of interval from radiotherapy (RT) on contrast intensity was investigated using linear regression. Correlation of contrast intensity to carotid intima-medial thickness (CIMT) and QSTROKE score was undertaken using Spearman's rank correlation. The QSTROKE score was specifically designed to aid general practitioners in predicting a patient's risk of developing a stroke and is based on the presence of atherosclerotic risk factors. The QSTROKE (2014) score was calculated for each patient using an online calculator (www.qstroke.org).

3.2.6 Statistical Analysis

The FWHM of lumen intensity histograms across the patient population are presented as means and standard deviations (SD). The FWHM of lumen intensity histograms were compared between uncorrected and corrected images using paired samples *t* tests. A two-tailed test was used, with alpha set at 0.05. Statistical analyses were performed using online GraphPad Prism 6.

3.3 Results

3.3.1 Phantom validation

Images of the phantom before and after correction are shown in Figure 3-4. The image intensity in the lumen on the LHS is significantly attenuated before correction and is restored to a level similar to that on the RHS after correction. The attenuated tissue region under the vessel on the LHS has also been compensated. Note that the difference in speed of sound

between the additional attenuation material and water caused image distortion for the vessel and phantom below.

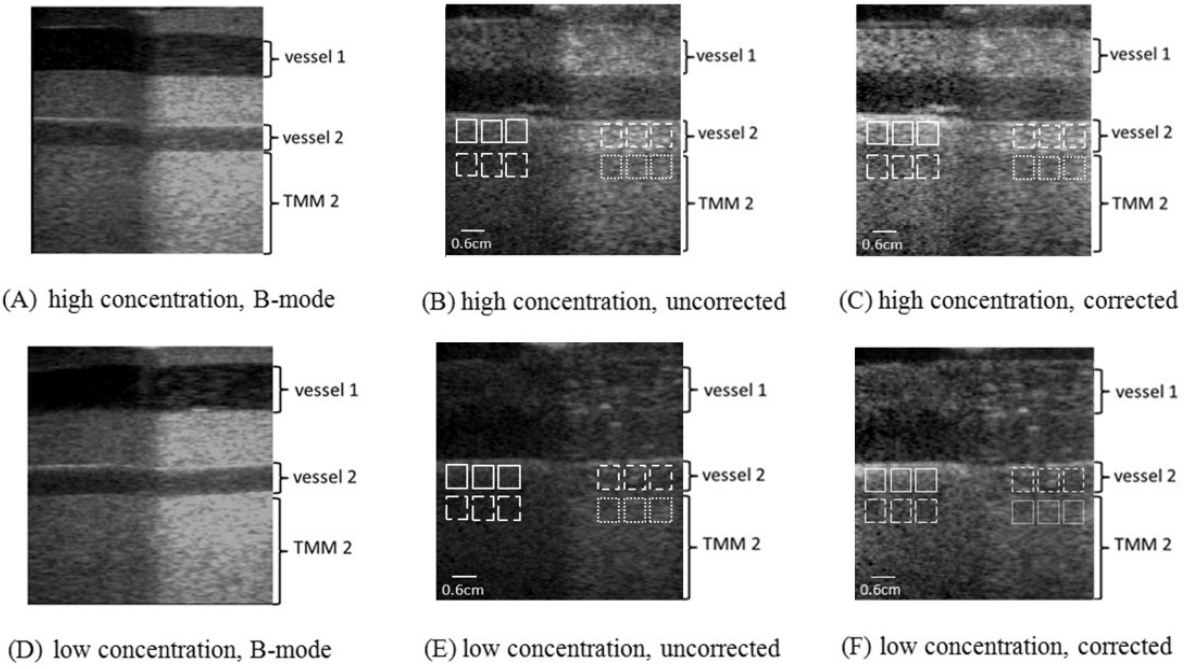

Figure 3-4: CEUS images of a carotid artery-mimicking phantom before and after attenuation correction with B-mode images as reference. ROIs with solid outlines for regions of attenuated bubble signals (bubble-attenuated), ROIs with dashed outlines for regions of unattenuated bubble signals (bubble-control), ROIs with long dashed lines for regions of attenuated tissue signals (tissue-attenuated) and ROIs with round dotted lines for regions of unattenuated tissue signals (tissue-control)

Table 3-1 and Table 3-2 show the ROI measurements of the phantom with high bubble concentration before and after attenuation correction. It can be seen that the intensity error was reduced from 61% to 7% for bubbles and from 58% to 13% for tissues after correction.

Table 3-1: Bubble ROIs measurement of phantom before and after attenuation correction (high concentration)

	ROI (bubble — control)	**ROI (bubble — attenuated) uncorrected**	**ROI (bubble — attenuated) corrected**
Intensity (Mean±SD)	1.11±0.053	0.439±0.058	1.03±0.029
Difference to control		61%±9%	7%±9%

Table 3-2: Tissue ROIs measurement of phantom before and after attenuation correction (high concentration)

	ROI (tissue — control)	**ROI (tissue — attenuated) uncorrected**	**ROI (tissue — attenuated) corrected**
Intensity (Mean±SD)	0.670±0.018	0.283±0.017	0.600±0.033
Difference to control		58%±2%	13%±4%

Table 3-3 and Table 3-4 show the ROI measurements of the phantom with low bubble concentration before and after attenuation correction. It can be seen that the intensity error was reduced from 47% to 17% for bubbles and from 60% to 14% for tissues after correction.

Table 3-3: Bubble ROIs measurement of phantom before and after attenuation correction (low concentration)

	ROI (bubble — control)	**ROI (bubble — attenuated) uncorrected**	**ROI (bubble — attenuated) corrected**
Intensity (Mean±SD)	0.819±0.103	0.429±0.026	0.838±0.047
Difference to control		47%±3%	17%±9%

Table 3-4: Tissue ROIs measurement of phantom before and after attenuation correction (low concentration)

	ROI (tissue — control)	**ROI (tissue — attenuated) uncorrected**	**ROI (tissue — attenuated) corrected**
Intensity (Mean±SD)	0.683±0.008	0.275±0.012	0.538±0.044
Difference to control		60%±1%	14%±9%

3.3.2 In vivo results

Patient characteristics were presented in Table 3-5. CEUS images of carotid arteries before and after attenuation correction are shown in Figure 3-5. It can be seen that in both cases part of the lumen is darker than the rest before the correction, and such attenuation artefacts are corrected for after applying the developed algorithms. Visually, the shadowing in the image

was removed. In addition, the visualization of contrast enhancement in the vessel wall was improved.

Table 3-5: Patient demographics

Demographic characteristics/risk factors		**Number (%) (N=48)**
Female		15 (31%)
Age in years, median (interquartile range)		59.2 (49.2 – 64.2)
Histology	Squamous	38 (79%)
	Non-squamous	10 (21%)
Tumour Grade	Well Differentiated	2 (4%)
	Moderate Differentiated	8 (17%)
	Poorly Differentiated	25 (52%)
	Unknown	13 (27%)
Tumour Stage	0	7 (15%)
	1	20 (42%)
	2	17 (35%)
	3	1 (2%)
	4	3 (6%)
Nodal Status	0	11 (23%)
	1	10 (21%)
	2	27 (56%)
Neck Dissection		31 (65%)
Induction Chemotherapy		7 (15%)
Concomitant Chemotherapy		22 (46%)

RT dose to neck (Gy)	50 Gray	19 (40%)
	60 Gray	28 (58%)
	63 Gray	1 (2%)
Interval since radiotherapy (months)		59.4 (41- 88.7)
Risk Factors	Diabetes	4 (8%)
	Hypertension	12 (28%)
	Dyslipidaemia	11 (23%)
	Smoker	25 (52%)
Body Mass Index (kg/m^2) **(median (IQR))**		26.5 (23.2 – 28.4)
Medication	Aspirin	12 (28%)
	ACE Inhibitors	4 (8%)
	5-HMG Co-reductase Inhibitor	13 (27%)
Total Cholesterol **(mmol/L)**		5.1 (4.6 - 5.8)
Low Density Lipoproteins **(mmol/L)**		3.3 (2.6 - 3.7)
High Density Lipoproteins **(mmol/L)**		1.4 (1.2 – 1.7)

3.3.3 Histogram of lumen intensity and FWHM evaluation

Lumen intensity histograms for the two patients are shown in Figure 3-6. FWHM of the intensity histogram within the lumen was reduced from 0.350 (Figure 3-6A) to 0.195 (Figure 3-6B) after attenuation correction for patient A and from 0.500 (Figure 3-6C) to 0.150 (Figure 3-6D) for patient B.

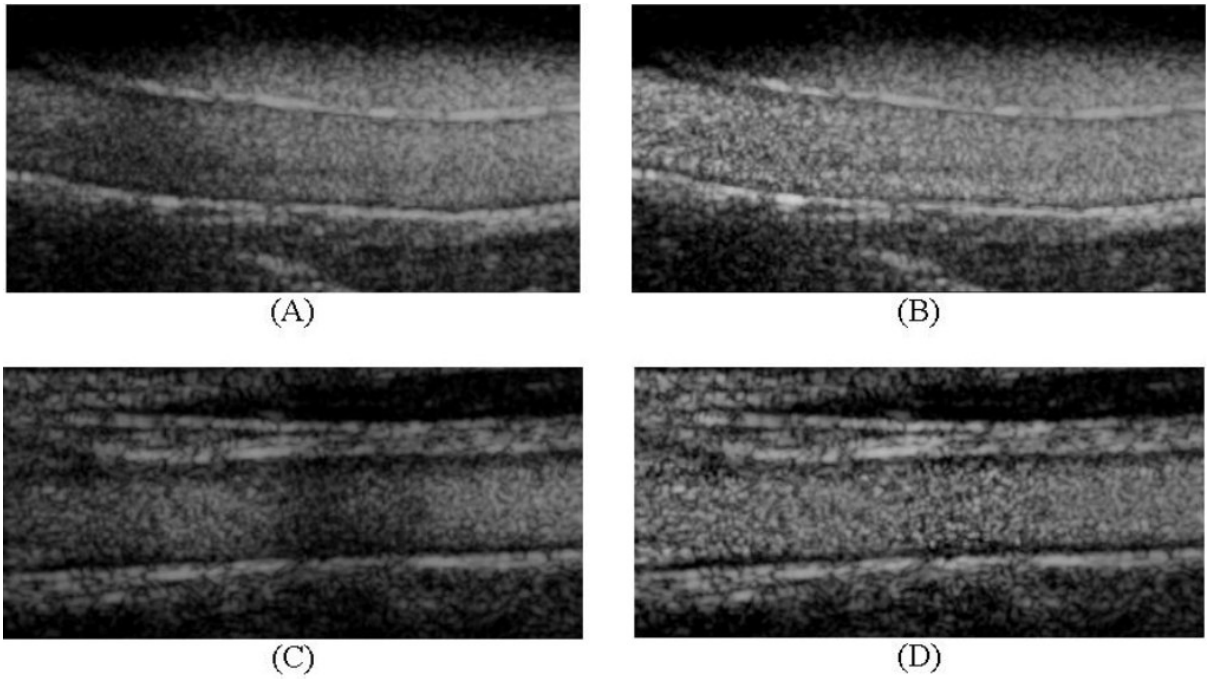

Figure 3-5: Examples of CEUS images of carotid arteries before and after attenuation correction. Top row: Patient A before (A) and after (B) attenuation correction; Bottom row: Patient B, before (C) and after (D) attenuation correction

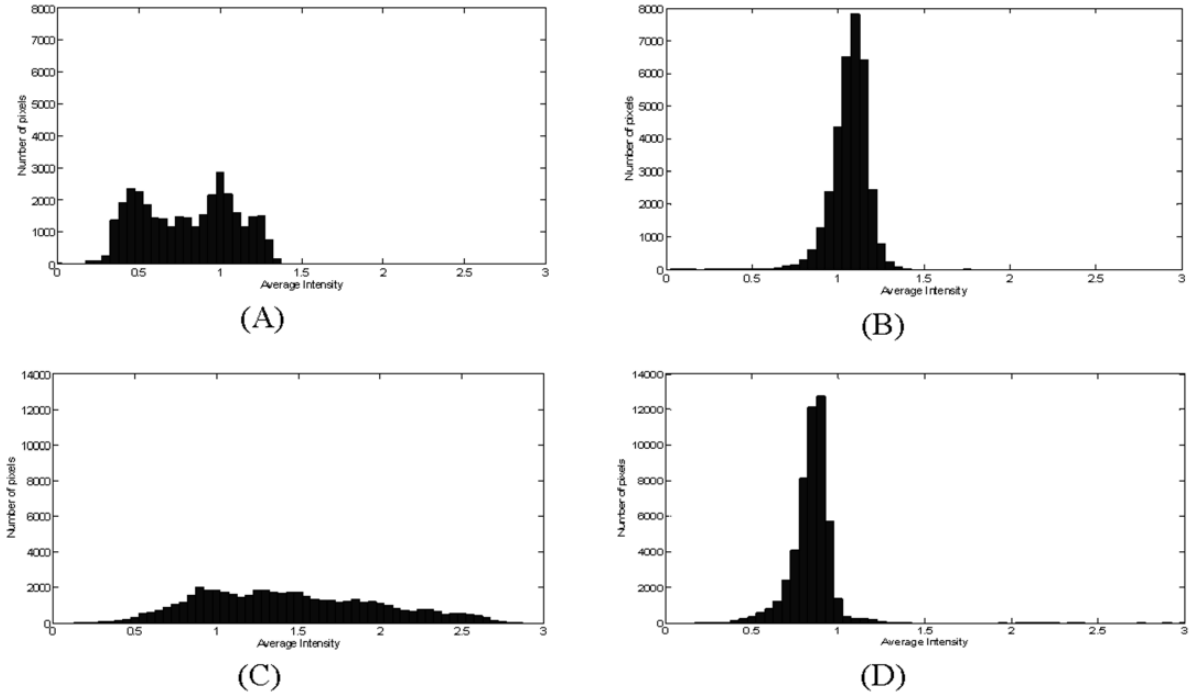

Figure 3-6: Image intensity within lumen before and after attenuation correction. Top row: Patient A before (A) and after (B) attenuation correction; Bottom row: Patient B before (C) and after (D) attenuation correction

The FWHMs of lumen intensity histogram for all 48 patients were compared before and after attenuation correction. The mean ± SD of the FWHM was 0.346 ± 0.138 before and 0.135 ± 0.038 after the correction, representing a 61.0% decrease in FWHM with the corrected image compared with the uncorrected one. This decrease in FWHM is statistically significant (paired *t* test; $p < 0.0001$).

3.3.4 Contrast intensity evaluation in advential vasa vasorum

There was a significant difference in the mean (SD) contrast intensity per pixel on the irradiated side (1.1 (0.4)) compared to 0.96 (0.34) on the unirradiated side (paired *t* test; $p = 0.01$). After attenuation correction, the difference in mean contrast intensity per pixel was

still significant (1.4 (0.58) versus 1.2 (0.47) (paired *t* test; $p = 0.02$)) (Figure 3-7A and 3-7B). We compared the contrast intensity before contrast (subtraction images) between the irradiated and unirradiated side. There was no difference between the signal intensity before contrast infusion in irradiated (mean 0.55 (SD = 0.18)) versus unirradiated (mean 0.51 (SD = 0.18) (paired *t* test; $p = 0.12$) arteries, suggesting that there was no significant difference in tissue homogeneity between irradiated and unirradiated arteries before contrast infusion.

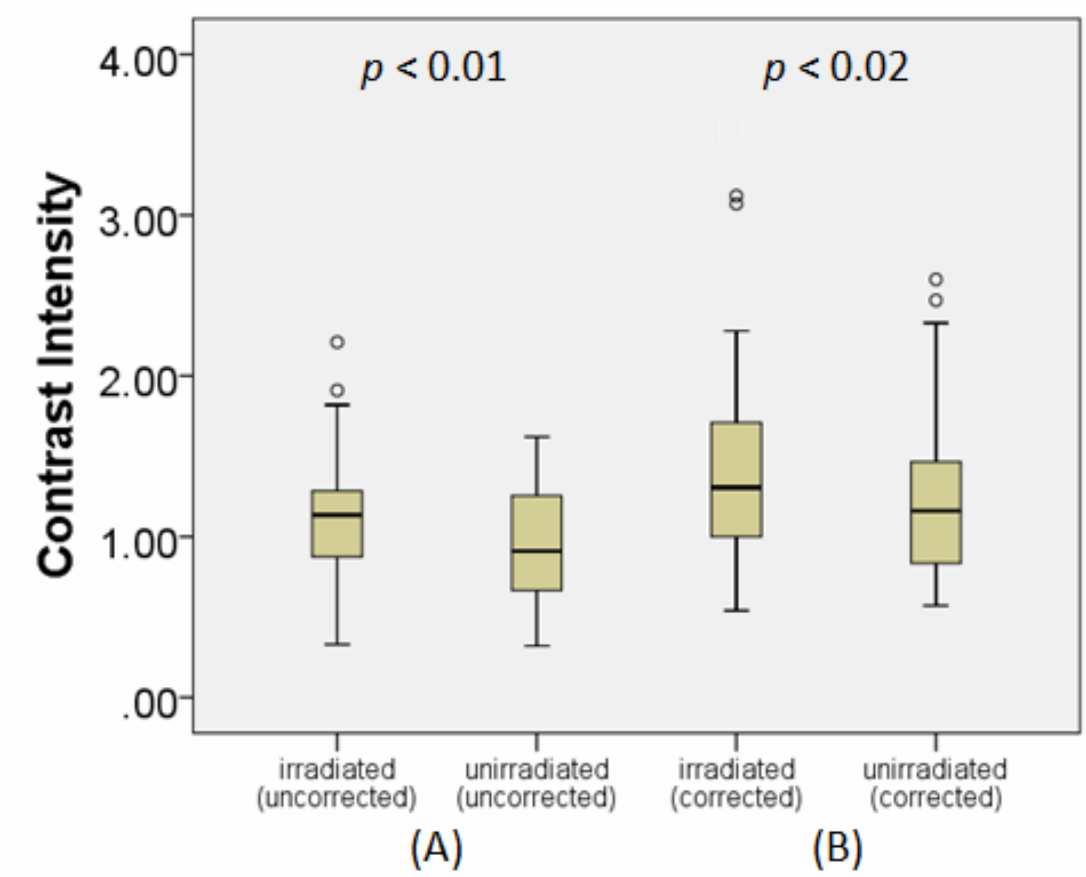

Figure 3-7: Contrast adventitial intensity in irradiated versus unirradiated arteries (A) before attenuation correction and (B) after attenuation correction (*p* significant if <0.05).

3.3.5 Correlation of contrast intensity to CIMT

As ROIs were selected on the far wall of the distal CCA, we compared the difference in mean distal CCA CIMT between irradiated – unirradiated arteries to the difference in contrast

intensity between irradiated – unirradiated arteries (Figure 3-8). There was no significant correlation between CIMT and contrast intensity either before or after attenuation correction.

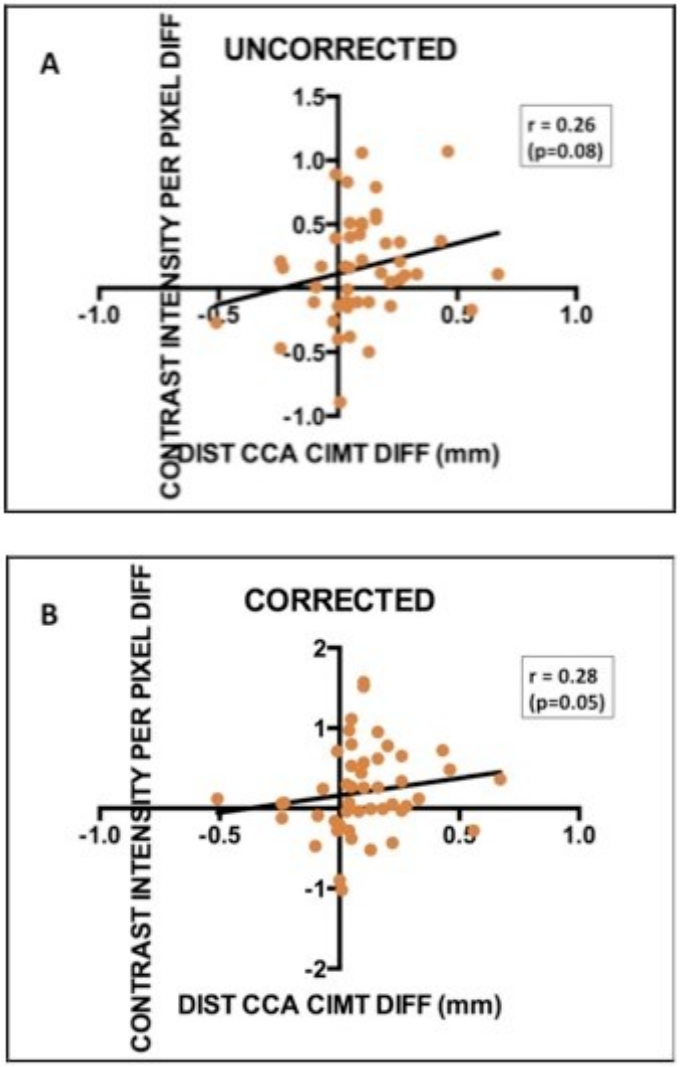

Figure 3-8: Correlation of distal CCA CIMT difference (irradiated – unirradiated) and contrast intensity difference (irradiated – unirradiated) (A) before and (B) after attenuation correction (*p* significant if <0.005)

3.3.6 Correlation of contrast intensity to QSTROKE score

There was no correlation between contrast intensity and QSTROKE score for both the irradiated and unirradiated side of the neck (Table 3-6).

Table 3-6: Correlation of contrast intensity to QSTROKE score for irradiated and unirradiated arteries (p significant if <0.005)

Correlation coefficient (r)			P value
Irradiated	**Contrast intensity**	-0.06	0.68
	Corrected contrast intensity	0.07	0.64
Unirradiated	**Contrast intensity**	-0.15	0.31
	Corrected contrast intensity	0.002	0.99

3.3.7 Correlation of contrast intensity to interval from RT

The correlation of adventitial contrast intensity difference (irradiated – unirradiated) to interval from RT is shown in Figure 3-9 (attenuation-corrected images). This shows no correlation between the interval from RT and the difference in contrast intensity between the two sides of the neck. This suggests that contrast intensity does not increase steadily over time. Rather, it is more likely that this increase following RT occurs at a certain time point and then remains stable over time. As all patients had been treated at least 2 years previously, it is probable that this process occurs prior to 2 years following RT.

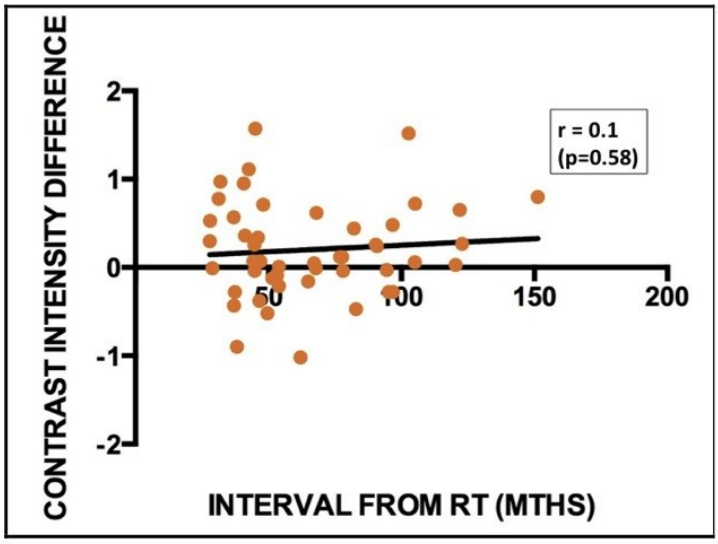

Figure 3-9: Correlation of contrast intensity difference (irradiated – unirradiated) and interval from RT (*p* significant if <0.005)

3.4 Discussion

An attenuation correction and image normalisation method for CEUS carotid artery images has been developed for more reliable quantification of contrast enhancement. The method uses the lumen as a reference, where the image brightness is assumed to be homogeneous if attenuation is properly corrected. Our initial results on phantoms and in vivo carotid arteries show that the correction method significantly reduces attenuation artefact. On phantom evaluation the errors due to attenuation is reduced from 47-61% to 7-17%. For in vivo data the correction improved the lumen homogeneity, measured as FWHM of the lumen intensity histogram, by 61% in average.

The method assumes that microbubbles are well mixed across the lumen, and, therefore, that image brightness should be homogeneous if attenuation is properly corrected. This is a

reasonable assumption as the microbubbles are injected as an intravenous infusion and by the time they get to the carotid artery they would have been well mixed in blood.

The correction algorithm includes two parameters: the Gaussian spatial low-pass filter size and the regulariser. They are independent of each other. The filter size (sigma) is determined by the size of the speckles (it needs to be big enough to remove the speckles), while the regularizer is determined by the system noise level.

There are a range of imaging variables including ultrasound scanner settings such as frequency, MI, various gain settings and dynamic range and the type of scan format (linear or sector). The proposed algorithms are not expected to be significantly affected by the variations of most of these factors in general as they do not violate the model assumption, i.e. microbubbles within vessel lumen are well mixed and hence vessel lumen signals should be homogeneous. However, some factors, such as dynamic range, if set to too low, could cause image saturation and hence impact the results.

To illustrate the effect of attenuation in both axial and lateral directions, we have performed correction in x direction alone by averaging the estimated attenuation vertically, and compared with the correction in both directions. From Figure 3-10D, it can be seen that the attenuation in both direction is significant and should be corrected.

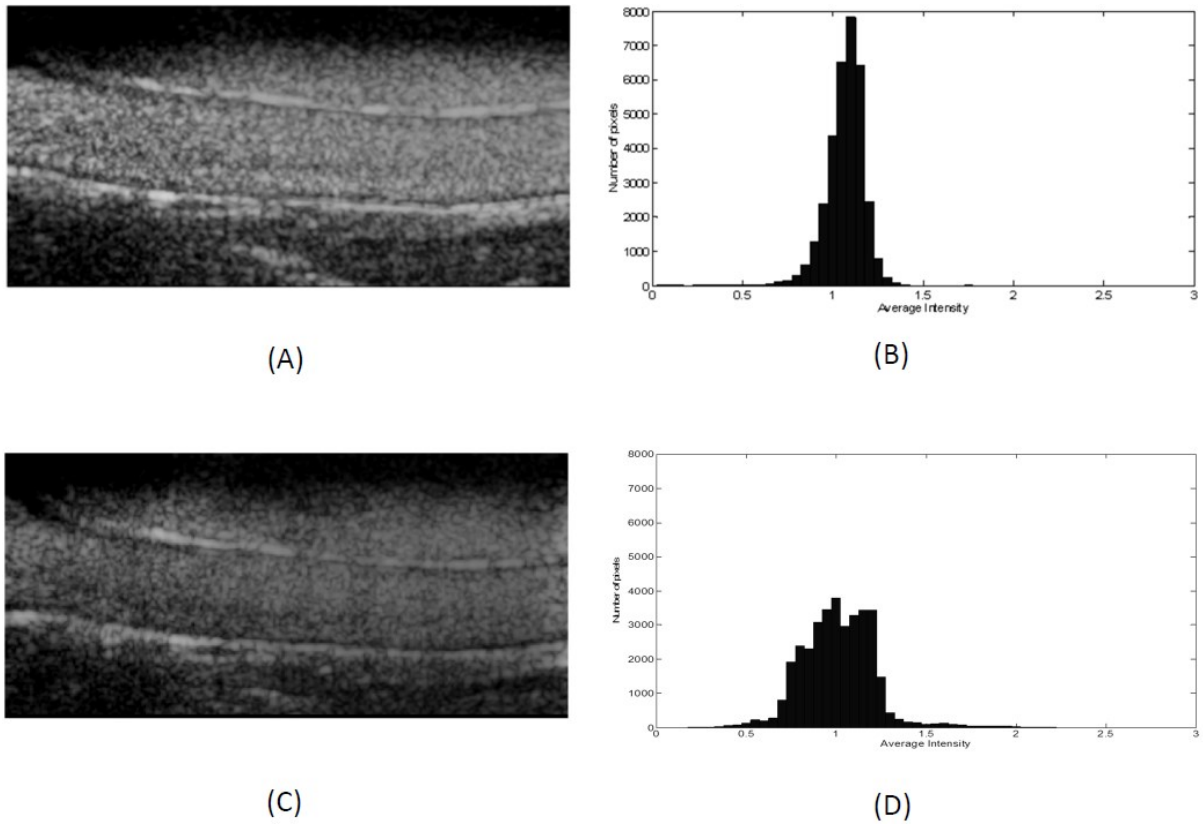

Figure 3-10: Top row: Attenuation correction in both x and y direction (A) CEUS image and (B) Image intensity histogram within lumen after attenuation correction. Bottom row: Attenuation correction in x direction only (C) CEUS image and (D) Image intensity histogram within lumen after attenuation correction

Besides attenuation, nonlinear imaging artefacts (15, 16) also commonly exist in CEUS images. Such artefacts originate from the assumption of totally linear ultrasound transmission and propagation on one hand and the nonlinear propagation of the transmitted ultrasound pulse through tissue and/or microbubble clouds in reality on the other hand (15, 16). These artefacts vary with both ultrasound amplitude and frequency. Clinical examples of such artefacts have been recently reported (17, 18). In the present study, the quantification results are likely to contain, besides desirable neovascularisation and VV signals, significant undesirable nonlinear artefacts. It is important to address both attenuation and the nonlinear

artefacts in order to achieve reliable quantification in CEUS images. We are currently working on correction of nonlinear artefacts and initial results have already been reported (19) with the aim of incorporating this into our software. Currently, further use of our software in a clinical setting would be suitable to quantifying differences in contrast intensity between patients and controls, where there is a reasonable expectation that nonlinear imaging artefacts would be similar for both groups.

Attenuation artefacts in CEUS images, together with other factors, have made reliable quantification difficult and lead to diagnostic uncertainty. This is the first study, as far as we are aware, to develop attenuation and normalisation techniques for CEUS carotid images. It does not require modification to any imaging system hardware and can be packaged as a software module and integrated into existing commercial ultrasound scanners. While in this work the correction of attenuation and normalisation were conducted offline, real-time processing is feasible as the algorithm only involves simple filtering and division. Currently the more time-consuming part is the manual lumen segmentation and motion tracking but given that the algorithm does not depend on accurate lumen segmentation and tracking, it is feasible for these to be done in real-time. This technique has potential to be extended to other views of carotid arteries and this requires further studies. The in-vivo study has demonstrated a significant difference in contrast intensity between irradiated and unirradiated carotid arteries with novel software that utilizes an attenuation correction and image normalization method. This is strengthened by the fact that no significant difference was seen between the two sides of the neck on subtraction images (i.e. before the infusion of contrast). Furthermore, the use of controls would be valuable in determining changes related specifically to signal intensity due to neovascularisation, both in the adventitia and in plaques.

The intensity per pixel parameter derived in this study has not been utilized before and requires validation in a longitudinal study and correlation to histological samples. We believe, however, that the average intensity per pixel will be more representative of changes occurring in the adventitia and less likely to over- or underestimate contrast intensity in the adventitia.

In CEUS, pseudo-enhancement artefact originating from tissues could be present due to ultrasound non-linear propagation (15, 16). To rule out the possibility that different tissue echogenicity caused the difference in CEUS signals in our study, non-contrast video loops of arteries on both sides of the neck were obtained prior to contrast infusion. There was no significant difference in adventitial intensity between the two sides of the neck prior to contrast and, therefore, we are confident that differences in intensity between the two sides following contrast infusion were likely to have been due to the contrast uptake in the adventitial vasa vasorum.

There was no correlation between the contrast intensity difference and the difference in the distal CCA CIMT or the QSTROKE score. Therefore, further prospective work is required to determine if this imaging biomarker is truly an early marker of radiation-induced atherosclerosis. Prospective data using this model of matched internal controls would provide useful information about the timing of adventitial vasa vasorum proliferation after RT and its correlation to CIMT at different time points. It is also possible that this marker is

an independent biomarker and may correlate to the final end-point of stroke or TIA but long-term data are required to clarify this.

3.5 Conclusions

Our attenuation correction and normalisation method shows a significant reduction of attenuation artefacts both on a carotid artery-mimicking phantom and in vivo. This will be a step towards reliable quantification of contrast enhancement in CEUS carotid images.

References

1. Murray CJ, Lopez AD**.** Mortality by cause for eight regions of the world: Global Burden of Disease Study. Lancet. 1997;349(9061):1269-76.
2. U-King-Im JM, Young V, Gillard JH**.** Carotid-artery imaging in the diagnosis and management of patients at risk of stroke. Lancet Neurology. 2009;8(6):569-80.
3. Topol EJ, Nissen SE**.** Our Preoccupation with Coronary Luminology - the Dissociation between Clinical and Angiographic Findings in Ischemic-Heart-Disease. Circulation. 1995;92(8):2333-42.
4. Virmani R, Burke AP, Farb A, Kolodgie FD**.** Pathology of the vulnerable plaque. Journal of the American College of Cardiology. 2006;47(8):C13-C8.
5. Hellings WE, Peeters W, Moll FL, et al. Composition of Carotid Atherosclerotic Plaque Is Associated With Cardiovascular Outcome A Prognostic Study. Circulation. 2010;121(17):1941-U111.
6. Macioch JE, Katsamakis CD, Robin J, et al. Effect of contrast enhancement on measurement of carotid artery intimal medial thickness. Vascular Medicine. 2004;9(1):7-12.

7. Feinstein SB**.** Contrast ultrasound imaging of the carotid artery vasa vasorum and atherosclerotic plaque neovascularization. Journal of the American College of Cardiology. 2006;48(2):236-43.

8. Tang MX, Mulvana H, Gauthier T, et al. Quantitative contrast-enhanced ultrasound imaging: a review of sources of variability. Interface Focus. 2011;1(4):520-39.

9. Tang MX, Mari JM, Wells PNT, Eckersley RJ**.** Attenuation Correction in Ultrasound Contrast Agent Imaging: Elementary Theory and Preliminary Experimental Evaluation. Ultrasound in Medicine and Biology. 2008;34(12):1998-2008.

10. Mule S, De Cesare A, Lucidarme O, et al. Regularized estimation of contrast agent attenuation to improve the imaging of microbubbles in small animal studies. Ultrasound in Medicine and Biology. 2008;34(6):938-48.

11. Mari JM, Hibbs K, Stride E, et al. An Approximate Nonlinear Model for Time Gain Compensation of Amplitude Modulated Images of Ultrasound Contrast Agent Perfusion. Ieee Transactions on Ultrasonics Ferroelectrics and Frequency Control. 2010;57(4):818-29.

12. Briechle K, Hanebeck UD**.** Template matching using fast normalized cross correlation. Optical Pattern Recognition Xii. 2001;4387:95-102.

13. Golemati S, Sassano A, Lever MJ, et al. Carotid artery wall motion estimated from B-mode ultrasound using region tracking and block matching. Ultrasound in Medicine and Biology. 2003;29(3):387-99.

14. Madsen EL, Frank GR, Dong F**.** Liquid or solid ultrasonically tissue-mimicking materials with very low scatter. Ultrasound in Medicine and Biology. 1998;24(4):535-42.

15. Tang MX, Eckersley RJ**.** Nonlinear propagation of ultrasound through microbubble contrast agents and implications for Imaging. Ieee Transactions on Ultrasonics Ferroelectrics and Frequency Control. 2006;53(12):2406-15.

16. Tang MX, Kamiyama N, Eckersley RJ**.** Effects of Nonlinear Propagation in Ultrasound Contrast Agent Imaging. Ultrasound in Medicine and Biology. 2010;36(3):459-66.

17. ten Kate GL, Renaud GGJ, Akkus Z, et al. Far-Wall Pseudoenhancement during Contrast-Enhanced Ultrasound of the Carotid Arteries: Clinical Description and in Vitro Reproduction. Ultrasound in Medicine and Biology. 2012;38(4):593-600.

18. van den Oord SC, Renaud G, Bosch JG, et al. Far wall pseudo-enhancement: a neglected artifact in carotid contrast-enhanced ultrasound? Atherosclerosis. 2013;229(2):451-2.

19. Yildiz YO, Eckersley RJ, Tang MX**.** Correction of nonlinear imaging artefacts in contrast enhanced ultrasound. Proceedings of the 19th European symposium on Ultrasound Contrast Imaging. 2014.

Chapter 4

A temporal and spatial analysis approach for automated segmentation of microbubble signals in contrast enhanced ultrasound images – application to quantification of active vascular density in human lower limbs

Contrast enhanced ultrasound (CEUS) using microbubble contrast agents has shown great promise in visualising and quantifying active vascular density. Most existing approaches for perfusion quantification using CEUS are calculated based on image-intensity, and are susceptible to confounding factors and imaging artefact. Poor reproducibility is a key challenge to clinical translation. In this study a new automated temporal and spatial signal analysis approach is developed for reproducible microbubble segmentation and quantification of contrast enhancement in human lower limbs. The approach is evaluated *in vitro* on phantoms and *in vivo* in lower limbs of healthy volunteers before and after physical exercise. In this approach perfusion is quantified based on the relative areas microbubbles occupy instead of their image intensity. Temporal features of the CEUS image sequences are used to identify pixels that contain microbubble signals. A microbubble track density (MTD) measure, the ratio of the segmented microbubble area over the whole tissue area, is calculated as a surrogate for active capillary density. In vitro results show a good correlation (r^2 = 0.89) between the calculated MTD measure and the known bubble concentration. For in vivo

results, a significant increase (129% in average) in the MTD measure is found in lower limbs of healthy volunteers after exercise, with excellent repeatability over a series of days (ICC = 0.96). This compares to the existing state-of-art approach of destruction and replenishment analysis on the same subjects (ICC <= 0.78). The proposed new approach demonstrates great potential as an accurate and highly reproducible clinical tool for quantification of active vascular density. This work was in collaboration with Dr Katherine J. Williams and Dr Brahman Dharmarajah from Section of Surgery, Imperial College, Charing Cross Hospital, where they focused on evaluation of musculoskeletal microcirculation with contrast enhanced ultrasound.

4.1 Introduction

Ultrasound is a safe, affordable and accessible front-line clinical imaging modality, characterised by real-time image display. Recent advances in contrast-enhanced ultrasound (CEUS) imaging, provide the possibility of specifically imaging blood vessels with high sensitivity and resolution. Microbubbles move through the body while being confined to blood vessels, distinguishing them as an excellent intravascular contrast medium. They vibrate under ultrasound and in a non-linear fashion, generating specific harmonic signatures that allow them to be distinguished from background tissue signals with a high sensitivity.

CEUS is ideally suited for measurements of flow and perfusion, as bubbles move within the blood vessels at comparative speeds to blood cells. A destruction-replenishment approach has been used in many in vitro and in vivo trials with success. High amplitude ultrasound is used to destroy microbubbles within the imaging plane, then the replenishment of the region is observed over time. To quantify perfusion, Time Intensity Curve (TIC) analysis is conducted to extract a number of physiological parameters such as peak intensity, time to peak and flow

rate etc. This method estimates parameters related to vascular characteristics of the tissue and has been applied to the study of liver (1) and heart (2, 3). Recent studies have shown particularly great promise in evaluating neovascularisation in atherosclerotic plaques (4-6), the myocardial microcirculation (2, 3) and the musculoskeletal microcirculation of the lower limb (7-14).

However the quantification of perfusion using CEUS is affected by many confounding factors (15). In particular most existing analysis is image-intensity based, and such an approach is vulnerable to problems such as signal attenuation, and nonlinear imaging artefacts (16, 17). An alternative approach to individual bubble tracking and quantification within the image have been reported, particularly in peripheral imaging applications where relatively high frequencies are commonly used (4-15MHz). While imaging with such frequencies reduce sensitivity in bubble detection (18) and only the brightest bubbles show up in the CEUS images, the improved spatial resolution associated with such high frequency could facilitate the tracking of individual bubbles. Hoogi et al. (19) proposed a method for segmenting the contrast spots within atherosclerotic plaques in individual images by tracking individual microbubbles. The main advantage of this approach is that the temporal behaviour of bubble flow can be demonstrated. This makes it robust to noise and allows differentiation between blood vessels and artefacts.

In CEUS image sequences, we hypothesise that the temporal profile of each pixel can be used to detect microbubbles passing the pixel. The relative area of these “bubble pixels” can provide an area-based perfusion measure that may be more robust than existing image-intensity based approaches. Furthermore, the pixel-based temporal analysis can be reduced to

an automated algorithmic process, giving advantages in terms of user interface, output speed and interpretation over existing approaches.

The objective of this study was to develop a robust and automated quantification tool for microbubble identification in CEUS image sequences using a pixel level temporal and spatial analysis based algorithm. This technique will be demonstrated with a flow phantom and then, as an initial clinical demonstration, applied to the quantification of in vivo musculoskeletal microcirculation in lower limb perfusion of healthy human subjects.

4.2 Materials and Methods

4.2.1 Microbubble detection algorithm

The proposed algorithm works at a pixel level to detect microbubble signals. The image contains primarily three components: tissue artefact, noise, and microbubble signals. Initially, average image intensity and coefficient of variation are used to remove tissue signals, and then microbubbles are distinguished from noise by examining the frequency composition of the pixel's temporal signal. The temporal signal of a pixel within a vessel with bubble(s) passing through has very different frequency composition from that with noise only (See Figure 4-2). The microbubble detection algorithm consists of the following specific steps.

1) Detecting tissue only regions.

   Given the signal, *I(t)*, the coefficient of variation (COV) is shown as follow,

$$COV = \frac{\sqrt{(I - \langle I(t)\rangle)^2}}{\langle I(t)\rangle} \tag{4-1}$$

where $\langle I(t) \rangle$ is the temporal average intensity. If we assume tissue signals to be higher in amplitude than noise background and not changing significantly over time, the combination of COV and average intensity can be used to identify tissue signal. If a signal's COV is smaller than a threshold T_{COV} and its average intensity is larger than a threshold T_{AI}, this signal is classified as tissue signal. The threshold values of T_{COV} and T_{AI} are estimated empirically by examining the histograms of the datasets. The remaining unclassified signals contain microbubbles and noise.

Figure 4-1A and 4-1B show screen captures from a human subject's gastrocnemius after an intravenous injection of Sonovue. It can be seen that microbubble signals, tissue signals (arrows in Figure 4-1A) and noise are visible in the image.

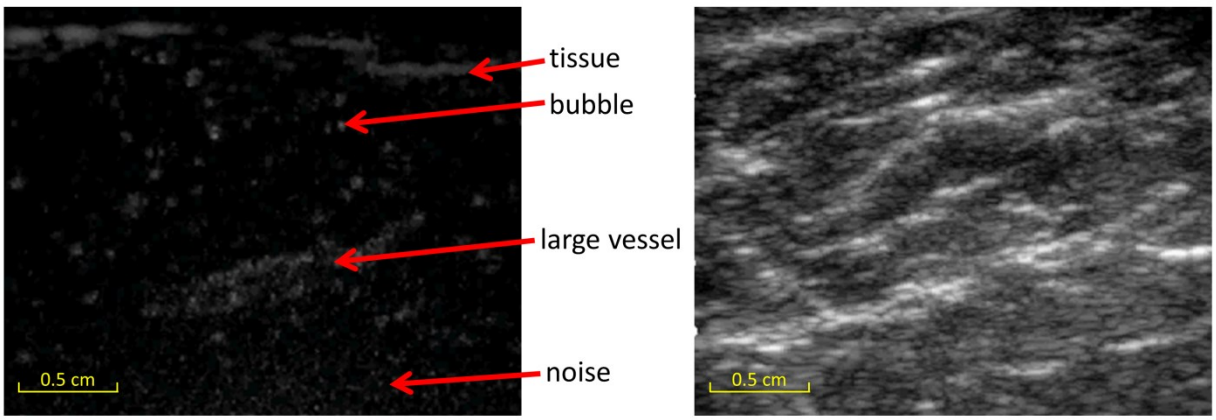

Figure 4-1: Contrast-enhanced ultrasound screen captures from human gastrocnemius muscle in vivo, after injection of Sonovue. (A) CEUS mode image with tissue and microbubble signals are labelled with arrows. and (B) B-mode image

2) Separating microbubble regions from regions of noise through examining temporal features

It is assumed that the temporal noise of the ultrasound data is white noise and hence broadband. For a pixel where a microbubble(s) passed through, the temporal signals are expected to have more low frequency components depending on the velocity of the microbubbles. Therefore a simple way to identify microbubble signal from noise is to look at the frequency features of the signals.

Example time intensity curves (Figures 4-2A and 4-2C) and their spectrum (Figures 4-2B and 4-2D) for microbubbles and noise from single pixels of in vivo human data are shown. It can be seen that the microbubble signal consists of more low frequency components, while the noise is spread over the whole spectrum, thus allowing their separation. In this study, we fix the time window for Fourier analysis to be 30 seconds. This is empirically chosen in order to generate reasonable amount of segmented bubble signal within the image plane.

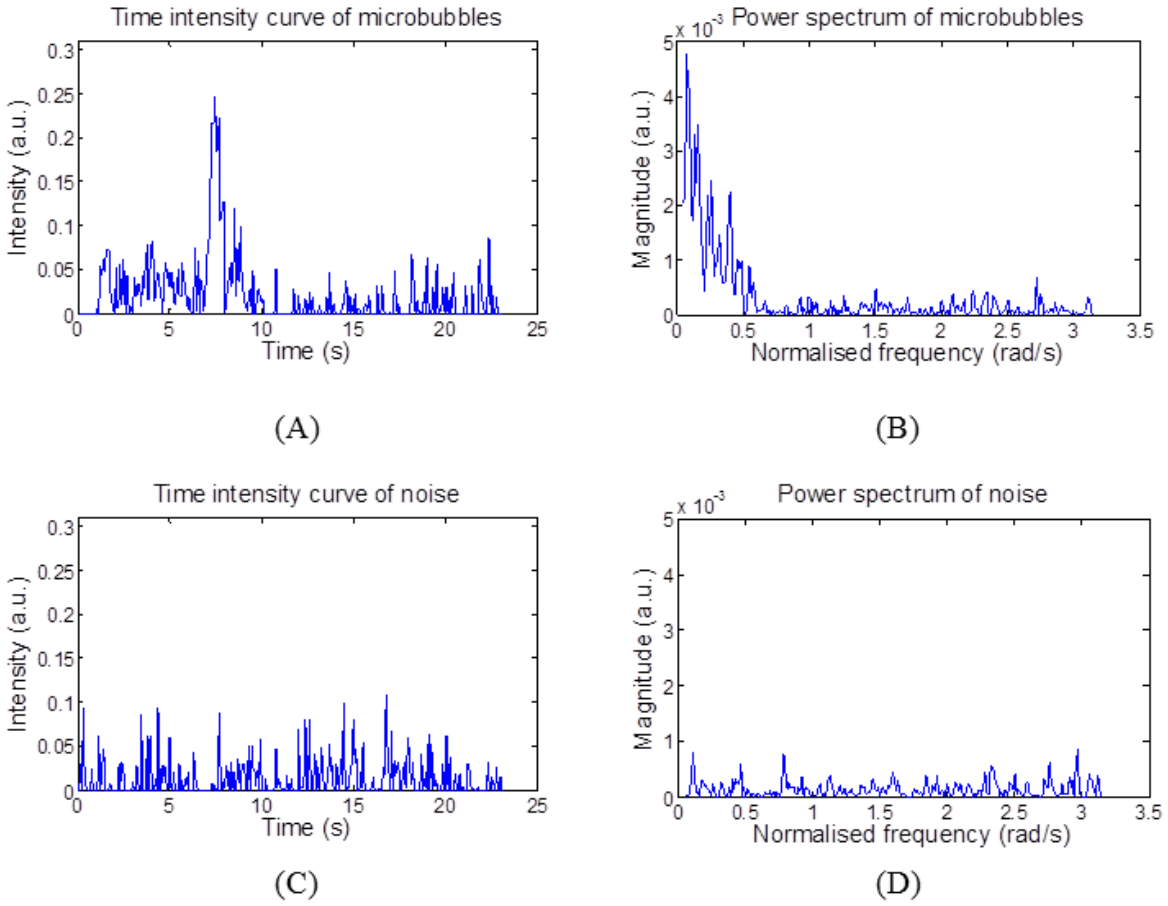

Figure 4-2: The time intensity curve and power spectrum of (A, B) microbubbles (C, D) noise

The power spectrum density in Figure 4-2B and 4-2D represents the frequency composition of the pixel temporal signal (Figure 4-2A and 4-2C). Such frequency spectrum indicates how fast the pixel signal changes over time. For a pixel containing only noise, the signal changes has both fast (high frequency) and slow (low frequency) components in the spectrum (broadband) (Figure 4-2D). For bubble signal the change is slow and it has a peak at lower frequencies in the spectrum (Figure 4-2B). The position of the peak depends on the bubble flow velocity as explained in the Methods section and equation (4-2).

Before describing the following steps of the method, the physiological relevance of the frequency of the microbubble signal should be explained. The rate of change of the intensity at a point is related to flow velocity. Therefore, given a single microbubble with velocity

$v_b = \frac{d}{t}$, where the d is the distance travelled by it in time t either within or across the ultrasound imaging plane. For a certain concentration of microbubbles, if we assume that the microbubbles are well mixed and the average separation distance of two neighbouring microbubbles is D, while the duration between one bubble passing a certain pixel and its neighbour bubble passing the same pixel is T, the velocity of a single microbubble can be described by equation (4-2):

$$v_b = \frac{D}{T} = fD \tag{4-2}$$

where f is the inverse of T, i.e. a frequency. Assuming a constant concentration, the frequency is linearly related to the velocity of microbubbles.

While the frequency is determined by microbubble velocity, it is also affected by microbubble concentration and other factors. To improve the robustness of the method, instead of examining the fine features on the spectrum, a simple measure of relative weighting of the signals high and low frequency components is used in this study. Given the microbubble signal, $I_b(t)$, noise signal, $I_n(t)$, and their power spectrums $\widehat{I_b}(f)$, $\widehat{I_n}(f)$, a cut-off frequency, f', is defined (see equation (4-3)) to separate the spectrum into low and high frequency regions. The area under curve is then calculated (exclude the DC component) for these two regions correspondingly. A high-to-low frequency ratio (HLFR) is calculated:

$$HLFR = \frac{\sum_{f>f'} \left|\hat{I}(f)\right|}{\sum_{f\leq f'} \left|\hat{I}(f)\right|} \tag{4-3}$$

The ratio is used to classify a given signal as either microbubble or noise. For a pixel containing e.g a microvessel, as microbubbles occasionally pass this otherwise dark pixel, its

temporal signal is expected to have a higher proportion of lower frequency components than white noise. Consequently the HLFR of the pixel is expected to be smaller than that of noise.

A histogram of normalised HLFR for each CEUS image sequence is then constructed where two peaks are expected (See Figure 4-5), one corresponding to microbubbles and the other to noise background. A HLFR threshold, T_{HLFR}, is then determined to separate the microbubble and noise distribution. To automatically determine the threshold, the histogram is fitted using a double-Gaussian model. The threshold is set at the interception of these two Gaussian distributions.

The cut-off frequency f' in equation (4-3) to separate the high and low frequency components in the signal spectrum is important and needs to be optimised. f' is ranging from 0.31 to 3.14 with interval 0.31. We formulate an optimisation solution to estimate the optimal cut-off frequency, $\widehat{f'}$, by maximising the distance between the bubble peak and noise peak, $L(f')$, in the HLFR histogram,

$$\widehat{f'} = arg\,\max_{f'}(L(f')) \tag{4-4}$$

Once the optimal $\widehat{f'}$ is determined, the threshold T_{HLFR} can be computed accordingly to segment out bubble areas.

Finally a spatial filtering is conducted to the segmented image to remove isolated pixels of noise to further improve the robustness of the algorithm. A 3x3 pixel median filter is applied.

The size of the filter is determined when taking into account the spatial extent of a microbubble in an image.

4.2.2 Microbubble track density (MTD) measure

The number of pixels identified as having bubble signals is normalized by the total number of pixels within the ROI to obtain the microbubble track density (MTD) measure for the ROI.

$$MTD = \frac{\text{number of pixels with microbubbles}}{area\ of\ ROI} \tag{4-5}$$

This measure is used as a surrogate for active vascular density within the ROI.

4.2.3 Phantom flow model set up and validation

The microbubble detection algorithm was validated on a flow phantom constructed in-house. It consisted of a contrast agent-filled solution in a tank. The flow was generated by a magnetic stirrer, which is placed under the tank. Given that the microbubbles were well mixed, such a setup offers repeatable experimental measurements with different concentrations of microbubbles.

The SonoVue^{TM} (Bracco, Milan) microbubbles were used at six concentrations: 0 µL (control), 0.05µL, 0.1µL, 0.15µL, 0.2µL and 0.25µL, diluted in 0.6L air-saturated water in a tank. A magnetic stirrer was used to stir the solution at 2 rev/second. CEUS data were acquired using the following in vitro scanning protocol. A clinical ultrasound scanner (Philips iU22, linear 3/9MHz broadband linear array transducer) was used to scan the phantom with the following settings: gain = 69%, TGC = manually adjusted, frame rate = 13Hz,

compression = 50, persistence = off. The scanner MI was set at 0.06 and the contrast imaging mode on the Philips IU22 scanner was used. With the low MI, bubble destruction is largely avoided and better reduction of the harmonic component from the tissue is achieved. Three 10-second sequences were obtained for each volume of microbubbles. Analysis of CEUS video sequences was performed offline using software developed in-house (Matlab, The Mathworks Inc., Natick, MA, USA). Regions of interest (ROIs) in the middle of the image covering a rectangular area of 245 x 70 pixels were selected manually. The MTD quantities generated by the proposed method are compared with the known concentrations of the microbubbles.

4.2.4 In vivo methodology

Five healthy volunteers were recruited from a research centre (Charing Cross Hospital, Imperial College London). The study was approved by the National Research and Ethics Committee (reference 13/LO/0943) and each participant provided written informed consent. CEUS image sequences were acquired on the lower limb with a clinical scanner (PHILIPS iU22 with a 3/9 MHz broadband linear array transducer) with the same settings as *in vitro* experiments. Contrast imaging mode in Philips IU22 scanner is used in this study. All the analyses were performed on such contrast specific images. B mode image is only used for motion estimation. SonoVue^{TM} was diluted using normal saline via a mini-spike system (25mg in 20ml). It was given as a continuous intravenous infusion (VueJect^{TM}, Bracco, Milan) via an 18G cannula sited in an antecubital vein, at a rate of 4.0 mL/min. Subjects were positioned on an examination couch in the left-lateral position, with knees lightly flexed for comfort. Image sampling was taken perpendicular to the skin from the medial head of gastroctrocnemius in the left leg, and marked for repeated measures. Care was taken to standardise the relative positions of both subject and imaging clinician using rehearsal.

Imaging commenced about 10 seconds prior to infusion initiation, and due to the limit of the scanner storage two consecutive acquisitions (~2.5 minutes each) were made to capture the full infusion period of ~5 minutes. Care was taken to minimise image acquisition down-time between recording sessions. Steady-state destruction-reperfusion imaging was conducted approximately 4 minutes after the infusion started, as an existing validated quantification method for comparison. The cannula was flushed with saline and disconnected. Subjects were exercised on a treadmill (walking speed: 2mph, +2%/3-mins, 15-minutes total), and then the imaging studies were repeated. The interval between cessation of exercise was minimised as far as practically possible. Measurements were repeated for each volunteer on consecutive days. One subject was excluded in this study due to acquisition error.

The whole image sequence was divided into five equal image segments of 300 frames each. The last segment was excluded in the data analysis to avoid the end of perfusion. Five region-of-interests were computer generated for the purposes of analysis (dimensions and placement on screen kept constant for all scans; see Figure 7). The MTD for both pre-exercise and after-exercise images were calculated and compared. Repeatability of the proposed method against destruction-reperfusion was also evaluated.

4.2.5 Large blood vessels elimination

Large blood vessels carrying large numbers of microbubbles may distort the measurement of active microvascular density. Visual inspection of scans can identify arteries and veins, and these can be manually removed from the ROI. A comparison before and after manual removal was made.

4.2.6 Non-rigid motion compensation

The motion of lower limb was tracked and corrected before any further processing by an image registration software MIRT (20). The software employs a non-rigid motion compensation framework (21, 22). The MS similarity measure, assuming that Rayleigh speckle noise in consecutive images is correlated, was chosen to deal with noisy B-mode ultrasound images (23). Maximum likelihood approach was used to estimate the transformation between the images and hence maximise the conditional probability. The registration and correction were firstly conducted on the simultaneously acquired B-mode sequence and then transferred to the CEUS image sequence.

4.2.7 Destruction and Replenishment (DR) analysis

The *in vivo* flow quantification was calculated using destruction replenishment time-intensity data (2, 14). A frame obtained 0.08 second after destruction is used as the background and is subtracted from subsequent frames to eliminate signal from non-capillary vessels (24). The replenishment curve was fitted with a mono exponential function, $y = A(1 - e^{-\beta t})$, where y is video intensity, A is plateau intensity and β is the rate constant using a non-linear least squares fitting algorithm in MATLAB. The time sequence analysed was measured from destruction flash to the end of the following 500 frames. Peak intensity, blood flow ($A \times \beta$) and flow reserve (ratio of blood flow after exercise to resting blood flow) were calculated from this model, and compared with the results obtained by our microbubble detection algorithm.

4.2.8 Statistical analysis

The microbubble track density (MTD) measures were calculated and the difference before and after exercise tested using paired samples *t* tests. A two-tailed test was used, with alpha set at 0.05. Statistical analysis was performed using online GraphPad Prism 6 (GraphPad Software Inc., San Diego, California, USA). For reproducibility the intra-class correlation coefficients (ICC) of MTD and DR methods for the four subjects' two repeats on different days were calculated and compared.

4.3 Results

4.3.1 Phantom validation

By examining the HLFR histograms two distinct peaks were detected at HLFR = 0.2 (microbubbles) and HLFR = 0.75 (noise). The locations of both peaks were similar for different concentrations of microbubbles. The segmentation results of the phantom with five microbubble concentrations are shown in Figure 4-3. It can be seen that more microbubbles were detected at higher concentration.

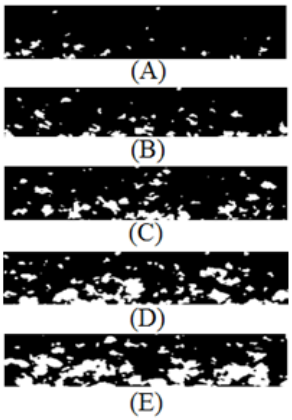

Figure 4-3: The segmentation results of the phantom with five microbubble concentrations (A) 0.05μL (B) 0.1μL (C) 0.15μL (D) 0.2μL (E) 0.25μL [The height of the ROI: 0.7cm]

The linear relationship between MTD and concentration is illustrated in Figure 4-4, with an R-square value of 0.89.

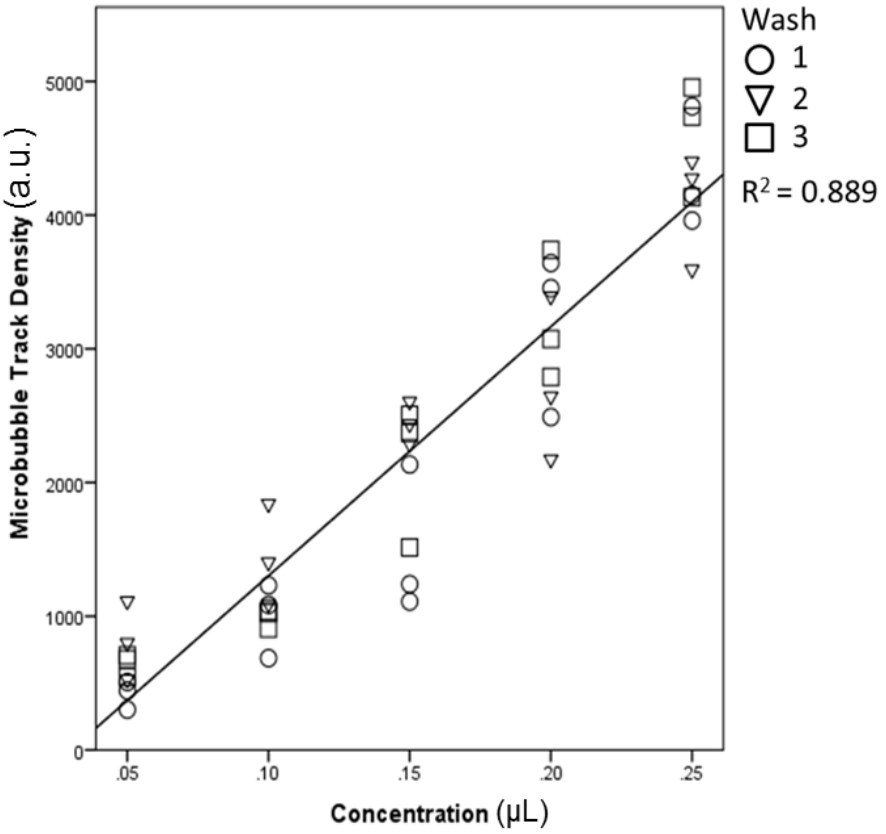

Figure 4-4: Microbubble track density measure versus microbubble concentration in the phantom. Three repeats of washing and re-injecting bubbles (Wash) and three repeats for each bubble injection were made

4.3.2 In vivo results

The plots of normalised HLFR of four subjects before and after exercise are displayed in Figure 4-5. Two distinct peaks are seen, the lower one corresponding to microbubbles and the higher peak for noise. The thresholds T_{HLFR} of the four subjects were automatically determined according to that described in section Microbubble detection algorithm to be 0.12 ($\hat{f}'$= 2.51, before exercise) and 0.167 ($\hat{f}'$= 2.51, after exercise) for subject 1, 0.093 ($\hat{f}'$= 1.88,

before exercise) and 0.14 ($\widehat{f}'$= 1.88, after exercise) for subject 2, 0.16 ($\widehat{f}'$= 2.51, before exercise) and 0.15 ($\widehat{f}'$= 1.88, after exercise) for subject 3, and 0.4 ($\widehat{f}'$= 1.26, before exercise) and 0.35 ($\widehat{f}'$= 0.94, after exercise) for subject 4.

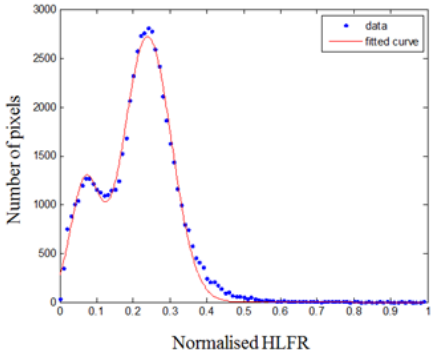

(A) before exercise

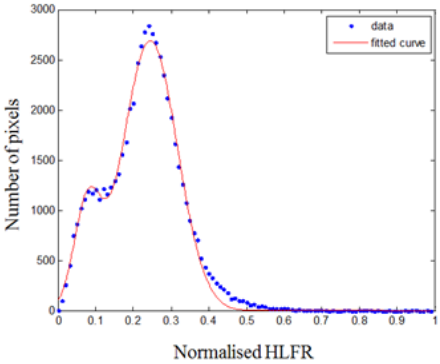

(B) after exercise

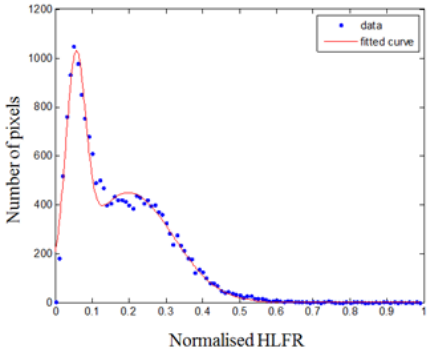

(C) before exercise

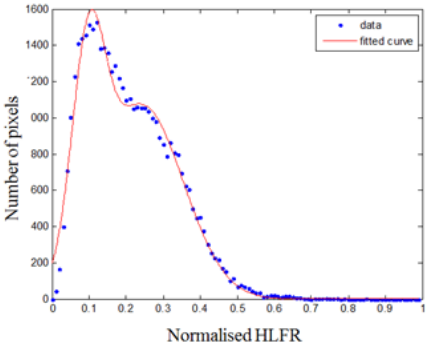

(D) after exercise

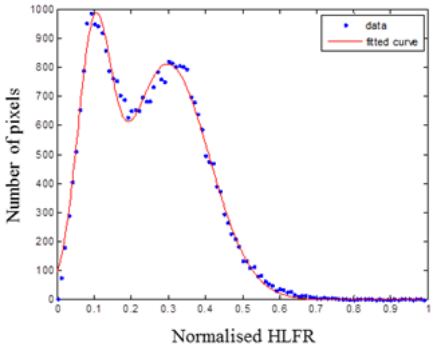

(E) before exercise

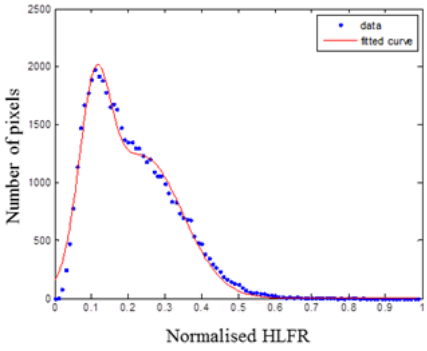

(F) after exercise

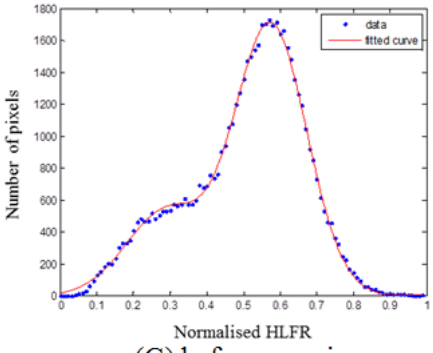

(G) before exercise

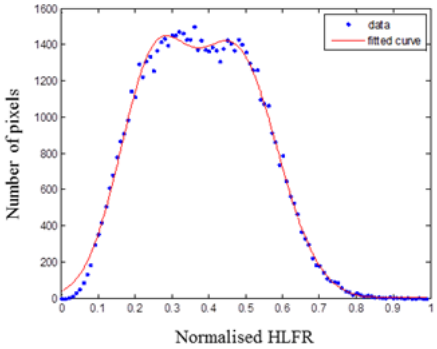

(H) after exercise

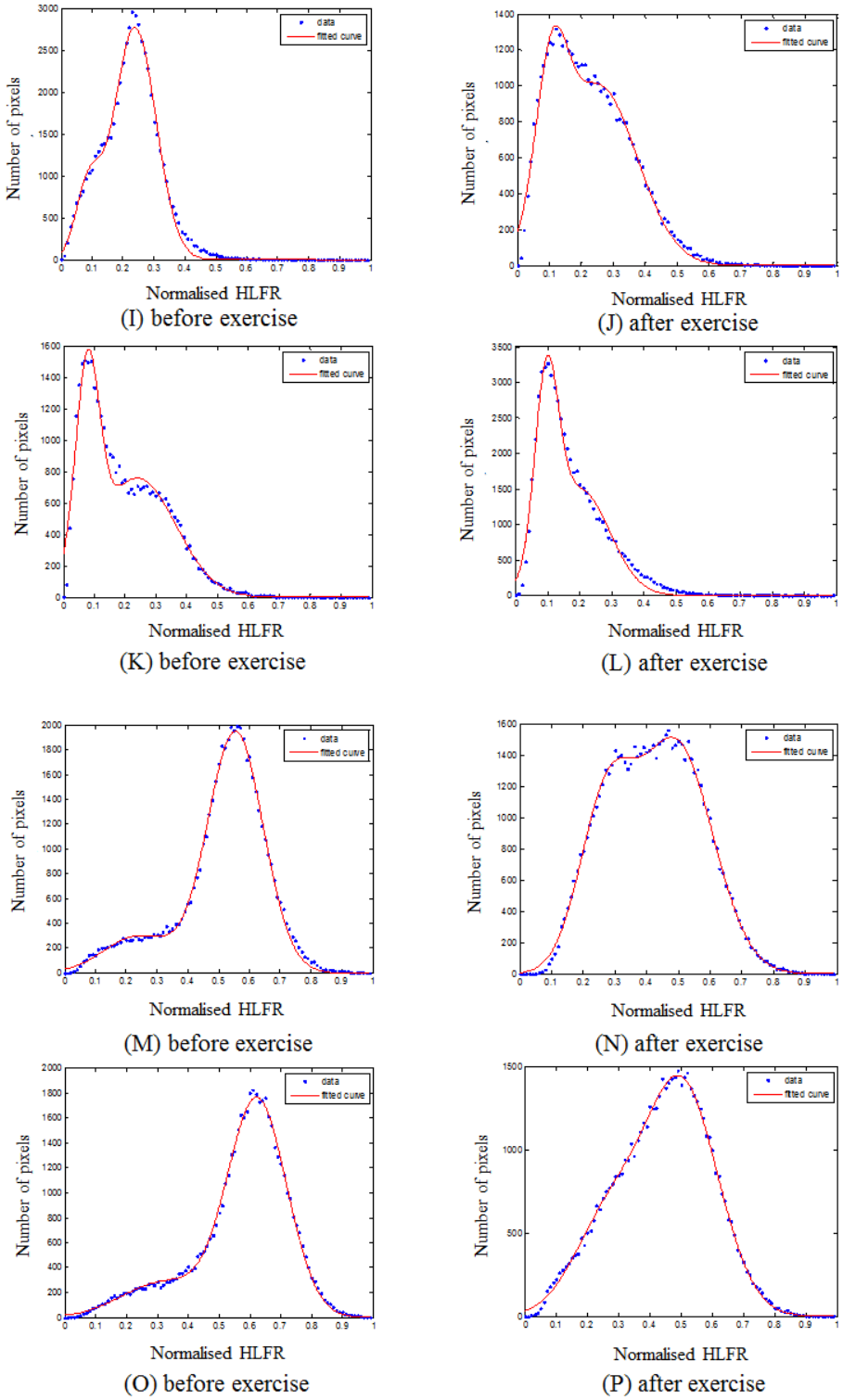

Figure 4-5: The normalised HLFR of (A, B) subject 1, (C, D) subject 2, (E, F) subject 3, (G, H) subject 4 before and after exercise of first day scan and the normalised HLFR of (I, J) subject 1, (K, L) subject 2, (M, N) subject 3, (O, P) subject 4 before and after exercise of second day scan

The segmentation results of four subjects before and after exercise are provided in Figure 4-6. It can be seen that the segmented microbubble areas increased after exercise.

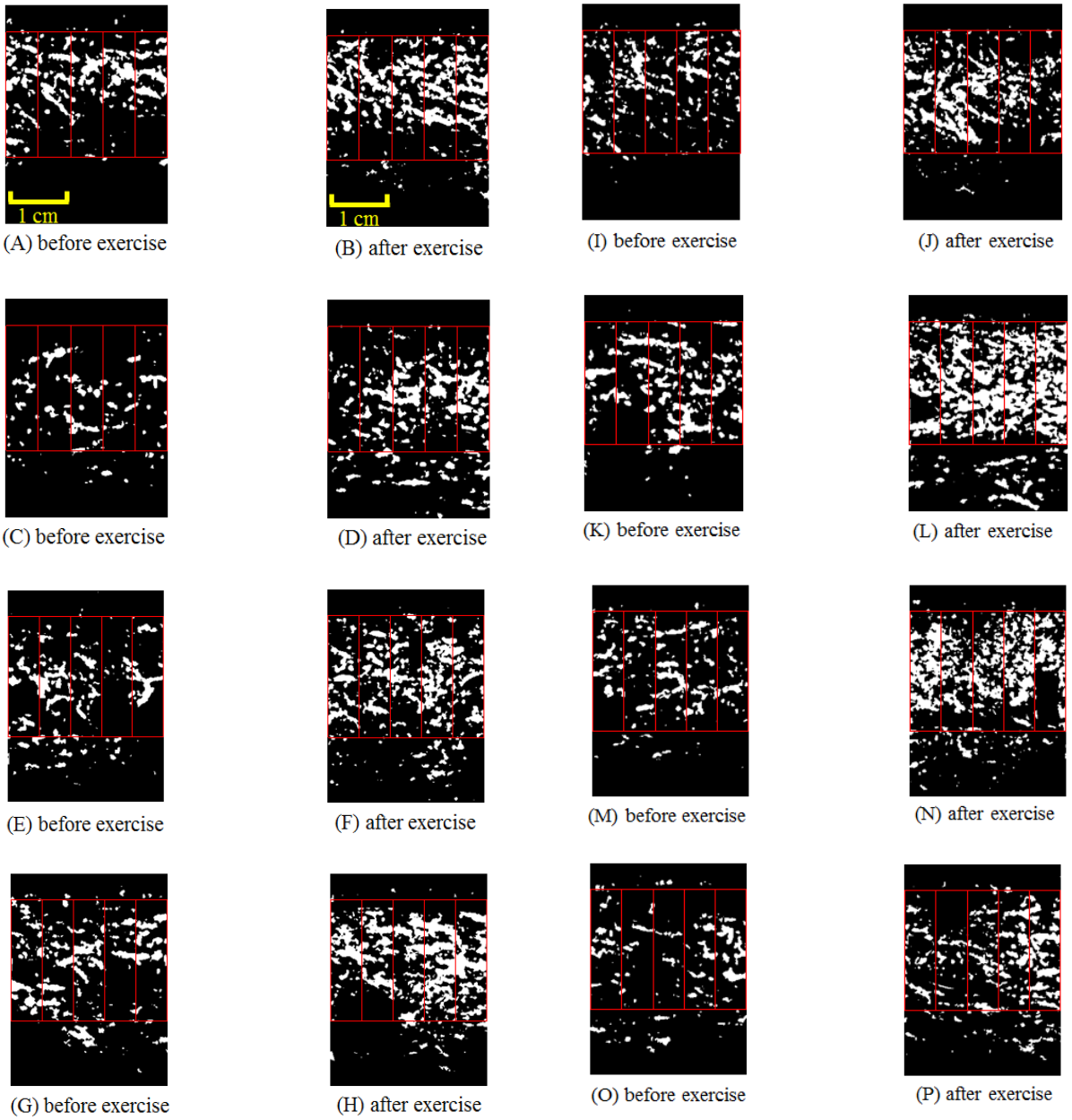

Figure 4-6: The CEUS segmentation results of subject 1 (A, B), subject 2 (C, D), subject 3 (E, F) and subject 4 (G, H), taken from gastrocnemius before and after exercise and after exercise of the first day and the CEUS segmentation results of subject 1 (I, J), subject 2 (K, L), subject 3 (M, N) and subject 4 (O, P), taken from gastrocnemius before and after exercise of the second day

4.3.3 Destruction and Replenishment analysis

The time intensity curves, fitted with the mono exponential function before and after exercise with a repeated scan are shown in Figure 4-7. The perfusion was increased after exercise.

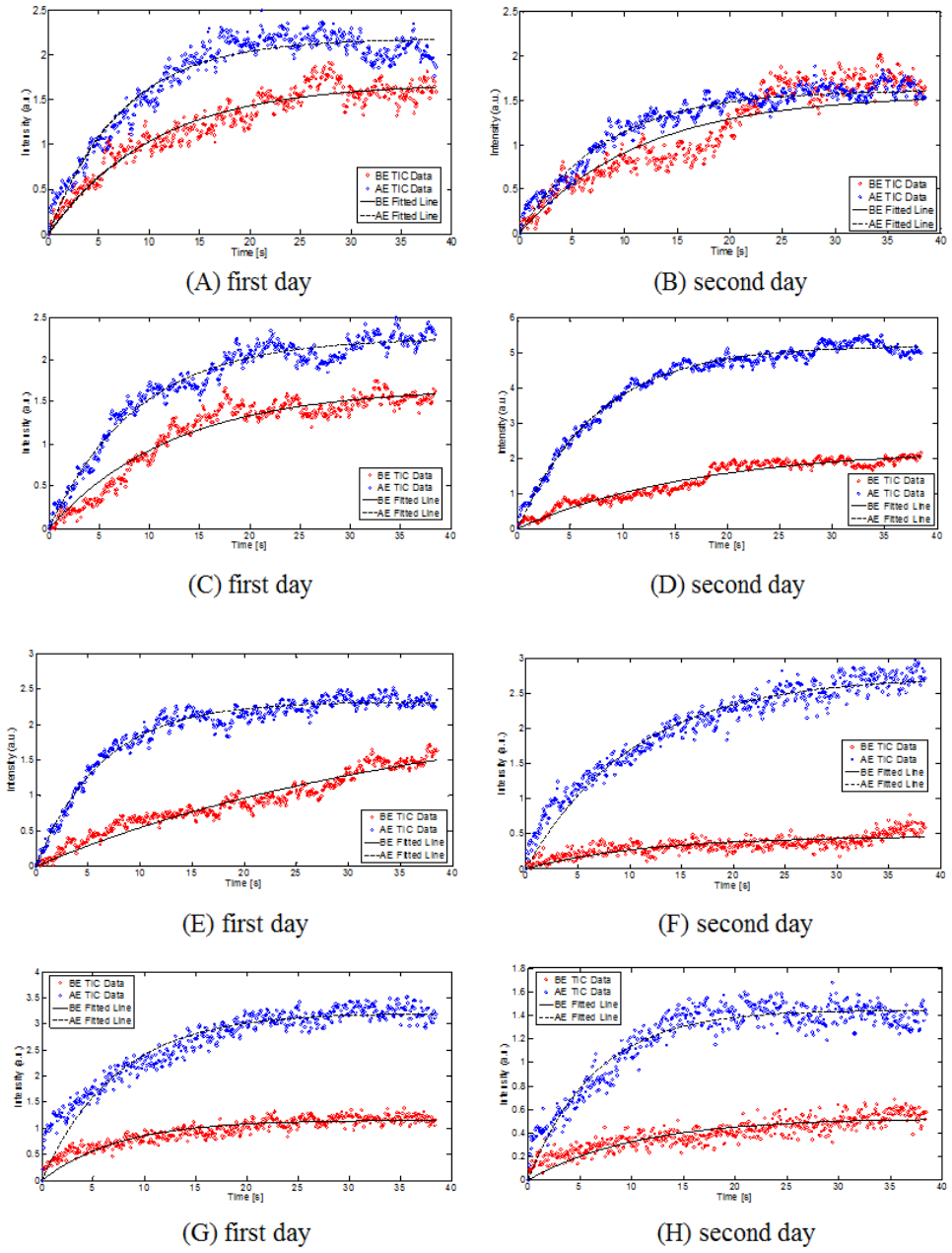

Figure 4-7: The disruption-replenishment time intensity curves with mono exponential of (A, B) subject 1, (C, D) subject 2, (E, F) subject 3, (G, H) subject 4 for the first and second day scans [BE - before exercise, AE - after exercise]

4.3.4 Reproducibility

The percentage change of microbubble track density after exercise for each scan is compared (Figure 4-8). The average percentage increase of microbubble track density (mean ± SD) was 138.2% ± 79.8 at the first day and 119.4% ± 62.7 at the second day, and the average percentage increase of MTD for two days was 128.8%. While for the existing DR method, the average percentage increase of peak intensity (mean ± SD) was 75.6% ± 71.6 at the first day and 234.7% ± 169.3 at the second day, and the average percentage increase of peak intensity for two days was 155.1%. For DR blood flow measurement, the average percentage increase (mean ± SD) was 213.8% ± 191.3 at the first day and 341.1% ± 215.4 at the second day for DR analysis, and the average percentage increase for two days was 277.4%. Furthermore, the DR average flow reserve (mean ± SD) was 3.1 ± 1.9 at the first day and 4.4 ± 2.2 at the second day for DR analysis, and the average flow reserve for two days was 3.7. Figure 4-9 also shows using a scatter plot how repeatable each method is. The proposed approach demonstrated excellent agreement on repeated measurements with the highest reproducibility (ICC = 0.96, p = 0.008), while the existing state-of-art DR analysis showed poor reproducibility of peak intensity (ICC = -0.39, p = 0.61), and better reproducibility of blood flow (ICC = 0.78, p = 0.09) and flow reserve (ICC = 0.78, p = 0.09).

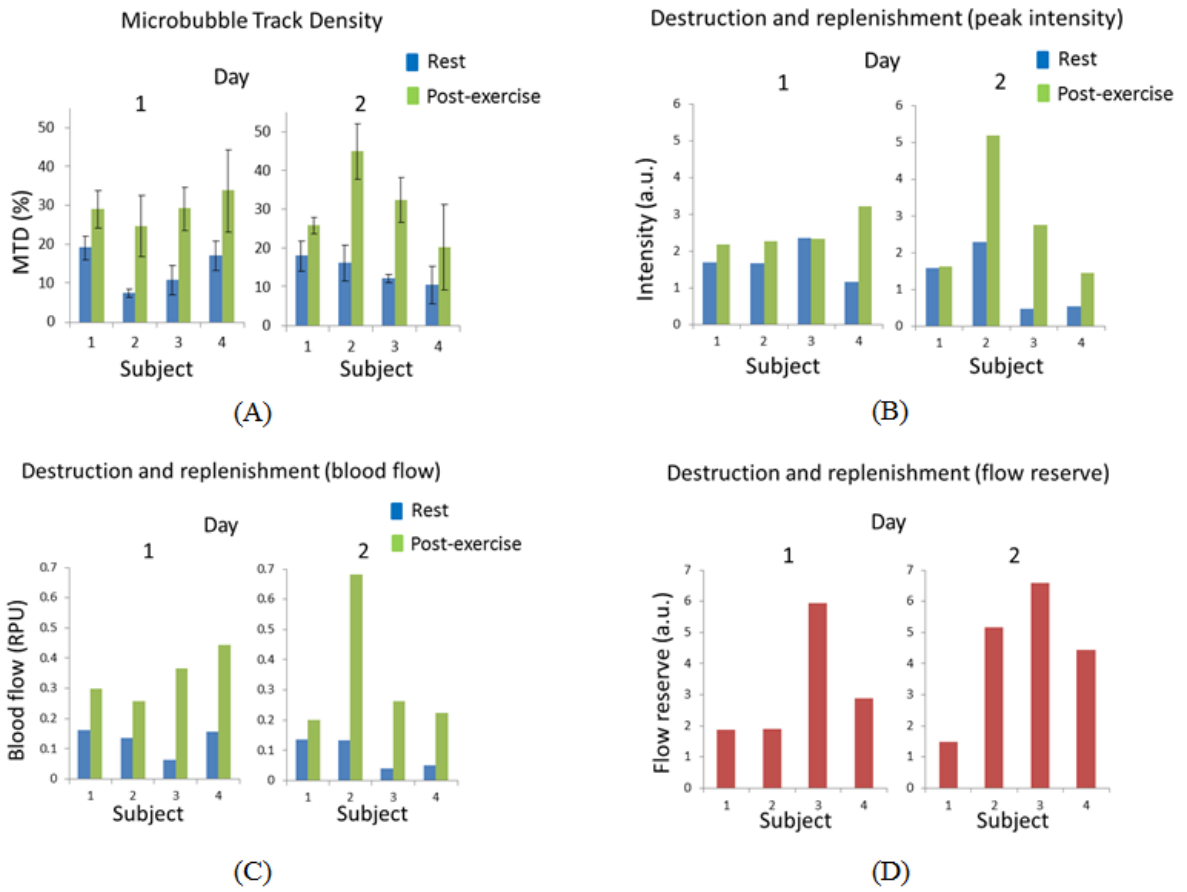

Figure 4-8: (A) Microbubble track density quantification by our microbubble detection algorithm per scan and (B) Peak intensity, (C) Blood flow, (D) Flow reserve by Destruction and Replenishment analysis before and after exercise

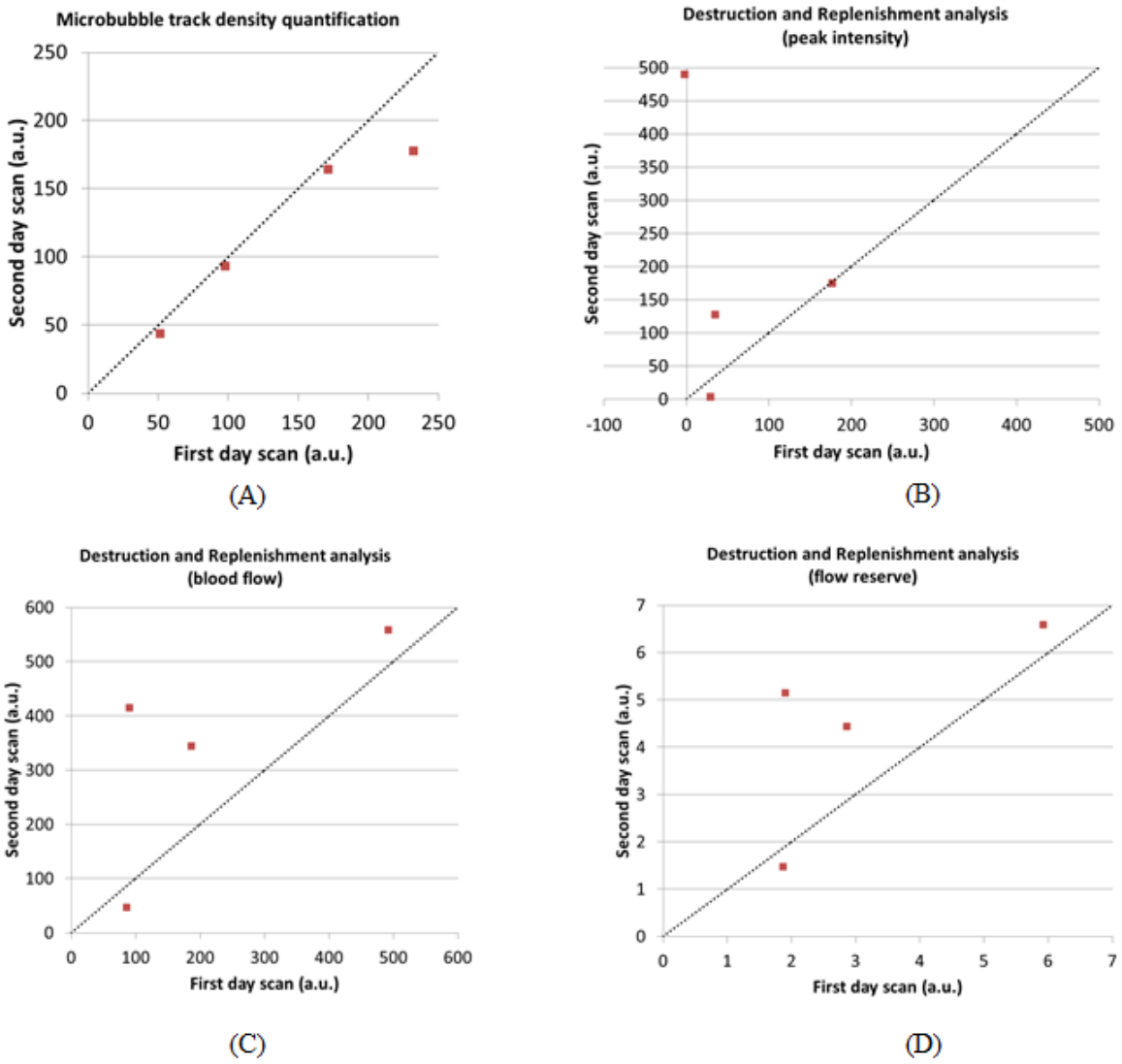

Figure 4-9: The plot of percentage change of first day scan vs second day scan by (A) Microbubble track density quantification and (B) Peak intensity, (C) Blood flow, (D) Flow reserve by destruction-replenishment analysis. (n=4)

4.3.5 Analysis with large blood vessels

The MTD using the proposed algorithm without removing large vessel signals was also calculated. The average percentage increase of microbubble track density (mean ± SD) was 130.2% ± 69.8 at the first day and 115.8% ± 63.3 at the second day. The average percentage increase of MTD was 123% for two days. Only a small change of ~6% in the averaged data

is found when comparing to the results with large vessels removed. The inclusion of large vessels does not change the repeatability of the results either (ICC = 0.97 vs. 0.96).

4.4 Discussion

A temporal and spatial image analysis method has been developed for detection and segmentation of microbubble signals to generate MTD, a quantitative surrogate measure for perfusion/tissue active capillary density. The method was validated in-vitro and then applied to healthy lower limb CEUS images to quantify active vascular density. The in-vitro results show an excellent linear relationship between the microbubble concentration and the MTD measure. The in vivo data on human lower limbs show a significant increase in MTD measure after exercise (129%) and the results are highly repeatable (ICC=0.96).

Quantification of active vascular density is valuable in a wide range of clinical applications. While CEUS imaging is increasingly used in clinical imaging and research, its repeatability and accuracy are still poor, largely due to the various factors that affect the image intensity-based quantification measures (15). The approach we proposed is the first study, as far as we are aware, to develop microbubble signal detection and segmentation technique by examining the relative frequency composition of the temporal signal, in order to classify pixels into either bubble pixels or noise pixels. Since the temporal signals of microbubbles and noise are very different, this approach allows effective separation of microbubbles from noise in the image. Since the relative frequency feature used in this method is image intensity independent and is more robust to the various confounding factors such as attenuation, the approach potentially offers more reliable and repeatable quantification results. This is likely the reason why this approach is shown to be much more repeatable than the accepted

disruption-replenishment analysis which is image intensity based (ICC of 0.96 vs 0.78). Moreover, our approach can deal with microbubbles travelling perpendicular to the 2D imaging plane, which existing spatial tracking approaches cannot do.

Besides reproducibility, this proposed method can also help address another key issue of the existing method for limb perfusion quantification; the low SNR associated with low basal blood flows in humans. As the proposed technique makes use of temporal information accumulated over a couple of minutes, it is more robust to noise. The in vivo data of this study demonstrated detection of a significant amount of bubble signal corresponding to basal blood flow.

The proposed method is based on temporal analysis of individual pixels so it is sensitive to the motion effect. As the motion of lower limb can be non-rigid (muscle movement may result in the images changing shape, and these shape changes cannot be corrected by a rigid body transformation), we employed a non-rigid motion correction (23) to reduce motion artefacts. While this correction technique seems to be effective in correcting motion and allows the generation of repeatable quantification results, any remaining motion that is uncorrected for could potentially introduce a bias in the quantification by magnifying vessel footprints.

For some applications the primary target of interest is small capillary vessels, and hence the existence of large vessels, e.g. in the lower limb images in this study, is less desirable and may affect the quantification result. In this study we have identified the apparent large vessels

in the data by visual inspections and manually removed them. We then compared the quantification results with or without the large vessels. In this case the results with and without large are very similar. The average percentage increase of MTD with large vessels is slightly smaller (123%) than the one without large vessels (129%) and the difference of average percentage increase is not statistically significant. This indicates that the result is not significantly affected by large vessels. As our approach counts the areas that any microbubble covers in CEUS images, even a single bubble slowly flowing through a small vessel would cover a significant area due to the point spread function of imaging system being much larger than the size of a microbubble/capillary. Therefore our approach seems to favour small vessels than larger ones which might explain why the existence of large vessels did not have a significant effect.

Our destruction reperfusion analysis is concordant with that reported in existing literature (14). The peak intensity and blood flow measurements increased after exercise. However, the reproducibility is not reported in that study. When our DR method is compared with MTD, the reproducibility characteristics of MTD are much more favourable.

The delay between the exercise and the imaging (~2 minutes) could reduce the flow reserve measurements. Another factor is that the physical exercise in this study is not very stressful so only a minor vasodilatation is expected. Both factors contributed to the low flow reserve comparing to that in (14).

It should be noted that our approach is different to the maximum intensity projection (MIP) (29, 30), which display the maximum image intensity during the whole acquisition period at each pixel. While MIP is a good tool to visualise vascular morphology, it is still image intensity based and has similar issues as other existing techniques when used for perfusion quantification.

The proposed method can be affected by the concentration of bubbles. Using too high a concentration of bubbles may cause saturation in the bubble detection results. Such saturation can be dealt with by either taking shorter video sequences, or by applying a statistical formula (31). Furthermore, it should be noted that the number of subjects is limited (n=4) in this study and further work on more subjects would be useful to confirm the robustness of our method.

The present study does not measure kinetics and hence perfusion. However, the frequency features of the image sequence data have information that allows not only an effective separation of bubbles from noise, but also potentially the velocity information of the blood flow. A pixel within a vessel with faster flow will generate higher temporal frequencies due to the more frequent appearance of microbubbles in the pixel temporal signal. These frequencies will also be dependent on microbubble concentration and further studies should be conducted to explore this extra information in the CEUS temporal signals.

This technique has great potential for clinical translation. Practically, it would be feasible to use tens of seconds of standard clinical CEUS scan data during plateau phase, and the quantification process can be fully automated with high repeatability. It has great potential in

the real-time assessment of limb perfusion/active capillary density in patients with peripheral perfusion deficits. The need for cardiovascular ionotropic support can have negative effects on peripheral perfusion, and CEUS may be able to guide intravascular filling needs and ionotropic support. CEUS could be used to accurately quantify capillary perfusion in post-operative surgical flap monitoring, guiding patient management and decision making. Our automated CEUS method could be used in an outpatient setting, provide a potentially valuable biomarker for clinically significant peripheral arterial disease, or attribute information to the management of the patient with a diabetic foot (prognosis, surgical planning, treatment monitoring). It also has the potential to be extended to other clinical applications, e.g. quantification of carotid/aortic plaque neovascularisation, breast screening or cancer monitoring.

4.5 Conclusions

The proposed microbubble detection method demonstrated excellent accuracy and repeatability in quantifying active vascular density and has great potential for clinical translation in the assessment of lower limb perfusion and beyond.

References

1. Claudon M, Dietrich CF, Choi BI, et al. Guidelines and good clinical practice recommendations for Contrast Enhanced Ultrasound (CEUS) in the liver - update 2012: A WFUMB-EFSUMB initiative in cooperation with representatives of AFSUMB, AIUM, ASUM, FLAUS and ICUS. Ultrasound Med Biol. 2013;39(2):187-210.

2. Wei K, Jayaweera AR, Firoozan S, et al. Quantification of myocardial blood flow with ultrasound-induced destruction of microbubbles administered as a constant venous infusion. Circulation. 1998;97(5):473-83.

3. Senior R, Moreo A, Gaibazzi N, et al. Comparison of sulfur hexafluoride microbubble (SonoVue)-enhanced myocardial contrast echocardiography with gated single-photon emission computed tomography for detection of significant coronary artery disease: a large European multicenter study. J Am Coll Cardiol. 2013;62(15):1353-61.

4. Huang PT, Huang FG, Zou CP, et al. Contrast-enhanced sonographic characteristics of neovascularization in carotid atherosclerotic plaques. J Clin Ultrasound. 2008;36(6):346-51.

5. Xiong L, Deng YB, Zhu Y, et al. Correlation of Carotid Plaque Neovascularization Detected by Using Contrast-enhanced US with Clinical Symptoms. Radiology. 2009;251(2):583-9.

6. Hellings WE, Peeters W, Moll FL, et al. Composition of Carotid Atherosclerotic Plaque Is Associated With Cardiovascular Outcome A Prognostic Study. Circulation. 2010;121(17):1941-U111.

7. Duerschmied D, Zhou Q, Rink E, et al. Simplified contrast ultrasound accurately reveals muscle perfusion deficits and reflects collateralization in PAD. Atherosclerosis. 2009;202(2):505-12.

8. Krix M, Krakowski-Roosen H, Kauczor HU, et al. Real-time contrast-enhanced ultrasound for the assessment of perfusion dynamics in skeletal muscle. Ultrasound Med Biol. 2009;35(10):1587-95.

9. Krix M, Krakowski-Roosen H, Amarteifio E, et al. Comparison of transient arterial occlusion and muscle exercise provocation for assessment of perfusion reserve in

skeletal muscle with real-time contrast-enhanced ultrasound. Eur J Radiol. 2011;78(3):419-24.

10. Amarteifio E, Krix M, Wormsbecher S, et al. Dynamic contrast-enhanced ultrasound for assessment of therapy effects on skeletal muscle microcirculation in peripheral arterial disease: pilot study. Eur J Radiol. 2013;82(4):640-6.
11. Amarteifio E, Weber MA, Wormsbecher S, et al. Dynamic contrast-enhanced ultrasound for assessment of skeletal muscle microcirculation in peripheral arterial disease. Invest Radiol. 2011;46(8):504-8.
12. Mitchell WK, Phillips BE, Williams JP, et al. Development of a new Sonovue contrast-enhanced ultrasound approach reveals temporal and age-related features of muscle microvascular responses to feeding. Physiol Rep. 2013;1(5):e00119.
13. Song Y, Li Y, Wang PJ, Gao Y**.** Contrast-enhanced ultrasonography of skeletal muscles for type 2 diabetes mellitus patients with microvascular complications. Int J Clin Exp Med. 2014;7(3):573-9.
14. Lindner JR, Womack L, Barrett EJ, et al. Limb stress-rest perfusion imaging with contrast ultrasound for the assessment of peripheral arterial disease severity. JACC Cardiovasc Imaging. 2008;1(3):343-50.
15. Tang MX, Mulvana H, Gauthier T, et al. Quantitative contrast-enhanced ultrasound imaging: a review of sources of variability. Interface Focus. 2011;1(4):520-39.
16. Cheung WK, Gujral DM, Shah BN, et al. Attenuation Correction and Normalisation for Quantification of Contrast Enhancement in Ultrasound Images of Carotid Arteries. Ultrasound in Medicine and Biology. 2015;41(7):1876-83.
17. Yildiz YO, Eckersley RJ, Senior R, et al. Correction of Non-Linear Propagation Artifact in Contrast-Enhanced Ultrasound Imaging of Carotid Arteries: Methods and in Vitro Evaluation. Ultrasound Med Biol. 2015;41(7):1938-47.

18. Tang MX, Eckersley RJ**.** Frequency and pressure dependent attenuation and scattering by microbubbles. Ultrasound Med Biol. 2007;33(1):164-8.

19. Hoogi A, Akkus Z, van den Oord SC, et al. Quantitative analysis of ultrasound contrast flow behavior in carotid plaque neovasculature. Ultrasound Med Biol. 2012;38(12):2072-83.

20. Myronenko A**.** Medical Image Registration Toolbox (MIRT) for Matlab (version 1.0) (https://sites.google.com/site/myronenko/research/mirt). 2006.

21. Lee S, Wolberg G, Shin SY**.** Scattered data interpolation with multilevel B-splines. Ieee Transactions on Visualization and Computer Graphics. 1997;3(3):228-44.

22. Rueckert D, Sonoda LI, Hayes C, et al. Nonrigid registration using free-form deformations: Application to breast MR images. Ieee Transactions on Medical Imaging. 1999;18(8):712-21.

23. Myronenko A, Song X, Sahn DJ**.** Maximum Likelihood Motion Estimation in 3D Echocardiography through Non-rigid Registration in Spherical Coordinates. Functional Imaging and Modeling of the Heart, Lecture Notes in Computer Science. 2009;5528(2009):427-36.

24. Belcik JT, Davidson BP, Foster T, et al. Contrast-enhanced ultrasound assessment of impaired adipose tissue and muscle perfusion in insulin-resistant mice. Circ Cardiovasc Imaging. 2015;8(4).

25. Christensen-Jeffries K, Browning RJ, Tang MX, et al. In Vivo Acoustic Super-Resolution and Super-Resolved Velocity Mapping Using Microbubbles. Ieee Transactions on Medical Imaging. 2015;34(2):433-40.

26. Viessmann OM, Eckersley RJ, Christensen-Jeffries K, et al. Acoustic super-resolution with ultrasound and microbubbles. Physics in Medicine and Biology. 2013;58(18):6447-58.

27. Ackermann D, Schmitz G**.** Detection and Tracking of Multiple Microbubbles in Ultrasound B-Mode Images. IEEE Trans Ultrason Ferroelectr Freq Control. 2016;63(1):72-82.

28. Rrico CE, Pierre J, Pezet S, et al. Ultrafast ultrasound localization microscopy for deep super-resolution vascular imaging. Nature. 2015;527(7579):499-+.

29. Parker DL, Wu J, van Bree RE**.** Three-dimensional vascular reconstruction from projections: a theoretical review. Engineering in Medicine and Biology Society, 1988. Proceedings of the Annual International Conference of the IEEE, 4-7 Nov. 1988 1988. 399-400 vol.1.

30. Anderson CM, Saloner D, Tsuruda JS, et al. Artifacts in maximum-intensity-projection display of MR angiograms. AJR Am J Roentgenol. 1990;154(3):623-9.

31. Siepmann M, Reinhardt M, Schmitz G**.** A statistical model for the quantification of microbubbles in destructive imaging. Invest Radiol. 2010;45(10):592-9.

Chapter 5

Differential intensity projection (DIP) for visualisation and quantification of plaque neovascularisation in CEUS images of carotid arteries

Intra-plaque neovascularisation (IPN) has been shown to be closely correlated with the plaque vulnerability. In this study a new image processing approach, differential intensity projection (DIP), was developed to visualise and quantify IPN in contrast enhanced ultrasound (CEUS) image sequences of carotid arteries. DIP used the difference between the local temporal maximum and the local temporal average signals to identify bubbles against tissue background and noise. The total absolute and relative areas occupied by bubbles within each plaque were calculated to quantify IPN. 24 CEUS image sequences of carotid arteries from head and neck cancer patients after radiotherapy were acquired. The results using DIP were compared with those obtained by maximum intensity projection (MIP) and visual assessment. The results show that DIP can significantly reduce nonlinear propagation tissue artefacts and is much more specific in detecting bubble signals than MIP, being able to reveal IPN signals which are buried in tissue artefacts in the corresponding MIP image. A good correlation is found between MVA (r = 0.83, p < 0.001) / MVD (r = 0.77, p < 0.001) obtained using DIP and the corresponding expert visual grades. In conclusion, the proposed method show great potential in quantification of IPN in contrast enhanced ultrasound of

carotid arteries. This work was done in collaboration with Dr Benoy Shah from Department of Echocardiography, Royal Brompton Hospital, where he focused on evaluation of intra-plaque neovascularisation using CEUS.

5.1 Introduction

Cardiovascular disease such as stroke is one leading cause of death in the world (1). The formation of atherosclerotic vulnerable plaque in the carotid artery could increase the risk of stroke (2, 3). Several studies have reported that intraplaque neovascularisation (IPN) is a precursor of intraplaque haemorrhage (IPH) and IPN could be a surrogate biomarker of unstable plaque (4-6). Therefore, quantification of IPN can be used for the early detection and clinical management of unstable atherosclerotic plaques and hence minimises the risk of stroke.

Recently, contrast-enhanced ultrasound (CEUS) imaging with microbubble contrast agents has provided a unique tool of visualizing and quantifying IPN. It has shown promise for imaging plaque vasculature. Several groups (7-9) have established correlations between CEUS imaging results and histological plaque neovascularisation and the risk of plaque rupture. However, in these studies, only subjective visual assessment was made to quantify the findings. Furthermore, although several computer algorithms (10, 11) are available to assist in the quantitative analysis of the images, they have some limitations. Hoogi et al. proposed a method for segmenting the contrast spots within atherosclerotic plaques in individual images by tracking individual microbubbles. The main advantage of this approach is that the temporal behaviour of bubble flow can be demonstrated. This makes it robust to noise and allows differentiation between blood vessels and artefacts. However, several

parameters of the algorithm were determined empirically from a few sequences, which may be a variable to quantitative results. Akkus et al. developed a statistical segmentation of carotid plaque neovascularisation. An iterative expectation-maximisation algorithm was employed to solve a mixture estimation problem and classify the pixel as either background, blooming of contrast, contrast spots or artefact. But, this technique has difficulties quantifying the IPN reliably for the plaque located on the far wall of the carotid artery due to nonlinear propagation artefacts (also called pseudo-enhancement artefact) (12, 13). Non-linear propagation of ultrasound creates artefacts in CEUS images that could significantly affect both qualitative and quantitative assessments of IPN (14). Although there is a correction method (15) to remove non-linear artefact, it requires additional post-processing which is not available on current commercial scanners.

Moreover, maximum intensity projection (MIP) is a common intensity-based bubble imaging method. It can visualise bubble paths (i.e. vessel trajectories) by displaying the maximum intensity over time for each pixel in CEUS images (16-18). While this approach is sensitive, simple and fast, the disadvantage is that this method has low specificity to bubbles. In particular, it is difficult to distinguish between tissue artefact due to nonlinear propagation and blood vessels, and therefore it could generate over-estimated vessel paths and affect quantification results.

The objective of this study was to develop and evaluate a sensitive, specific, simple and fast microbubble detection technique for CEUS carotid artery imaging by using differential intensity projection (DIP). This technique will be demonstrated in-vivo, and applied to the quantification of intraplaque neovascularisation in vivo.

5.2 Methods

5.2.1 Differential intensity projection

The proposed algorithm worked at a pixel level to detect microbubble signals. The CEUS images contained primarily three components: tissue artefact, noise, and microbubble signals. The differential intensity projection (DIP) was defined as below to capture the microbubble signals.

$$DIP(x_i, y_i) = \text{maximun}(I(x_i, y_i)) - \langle I(x_i, y_i) \rangle \quad (5\text{-}1)$$

where $DIP(x_i, y_i)$ is the differential image intensity at the *ith* pixel between the temporal peak signal $I(x_i, y_i)$ and the temporal average intensity $\langle I(x_i, y_i) \rangle$. For a given bubble occasionally passing an otherwise dark image pixel, the peak intensity was expected to be much higher than the average intensity. On the other hand, the peak intensity and the average intensity were expected to be similar for tissue signal. For noise both the peak and average intensity are expected to be relatively low. As a result, the differential intensity of pixels containing microbubble signals is expected to be higher than that of tissue or noise.

5.2.2 Threshold selection

A threshold in differential intensity was required to separate microbubble signal from tissue and noise. It was estimated from the histogram of differential intensity projection, an example of which is shown in Figure 5-1.

5.2.3 Microvascular area and density

The ROI in the plaque was selected manually. The number of pixels identified as containing bubble signal was defined as the microvascular area (MVA) measure, which can then be normalized by the total number of pixels within the plaque ROI to obtain the microvascular density (MVD) measure for the ROI.

$$MVD = \frac{\text{MVA}}{area\ of\ ROI} \tag{5-2}$$

5.2.4 Clinical application (plaque)

48 patients previously treated for head and neck cancer (HNC) with at least one risk factor for atherosclerosis were recruited from a cancer centre. 24 videos with carotid plaque were selected for this study. The study was approved by the institutional research and ethics committee and each patient provided informed consent. CEUS image sequences were acquired on both sides of the neck with a clinical scanner (GE Vivid7 with a 9 MHz broadband linear array transducer). A GE scanner was used to scan the subject with the following settings: MI = 0.21, Gain = 0, Dynamic Range = 54, TGC = manually adjusted, Frequency = 3.2/6.4 MHz. Contrast-enhanced ultrasound video loops were taken using a commercially available ultrasound contrast agent, SonoVue^{TM} (Bracco, Milan) given as an intravenous infusion via a peripheral vein at a rate of 1.2 mL/min. The infusion was delivered over a total of 5-7 minutes. Imaging was performed in real-time prior to the arrival of and following the saturation of the carotid artery with SonoVue.

5.2.5 Visual assessment

IPN was graded semi-quantitatively as absent (Grade 0), limited to the adventitia/plaque base (Grade 1) or extensive and/or extending into the plaque body (Grade 2) by a doctor blinded to the laterality of radiotherapy.

5.2.6 Motion compensation and DIP

The motion of the carotid artery was tracked and corrected by a dedicated motion correction algorithm (19). The algorithm consisted of three steps: (A) Pre-processing, (B) Lumen segmentation and (C) Registration. In the first step, the large rigid motions were removed by a rigid registration. Then, the algorithm used the information of the cardiac cycle and the Gabor filter responses of the corresponding frames to obtain a mixture of frames where the fragmentation of the lumen signal was largely removed. In the second step, the lumen was segmented by using thresholding and level set methods. A binary mask of the lumen region was obtained for each frame. Finally, a non-rigid registration was performed to correct the motion effect on each frame. It was based on minimising the energy functional of the non-lumen region of two consecutive images and the energy functional of the segmented lumen region of two consecutive binary masks.

Then DIP images were calculated for each CEUS image sequence using Eqn (5-1). Maximum Intensity Projection (MIP) is also obtained for comparison purpose.

5.2.7 Regions of interest (ROI) analysis

Analysis of CEUS video sequences was performed off-line using software developed in-house using MATLAB (The MathWorks, Natick, MA, USA). The carotid plaques were segmented manually as the regions of interest (ROIs) by a clinical expert using both CEUS sequence and maximum intensity projection (MIP) (Figure 5-2, first and second columns). Both MVA and MVD were calculated for each plaque, and results compared with visual grading.

5.2.8 Statistical analysis

The sample size is small and the sample is not normally distributed. Therefore, non-parametric statistical analyses are used in this study. The correlation between the visual grade and the MVA/MVD derived from our method was tested by Spearman rank correlation. The differences between the mean rank of MVA/MVD and in the visual grade groups were tested by Kruskall-Wallis test with alpha set at 0.05. Statistical analyses were performed using SPSS (IBM Corp. Released 2013. IBM SPSS Statistics for Windows, Version 22.0. Armonk, NY: IBM Corp.).

5.3 Results

5.3.1 Differential Intensity Histogram and Threshold selection

By examining the histogram of differential intensity projection (0.25) (Figure 5-1, dotted line), it can be seen that there are peaks in the histogram corresponding to microbubble, tissue and noise.

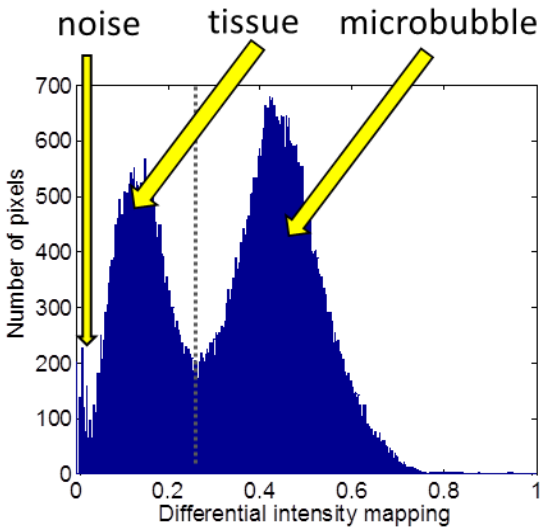

Figure 5-1: Histogram of differential intensity projection

5.3.2 Visual Assessment and Differential intensity projection

Among the 24 video sequences, Grade 0 IPN was seen in 12/24 videos, while Grade 1 IPN was seen in 8/24 videos and Grade 2 IPN was seen in 4/24 videos. Examples of CEUS images and the MIP images with each visual grade are shown in Figure 5-2. The corresponding DIP images are shown in Figure 5-2 (third column).

By examining MIP and DIP images of the same dataset against visually confirmed bubble signal by clinician experts (solid arrows in the images), DIP shows not only much less nonlinear tissue artefact and better image contrast, but also clearly reveals IPN signals which are buried by tissue artefacts in the correspond MIP image (Figure 5-2B)

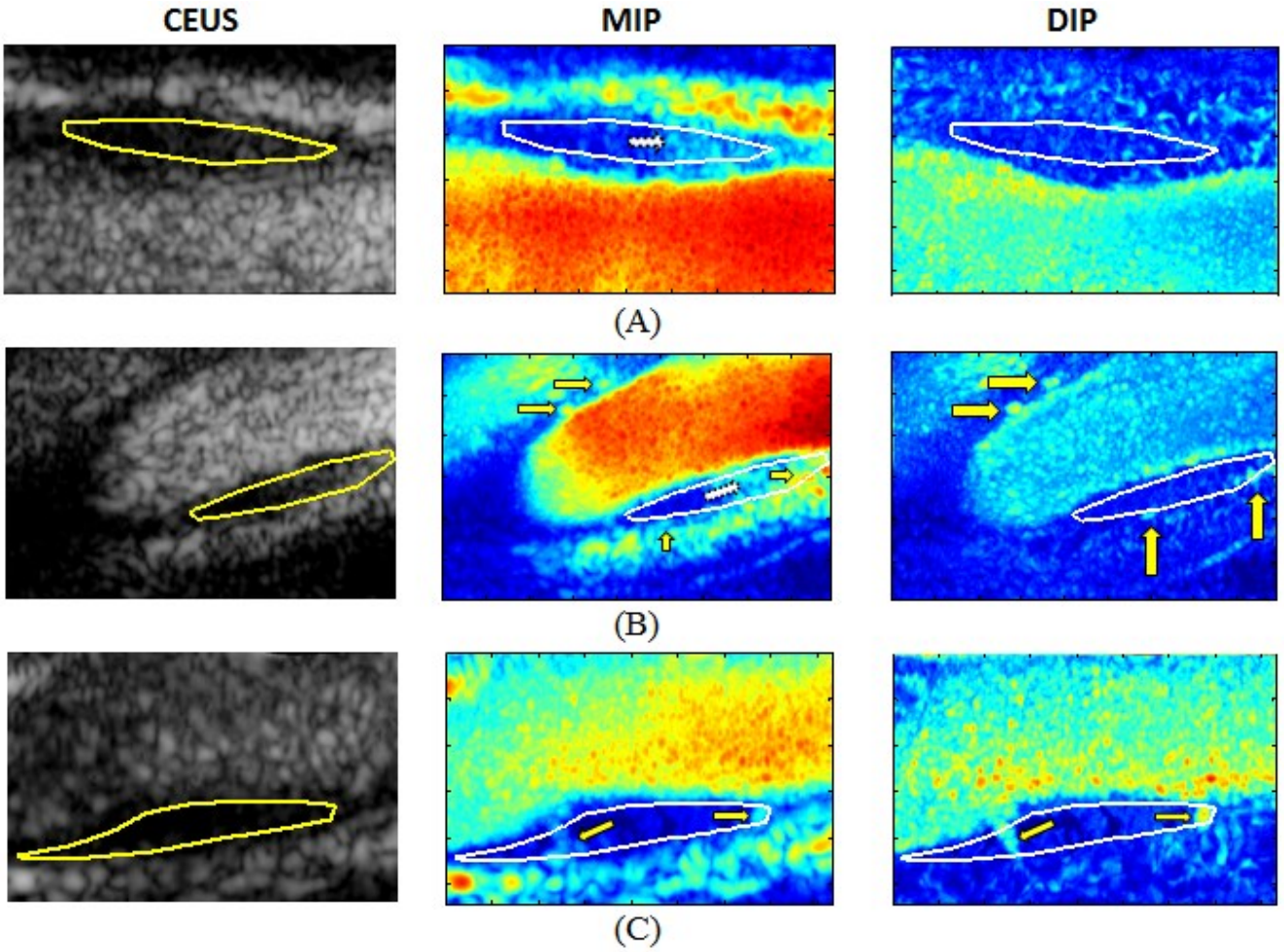

Figure 5-2: First column: CEUS image with ROI. Second column: Maximum intensity projection. Third column: Differential intensity projection. Row (A) plaque with grade 0 Row (B) plaque with grade 1 Row (C) plaque with grade 2, tissue artefact is indicated by an dashed arrow and bubble activity is indicated by an arrow.

5.3.3 Clinical evaluation (MVA and MVD)

The average and the median of log(MVA) for each visual grade were shown in Table 1. It can be observed that both mean and median of log(MVA) increased with the visual grade. Furthermore, Table 2 shows the average and the median of log(MVD) for each visual grade. It can be seen that mean of log(MVD) increased with the visual grade.

Table 5-1: The average and median of log(MVA) for each visual grade

Visual Grade	*Mean ± SD*	*Median*
Grade 1	1.78 ± 0.56	1.79
Grade 2	2.49 ± 0.50	2.36

Table 5-2: The average and median of log(MVD) for each visual grade

Visual Grade	*Mean ± SD*	*Median*
Grade 1	-1.70 ± 0.25 (%)	-1.70%
Grade 2	-1.49 ± 0.64 (%)	-1.70%

The box plots of visual grade vs MVA or MVD were displayed in Figure 5-3.

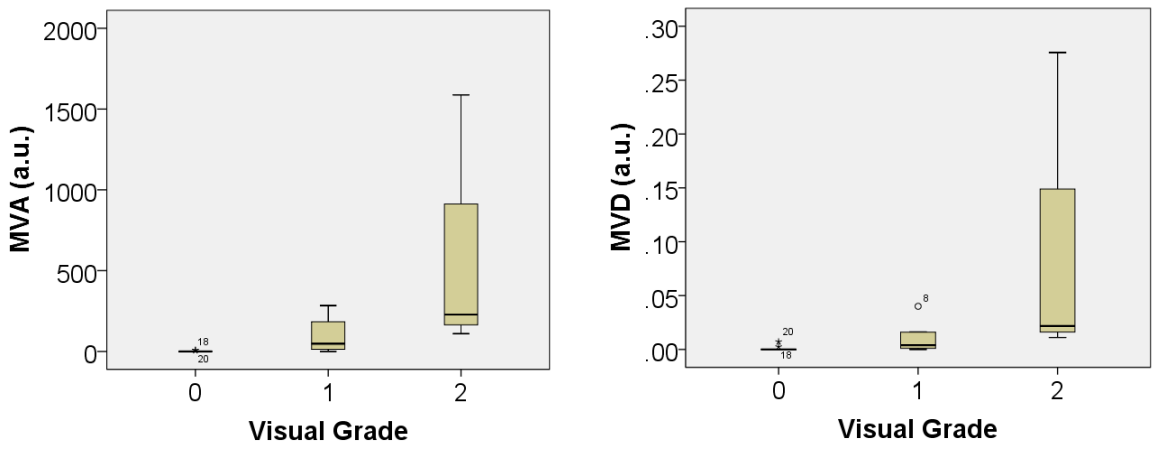

(A) (B)

Figure 5-3: The box plot of visual grade versus (A) MVA (B) MVD, outlier is indicated by a circle with number.

5.3.4 Spearman's rank correlation coefficient

Both MVA and MVD are significantly correlated with the visual grade (R= 0.83 and 0.77 respectively, with both, $p < 0.001$).

5.3.5 Kruskal-Wallis Test

Table 5-3: Visual grade groups comparison by Kruskal-Wallis test

Visual Grade Groups Comparison	*MVA*	*MVD*
Grade 0 vs Grade 1	$p = 0.001^{*}$	$p = 0.006^{*}$
Grade 1 vs Grade 2	$p = 0.126$	$p = 0.062$
Grade 0 vs Grade 2	$p = 0.001^{*}$	$p = 0.001^{*}$
* significant at $\alpha = 0.05$		

Table 5-3 shows the visual grade groups comparison. For the group grade 0 vs grade 1, there is a significant difference in MVA or MVD at $\alpha = 0.05$. Similarly, there is a significant difference in MVA or MVD at $\alpha = 0.05$ for the group grade 0 vs grade 2. However, for the group grade 1 vs grade 2, the difference in MVA or MVD is not significant at $\alpha = 0.05$, while the difference in MVD is significant at $\alpha = 0.1$.

5.4 Discussion

In this study a new image processing approach, differential intensity projection (DIP), was developed to visualise and quantify plaque IPN in contrast enhanced ultrasound (CEUS) image sequences of carotid arteries in vivo. The proposed DIP can significantly reduce nonlinear propagation tissue artefacts and improve imaging specificity. Two quantitative

measures, MVA which is related to the total vascular areas occupied by IPN in the plaque, and MVD which is a vascular density measure, were generated based on each DIP image. The in vivo data on human carotid artery shows a strong correlation between MVA/MVD and visual IPN grade and there is a significant difference in the MVA/MVD for the groups' comparison (i.e. grade 0 vs grade 1 or grade 0 vs grade 2). Comparing with MIP, our method can detect microbubble signal missed by MIP, and hence provides a more reliable way to visualise and quantify microbubble signals.

Quantification of IPN is valuable in clinical diagnosis. It is a novel surrogate marker of the risk of stroke. Recently several groups have developed various methods for IPN quantification. Huang et al. (20) proposed a dynamic evaluation of the plaque enhancement. The enhancement was analysed by a time intensity analysis (TIC). TIC is commonly used in analysing large and well perfused organs, for example, liver, prostate and heart. However, plaques in carotid artery are often small and weakly perfused, therefore, TIC analysis may not be appropriate to quantify microvessels in plaques. Hoogi et al. (10) adopted ECG grating to limit the motion and only one CEUS image per cardiac cycle was used. Hence, the connection of microvessel paths after time integration may be lost. More importantly, these algorithms can be significantly affected by nonlinear propagation tissue artefact. The DIP we proposed has a unique advantage of being able to efficiently reducing such tissue artefact.

One challenge of quantifying neovascularisation in plaque is the motion effect. It is due to the expansion and contraction of blood vessels, breathing and swallowing. Our dedicated motion compensation algorithm (19) was applied to improve the quantification of IPN. The software performs better than the current available softwares. It should be note that even though

motion compensation is applied, some out-of-plane motions could still affect the quantification. Any non-corrected motion will potentially introduce artefacts into the DIP images. Future study can take into account of out-of-plane motion, which could further improve quantification results.

Besides nonlinear propagation tissue artefact and motion compensation, attenuation is also an important issue which may affect the quantification. While it seems in this study the quantification is not significantly affected by attenuation, it may not always be the case. Recently, Cheung et al (21) have developed an automated attenuation correction and normalisation algorithm to improve the quantification of contrast enhancement in ultrasound images of carotid arteries. The algorithms firstly corrects attenuation artefact and normalises intensity within the contrast agent-filled lumen and then extends the correction and normalisation to regions beyond the lumen.

The proposed method can generate more specific visualisation of vessels and more reliable IPN quantification. It could have important implications for clinical screening, diagnosis and management of this important disease. Specifically such quantitative information on plaque vascularisation enables improved patient risk stratification and potentially improves drug treatment by acting as a tool for monitoring treatment.

The DIP is simple and computationally efficient and can be implemented in real time, as it only involves simple mathematical operations. The quantification process is semi-automated,

requiring manual input for segmenting the plaques. Fully automated segmentation is possible but requires further studies.

It should be noted that there is a small MVD overlapping of grade 1 and grade 2 plaques and their difference is not statistically significant. This is likely due to the small sample size of the analysis (n=4 for grade 2). More patient data in the future would help demonstrate any significance in quantification results between the two groups using our method.

In this study, our quantification technique in detecting IPN is demonstrated on the head and neck cancer patients who received radiotherapy treatment. It is known that HNC radiotherapy significantly increases the risk of plaque formation and risk of stroke (22). It should be noted that the technique presented is not limited to IPN quantification and has potential to be applied to other applications of microcirculation quantification.

5.5 Conclusions

DIP is demonstrated to be a specific, simple and fast technique for visualisation and quantification of small vessels in CEUS images and has great potential for clinical assessment of intraplaque neovascularisation.

References

1. Fuster V, Voûte J**.** MDGs: chronic diseases are not on the agenda. The Lancet. 2005;366(9496):1512-4.

2. Mughal MM, Khan MK, DeMarco JK, et al. Symptomatic and asymptomatic carotid artery plaque. Expert Rev Cardiovasc Ther. 2011;9(10):1315-30.

3. U-King-Im JM, Young V, Gillard JH**.** Carotid-artery imaging in the diagnosis and management of patients at risk of stroke. Lancet Neurology. 2009;8(6):569-80.

4. Virmani R, Burke AP, Farb A, Kolodgie FD**.** Pathology of the vulnerable plaque. Journal of the American College of Cardiology. 2006;47(8):C13-C8.

5. Hellings WE, Peeters W, Moll FL, et al. Composition of Carotid Atherosclerotic Plaque Is Associated With Cardiovascular Outcome A Prognostic Study. Circulation. 2010;121(17):1941-U111.

6. Feinstein SB**.** Contrast ultrasound imaging of the carotid artery vasa vasorum and atherosclerotic plaque neovascularization. Journal of the American College of Cardiology. 2006;48(2):236-43.

7. Coli S, Magnoni M, Sangiorgi G, et al. Contrast-enhanced ultrasound imaging of intraplaque neovascularization in carotid arteries: correlation with histology and plaque echogenicity. J Am Coll Cardiol. 2008;52(3):223-30.

8. Feinstein SB**.** The powerful microbubble: from bench to bedside, from intravascular indicator to therapeutic delivery system, and beyond. Am J Physiol Heart Circ Physiol. 2004;287(2):H450-7.

9. Giannoni MF, Vicenzini E, Citone M, et al. Contrast carotid ultrasound for the detection of unstable plaques with neoangiogenesis: a pilot study. Eur J Vasc Endovasc Surg. 2009;37(6):722-7.

10. Hoogi A, Akkus Z, van den Oord SC, et al. Quantitative analysis of ultrasound contrast flow behavior in carotid plaque neovasculature. Ultrasound Med Biol. 2012;38(12):2072-83.

11. Akkus Z, Bosch JG, Sánchez-Ferrero GV, et al. Statistical segmentation of carotid plaque neovascularization. SPIE Medical Imaging, 2013. International Society for Optics and Photonics: 867506--12.

12. Tang MX, Eckersley RJ**.** Nonlinear propagation of ultrasound through microbubble contrast agents and implications for Imaging. Ieee Transactions on Ultrasonics Ferroelectrics and Frequency Control. 2006;53(12):2406-15.

13. Tang MX, Kamiyama N, Eckersley RJ**.** Effects of Nonlinear Propagation in Ultrasound Contrast Agent Imaging. Ultrasound in Medicine and Biology. 2010;36(3):459-66.

14. ten Kate GL, Renaud GGJ, Akkus Z, et al. Far-Wall Pseudoenhancement during Contrast-Enhanced Ultrasound of the Carotid Arteries: Clinical Description and in Vitro Reproduction. Ultrasound in Medicine and Biology. 2012;38(4):593-600.

15. Yildiz YO, Eckersley RJ, Senior R, et al. Correction of Non-Linear Propagation Artifact in Contrast-Enhanced Ultrasound Imaging of Carotid Arteries: Methods and in Vitro Evaluation. Ultrasound Med Biol. 2015;41(7):1938-47.

16. Hoogi A, Adam D, Hoffman A, et al. Carotid plaque vulnerability: quantification of neovascularization on contrast-enhanced ultrasound with histopathologic correlation. AJR Am J Roentgenol. 2011;196(2):431-6.

17. van Ooijen PM, Ho KY, Dorgelo J, Oudkerk M**.** Coronary artery imaging with multidetector CT: visualization issues. Radiographics. 2003;23(6):e16.

18. Suri JS, Liu K, Reden L, Laxminarayan S**.** A review on MR vascular image processing: skeleton versus nonskeleton approaches: part II. IEEE Trans Inf Technol Biomed. 2002;6(4):338-50.

19. Stanziola A, Cheung WK, Eckersley RJ, Tang M-X**.** Motion correction in contrast-enhanced ultrasound scans of carotid atherosclerotic plaques. Biomedical Imaging (ISBI), 2015 IEEE 12th International Symposium on. 2015:1093-6.

20. Huang PT, Huang FG, Zou CP, et al. Contrast-enhanced sonographic characteristics of neovascularization in carotid atherosclerotic plaques. J Clin Ultrasound. 2008;36(6):346-51.

21. Cheung WK, Gujral DM, Shah BN, et al. Attenuation Correction and Normalisation for Quantification of Contrast Enhancement in Ultrasound Images of Carotid Arteries. Ultrasound in Medicine and Biology. 2015;41(7):1876-83.

22. Plummer C, Henderson RD, O'Sullivan JD, Read SJ**.** Ischemic stroke and transient ischemic attack after head and neck radiotherapy: a review. Stroke. 2011;42(9):2410-8.

Chapter 6

Summary, discussion and future work

6.1 Summary

In this thesis, three new methods have been developed to contribute to the field of contrast enhanced ultrasound image analysis and quantification.

Firstly, a correction method was proposed to significantly reduce attenuation effect in CEUS images of carotid arteries, based on which quantification could be improved. It was under the assumption that the microbubble contrast agents are well mixed in the vessel lumen, and therefore the image intensity across the vessel lumen should be homogeneous. It was shown, in both in-vitro experiment and in-vivo study, that this method could reduce shadowing artefact and improve homogeneity within the carotid lumens after the correction. This technique was applied to study contrast enhancement of carotid adventitial vasa vasorum as a biomarker of radiation-induced atherosclerosis. The results showed a significant difference in contrast intensity between irradiated and unirradiated carotid arteries and suggested that there is more contrast uptake in the adventitial vasa vasorum of irratidated arteries.

Secondly, an automatic microbubble segmentation and quantification technique based on temporal and spatial features of CEUS data was introduced. It was hypothesised that in CEUS image sequences the temporal signal profile of each pixel, particularly its frequency features, could be used to detect microbubbles passing the pixel. The relative area of these

"bubble pixels" could provide an area-based perfusion measure that is more robust than existing image-intensity based approaches. This method was applied to the lower limb CEUS images from healthy human volunteers to quantify active vascular density before and after physical exercise. The results showed a significant increase in MTD measure after exercise (129%) and the results were highly repeatable (ICC=0.96). This technique can potentially be used in real-time to assess limb perfusion/active capillary density in patients with peripheral perfusion deficits.

Finally, a differential intensity projection approach was developed to detect and quantify plaque neovascularisation in CEUS images of carotid arteries. The algorithm used temporal information to identify bubble signals. Two parameters, microvascular area (MVA) and microvascular density (MVD), were used to quantify the bubble signals. The results were compared with maximum intensity projection (MIP) and visual assessment. Visually, our method performed better than MIP as it showed a better elimination of tissue artefacts. There was also a strong correlation between MVA ($r = 0.83$, $p < 0.001$) / MVD ($r = 0.77$, $p < 0.001$) and visual grade. In conclusion, the proposed method showed great potential in quantification of intraplque neovascularisation in contrast enhanced ultrasound of carotid arteries.

To conclude, these techniques improve quantification in CEUS and provide automatic and objective qualitative results, which is a key for clinical translation of CEUS imaging in vascular assessment.

6.2 Discussion and future work

Although the results presented here have demonstrated the usefulness and effectiveness of the proposed methods in CEUS, it could be further developed in a number of ways.

In the first study, the attenuation correction method requires manual segmentation of the lumen, which limits the technique for a fully automatic correction. One can further improve this issue by introducing an automatic segmentation of the lumen. Segmentation techniques such as deformable template models, active contour segmentation methods and level set methods can be employed to extract the lumen region in a CEUS image. Moreover, this correction technique can be extended to study the cross-sectional of the carotid artery, where the perfused lumen could be a biomarker to indicate the degree of carotid stenosis.

In the second study, an automated temporal and spatial analysis algorithm was used to study active vascular density in the lower limbs of healthy human subjects. This study can be extended to the patients who suffer from peripheral arterial disease or diabetes. Patients with PAD would have a reduced capillary response to exercise, while resting capillary perfusion in symptomatic diabetic patients is expected to be lower than in healthy subjects. The quantitative results obtained by the algorithm can be used to confirm these expectations and to act as a potential monitoring tool for therapeutics of these diseases. Another possible extension is to apply this method to study 3D CEUS images. Currently, the quantitative results are limited to 2D CEUS images, and there is no information available in the third dimension. If 3D CEUS images are available, a 3D vasculature image could potentially be produced through this technique and it could be useful for visualisation and diagnosis of diseases which affect regional blood flow and may be missed by a 2D approach.

In the last study, future work could be done on extending the DIP algorithm to incorporate frequency features of microbubble, tissue artefact and noise signal as studied in Chapter 4. The quantification results could be further improved by capturing weak microbubble signals and eliminating strong noise signals. Furthermore, it is possible to extend the application of the algorithm from 2D CEUS carotid imaging to 3D imaging. This would allow the reconstruction of a 3D vasculature image of the whole plaque and out-of-plane motion is no longer an issue. The proposed quantification technique could be readily extended to 3D processing and the availability of 3D imaging data could provide a better quantification of IPN.